

Universität Stuttgart



Liv Prönneke

**Fluorescent Materials for Silicon
Solar Cells**

Institut für Physikalische Elektronik

Prof. J. H. Werner

Pfaffenwaldring 47

D-70569 Stuttgart

Fluorescent Materials for Silicon Solar Cells

Von der Fakultät Informatik, Elektrotechnik und Informationstechnik der
Universität Stuttgart zur Erlangung der Würde eines Doktor-Ingenieurs (Dr.-Ing.)
genehmigte Abhandlung

Vorgelegt von

Liv Prönneke

geboren am 17.10.1981 in Engelskirchen

Hauptberichter: Prof. Dr. rer. nat. habil. Jürgen H. Werner

Mitberichter: Prof. Dr. rer. nat. habil. Uwe Rau

Tag der Einreichung: 6. Juli 2011

Tag der mündlichen Prüfung: 23. Februar 2012

Institut für Physikalische Elektronik der Universität Stuttgart

2012

...two roads diverged in a wood, and I -
I took the one less traveled by,
and that has made all the difference.

Robert Frost

Inhaltsverzeichnis

Zusammenfassung	1
Abstract	4
1 Introduction	6
1.1 Motivation	6
1.2 Objective	6
1.3 Outline	7
2 System components	10
2.1 Solar Cell	11
2.2 Fluorescent Collector	12
2.3 Photonic Band Stop Filter	14
2.4 Component Matching	16
3 Monte-Carlo ray-tracing simulation	18
3.1 Simulation method	18
3.2 Systems in their radiative limits	22
3.2.1 System geometries and idealized components	23
3.2.2 Classical set-up: side-mounted solar cells	27
3.2.3 Novel concept: bottom-mounted solar cells	28
3.3 Influence of loss mechanisms	33
3.4 Conclusion and Outlook	38
4 Experimental results	39
4.1 Measuring and modeling reabsorption	39
4.1.1 Measuring reabsorption in fluorescent collectors	40
4.1.2 Comparison to Monte-Carlo simulation	42

4.1.3	Analytical fit	44
4.1.4	Conclusion and Outlook	51
4.2	Current increase of a-Si cell under fluorescent collector	52
4.2.1	Measuring concentration in fluorescent collectors	52
4.2.2	Comparison to Monte-Carlo simulation	57
4.2.3	Link to Reabsorption	58
4.2.4	Conclusion and Outlook	62
4.3	Geometrical and dispersive concentration	64
4.3.1	Geometrically concentrating troughs under fluorescent collectors	64
4.3.2	Outdoor measurement results for July, 2010	70
4.3.3	Conclusion and Outlook	75
4.4	Output power increase of c-Si module under fluorescent collector . . .	79
4.4.1	50 % power increase due to fluorescent collector	79
4.4.2	Threshold area	84
4.4.3	Conclusion and Outlook	86
4.5	Efficiency increase in photovoltaic modules by colored cell connectors	88
4.5.1	Experimental set-up	89
4.5.2	Results for calculated efficiency	91
4.5.3	Conclusion and Outlook	95
A	Exemplary component matching	97
B	Evenly filled spherical surfaces	99
C	Solar Cell Parameter	100
	Nomenclature	102
	List of Tables	107
	List of Figures	108
	Bibliography	111
	Danksagung	116
	Erklaerung	118

Zusammenfassung

Photovoltaische Systeme mit Fluoreszenzkollektoren benutzen die Konversion und Konzentration solarer Photonen, um Solarzellenwirkungsgrade zu erhöhen. Fluoreszenzmoleküle in einer Acrylglasplatte absorbieren einfallende Strahlung und emittieren räumlich isotrop verteilte Photonen in einen niedrigeren Energiebereich. Die Acrylglasplatte totalreflektiert die gestreuten Photonen und leitet sie zu den Kollektorseitenflächen. Daher beschäftigt sich die Forschung üblicherweise mit Solarzellen, die an den Kollektorseitenflächen angebracht sind. Diese Arbeit analysiert Wirkungsgradsteigerungen in photovoltaischen Systemen mit Fluoreszenzkollektoren, die *oben auf* der Solarzelle liegen.

Der erste Teil dieser Arbeit nutzt eine Monte-Carlo Simulation, um Vergleiche zwischen Fluoreszenzkollektorsystemen mit seitlich angebrachten und mit darunter liegenden Solarzellen zu ziehen. Zusätzlich untersucht die Simulation den positiven Einfluss einer photonischen Struktur über dem Kollektor. Die Ergebnisse zeigen, dass die Sammelwahrscheinlichkeit für Photonen in beiden Systemen abhängig ist von der Skalierung der Zellflächen und Zellabstände. Systeme mit seitlich angebrachten Solarzellen liefern höhere Erträge bei größeren Skalierungen. Für kleine Skalierungen ist der Fluoreszenzkollektor mit darunter liegenden Solarzellen jedoch genauso gut. Die Berücksichtigung von nicht strahlenden Verlusten und die Verwendung einer photonischen Struktur zeigen ebenfalls, dass unten liegende Solarzellen genauso viele Photonen einsammeln wie seitlich angebrachte, jedoch empfindlicher in der Skalierung sind.

Der zweite Teil der Arbeit präsentiert fünf experimentelle Ergebnisse, die einerseits grundsätzliche Mechanismen in Fluoreszenzkollektoren analysieren. Andererseits zeigen sie, wie Fluoreszenzfarbstoffe gewinnbringend in photovoltaischen Solarmodulen eingesetzt werden können.

i) Zur Messung der Reabsorption fallen LED-Photonen der Wellenlänge $\lambda = 406$ nm auf die Kollektoroberfläche. Eine Kamera hinter dem Kollektor fotografiert

mindestens einmal reabsorbierte Photonen, die die Rückseite verlassen. Eine analytische Beschreibung der Absorption und Emission im Kollektor liefert aus den Kamerabildern den Reabsorptionskoeffizienten $\alpha_{\text{reabs}} = 0.021 \text{ mm}^{-1}$.

ii) Light beam induced current (LBIC-) Messungen an einer amorphen Silizium-solarzelle zeigen, dass ein aufliegender Fluoreszenzkollektor den gesammelten Strom um 7% erhöht. Eine zusätzliche photonische Struktur erhöht den Strom um 95%. Eine analytische Beschreibung für dieses Experiment sagt unter Verwendung des im ersten Experiment ermittelten Reabsorptionskoeffizienten den Verlauf der Intensität vorher. Damit ist die Messung des Reabsorptionskoeffizienten ausreichend, um die Photoneneinsammlung in photovoltaischen Systemen mit Fluoreszenzkollektoren zu beschreiben, ohne, dass langwierige LBIC-Messungen nötig sind.

iii) Feldexperimente unter realer Sonneneinstrahlung vergleichen Solarzellen aus monokristallinem Silizium (c-Si) in Acrylglaströgen mit und ohne aufliegenden Fluoreszenzkollektor. Ist der Fluoreszenzstoff auf die Trogapertur begrenzt, so verringert er den Stromertrag. Eine fünffach größere Kollektorfläche erhöht den Stromertrag um 50% im Vergleich zu der begrenzten Fläche. Dieses Ergebnis verdeutlicht den Vorteil von streuender Konzentration gegenüber geometrischer Konzentration. Um den Stromertrag mit geometrischer Konzentration zu erhöhen, müssen neue Konzentratorsysteme mit zusätzlicher Solarzellenfläche gebaut werden. Das Experiment zeigt noch einen anderen Vorteil auf: Da die Fluoreszenzplatten die Photonen unabhängig von ihrem Winkel einsammeln, ist ihr Ertrag in Systemen mit und ohne Nachführung gleich.

iv) Zwei parallel geschaltete $2 \times 2 \text{ cm}^2$ c-Si Solarzellen erreichen unter einem Fluoreszenzkollektor eine elektrische Leistung $P_{\text{el}} = 189 \text{ mW}$. Derselbe Aufbau mit einer undotierten Acrylglasplatte erreicht nur $P_{\text{el}} = 125 \text{ mW}$. Durch die Variation der Solarzellenabstände zeigt dieses Experiment außerdem, dass die Aktivierung der umliegenden photovoltaisch inaktiven Fläche unbedingt notwendig ist, um die Verluste durch Streuung direkt über der Solarzelle zu kompensieren.

v) Alle vorherigen Experimente zeigen, dass Fluoreszenzstoffe direkt auf Solarzellen in der Praxis immer zu Verlusten führt. Das letzte Experiment vermeidet diese unerwünschten Verluste, indem der Fluoreszenzstoff nur die optisch inaktiven Zellverbinder einer $15 \times 15 \text{ cm}^2$ großen industriellen c-Si Solarzelle bedeckt, die mit Glas verkapselt ist. Der Fluoreszenzstoff auf den geweißten Zellverbindern streut einfallende Photonen in alle Richtungen. Die Oberfläche des Glases zur Luft totalreflektiert gestreute Photonen und lenkt sie auf die Solarzelle. Der mithilfe von LBIC- und Quanteneffizienzmessungen errechnete Wirkungsgrad der Zelle steigt von

$\eta = 16.0\%$ auf $\eta = 16.2\%$.

Zusammenfassend findet diese Arbeit nicht nur eine neue Charakterisierungsmethode für Konzentration durch Fluoreszenz. Sie zeigt außerdem, dass bei einer sorgfältigen Skalierung die Anwendung von Fluoreszenzkollektoren auf photovoltaischen Solarmodulen höhere Wirkungsgrade liefert.

Abstract

Photovoltaic systems with fluorescent collectors use the conversion and concentration of solar photons to increase solar cell efficiencies. Fluorescent dye in a dielectric plate absorbs incoming rays and emits spatially randomized photons with a lower energy range. The acrylic plate then guides part of the emitted spectrum to the collector side surfaces due to total internal reflection. Conventional research therefore applies solar cells to the side surfaces. This work analyzes the efficiency enhancement due to fluorescent collectors *on top of* solar cells which promises an easier technological handling.

The first part of this work uses a Monte-Carlo simulation to model photovoltaic systems with fluorescent collectors and photonic structures. The results allow the comparison between side- and bottom-mounted solar cells. Examining the systems in the radiative limit achieves maximum theoretical limits. In each system, the photon collection probability depends strongly on the scaling of cell size and distance. The side-mounted solar cells performs better for larger scales, but for small scales bottom-mounted solar cells achieve equally high efficiencies. Consideration of non-radiative loss mechanisms and the application of a photonic structure also leads to the result that the application of solar cells to the collector back side needs careful scaling but performs as good as side-mounted solar cells.

The second part presents the results of five experiments which analyze basic mechanisms in the fluorescent collector. Additionally, the experiments explore the benefits of fluorescent material in photovoltaic modules.

i) The reabsorption experiment directs photons from an LED with wavelength $\lambda = 406$ nm onto the collector top surface. A camera under the collector photographs photons which leave the back side. These photons are reabsorbed at least once. An analytical description extracts the reabsorption coefficient $\alpha_{\text{reabs}} = 0.021 \text{ mm}^{-1}$ from the camera picture.

ii) Light beam induced current (LBIC) measurements on an amorphous silicon

solar cell show that a fluorescent collector on top increases the collected current by 7%. The additional application of a photonic structure enhances the current by 95%. An analytical description of the absorption and emission processes in the collector using the reabsorption coefficient determined in the first experiment predicts the line-scans gained in the LBIC measurements. Therefore, the reabsorption measurement is sufficient enough to predict the collection performance of photovoltaic systems with fluorescent collectors without performing long LBIC-measurements.

iii) Outdoor experiments compare mono crystalline silicon (c-Si) solar cells in acrylic troughs with and without fluorescent collectors on top. Fluorescent distribution added to the geometrical concentration decreases the current gain if limited to the trough aperture. A five times larger fluorescent collecting plate leads to a current gain enhancement by at least 50% compared to the limited aperture. This shows the advantage of fluorescent concentration. Achieving an increased current gain with geometrical concentration requires a new trough and more solar cell material. The experiments also show another advantage: Fluorescent collectors concentrate photons independent of their angle. Thus, photovoltaic systems using fluorescent concentration perform best even without tracking.

iv) Two parallel connected $2 \times 2 \text{ cm}^2$ c-Si solar cells under a fluorescent plate achieve an electrical output power $P_{\text{el}} = 189 \text{ mW}$. The same set-up with an undoped acrylic plate on top gains $P_{\text{el}} = 125 \text{ mW}$. By varying the cell distance this experiment additionally points out that the activation of surrounding photovoltaic inactive area is crucial to compensate losses directly above the solar cell.

v) The last experiment avoids unfavorable losses by applying fluorescent dye to only the optical inactive cell connectors of a $15 \times 15 \text{ cm}^2$ industrial c-Si solar cell encapsulated under glass. The fluorescent dye covering the white painted connector distributes incoming photons at all angles. The glass-air surface guides distributed photons onto the solar cell via total internal reflection. Derived with LBIC and Quantum Efficiency measurements, the efficiency of the solar cell increases from $\eta = 16.0\%$ to $\eta = 16.2\%$.

In conclusion, this work not only finds a new characterization method for the fluorescent concentration. Additionally, it presents that applying fluorescent dye on top of photovoltaic solar modules increase efficiencies under careful consideration of the scaling.

Chapter 1

Introduction

1.1 Motivation

Electricity generation with photovoltaic systems is a growing market everywhere in the world. Figure 1.1 presents the data for Germany over the last 20 years. The total consumption as well as the fraction of photovoltaic generated electricity increases. An enhanced production of solar modules decreases the costs and enables the consumer to install photovoltaic systems with low financial investment.

Not only in Germany with a well established electricity grid, photovoltaic modules gain interest but also in developing countries with dispersed population and often no electricity supply at all. Here, solar power generation shows its main advantages of local installation and easy scaling of power plant size. Research and development therefore reaches for lower costs via reducing solar cell material or enhancing the solar cell efficiency. Increasing the efficiency requires either better electrical or optically improved properties of the solar cell. Unfortunately, optical improvement of the solar cell top surface often vanishes in the module, because the module glass is the actual surface towards the sun. Furthermore, in a module, areas like cell inter-spaces [2] and cell connectors [3, 4] are photovoltaic inactive, because they reflect impinging photons. Therefore, special interest lies in improving optical properties of solar *modules* for lower costs and higher efficiencies.

1.2 Objective

Fluorescent collectors are acrylic plates containing fluorescent dye. The collector concentrates incoming photons since the dye emits absorbed photons spatially ran-

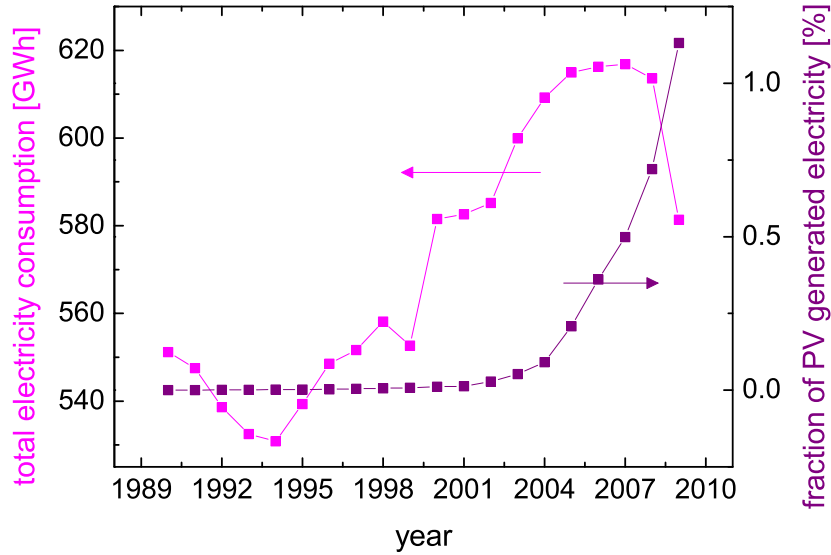


Fig. 1.1: Fraction of photovoltaic generated electricity on annual electricity consumption [1].

domized and the acrylic plate guides photons due to total internal reflection to the collector edges. Because of this side-guiding behavior, research follows mainly the objective to mount solar cells at the collector sides [5–7]. The main object of this work is the examination of solar cells *under* the fluorescent collector, a geometry which is easier to construct technologically. First, this work uses a Monte-Carlo simulation to model photovoltaic systems with fluorescent collector in the radiative limit. The results allow the comparison of the maximum efficiencies of side-mounted with bottom-mounted solar cells. Second, five experiments aim to understand and to use the beneficial concentration of fluorescent collectors for underlying solar cells.

1.3 Outline

Chapter 2 presents a short introduction to the examined system components solar cell, fluorescent collector and photonic structure.

Chapter 3 explains the Monte-Carlo simulation and presents the comparison between fluorescent collectors with side- and bottom-mounted solar cells and an optional photonic structure. The systems are in the radiative limit. The simulation

therefore provides maximum theoretical limits. The efficiency of the systems depends strongly on the scaling of the size and the distance of the solar cells. Side-mounted solar cells reach larger efficiencies for large scales. However, for small scales bottom-mounted solar cells achieve equally high efficiencies. Therefore, using solar cells under a fluorescent collector needs careful scaling but reaches efficiencies of the same value as side-mounted solar cells.

Chapter 4 presents five experiments sketched in Figs. 1.2a-e. The reabsorption measurement in Fig. 1.2a takes place by directing LED photons with the wavelength $\lambda = 406$ nm onto the collector surface. A black circle absorbs directly transmitted photons. A camera photographs the photons which are reabsorbed at least once and leave the back surface outside the circle. An analytical description extracts the reabsorption coefficient α_{reabs} from the camera picture. The light beam induced current (LBIC) measurement in Fig. 1.2b on an amorphous silicon (a-Si) solar cell under a fluorescent collector impressively shows the concentration effect. The application of a photonic structure increases the concentration even more. The reabsorption coefficient determined in the first experiment predicts the contribution of the formerly inactive area around the solar cell. The outdoor experiments in Fig. 1.2c explore the advantages of fluorescent concentration over geometrical concentration. In the experiment in Fig. 1.2d the fluorescent collector enhances the efficiency of a solar module with two parallel connected mono crystalline silicon (c-Si) solar cells. In the experiments in Figs. 1.2b-d, fluorescent collectors cover the whole solar cell area. Above the cell the distribution of photons is always of disadvantage. Figure 1.2e shows an experiment where the fluorescent concentration limited to the optical inactive cell connector area increases the efficiency by distributing photons, such as they are totally internal reflected at the module glass.

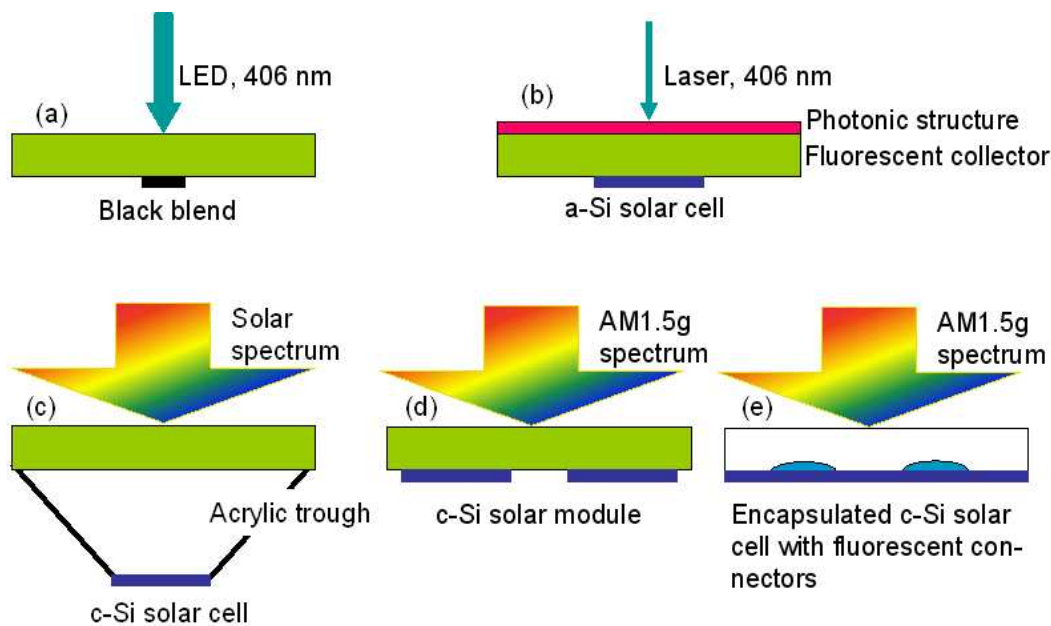


Fig. 1.2: a) Reabsorption measurement: Photons leaving the bottom surface of the collector outside the circle are reabsorbed once. An analytical fit determines the reabsorption coefficient. b) light beam induced current (LBIC) measurement of fluorescent collector with and without photonic structure on top above amorphous silicon (a-Si) solar cell. c) Geometrical concentrator with and without fluorescent collector on top of mono crystalline silicon (c-Si) solar cell measured outdoor. d) Efficiency measurement of two parallel connected c-Si solar cells. e) Quantum efficiency and LBIC measurements on encapsulated c-Si solar cell with fluorescent cell connectors.

Chapter 2

System components

This section describes in short the theoretical background for the components used in the analyzed photovoltaic systems: the solar cell, the fluorescent collector and the photonic band stop (PBS) filter.

A fluorescent collector -as understood in this thesis- is an acrylic glass plate doped with fluorescent dye molecules. Figures 2.1a-e sketch the functionality of a photovoltaic system with fluorescent collector, side-mounted solar cells and an optional PBS filter. Figure 2.1b indicates that the fluorescent dye absorbs incoming photons with energy range E_1 . Subsequently, the dye emits fluorescence photons which are shifted spectrally due to the Stokes shift ([8], p. 695f). The shift produces photons with a lower energy range E_2 which partly overlaps with the incident energy range E_1 ([9], p.38). Aside from being spectrally shifted, the emitted photons are distributed with spatially randomized spherical angles (θ, ϕ) defined in Fig. 2.1a.

Figure 2.1b also shows that the acrylic plate with refractive index $n_r^{\text{ag}} \approx 1.5$ ([10], p. 1156) guides emitted photons with angles θ larger than the angle of total internal reflection $\theta_c = 42.2^\circ$ ([8], p.487f). In contrast, photons with $\theta < \theta_c$ leave the collector as implied in Fig. 2.1c. Guided photons travel through the collector until they either are reabsorbed by the dye or reach an optically coupled solar cell. The reabsorption occurs for photons which are emitted into an energy range where the dye absorbs, because then the fluorescence spectrum overlaps with the absorption spectrum of the dye. If an emitted photon reaches a solar cell attached to the fluorescent collector (see Fig. 2.1b), the solar cell needs to be optically coupled to the collector. The optical coupling disables the total internal reflection. For the experiments in Sects. 4.2, 4.3, 4.4 and 4.5 I choose Glycerin, because its refractive index $n_r^{\text{oc}} \approx 1.5$ [11] lies between the refractive index of the acrylic glass n_r^{ag} and

the refractive index of the solar cell ($n_r^{c-Si} \approx 3.9$ for crystalline and $n_r^{a-Si} \approx 4.6$ for amorphous silicon [12]).

The application of a PBS filter avoids losing photons with angles $\theta < \theta_c$. Figure 2.1d shows the ideal PBS filter which is energy selective only ($\theta_{pbs} = \theta_c$). Figure 2.1e depicts that an angular selective PBS with $\theta_{pbs} < \theta_c$ guides photons $\theta < \theta_{pbs}$ to the sides. All other rays are subject to total internal reflection only. In the following sections I provide the basic mathematic descriptions needed to calculate the efficiency of photovoltaic systems with fluorescent collector and solar cells.

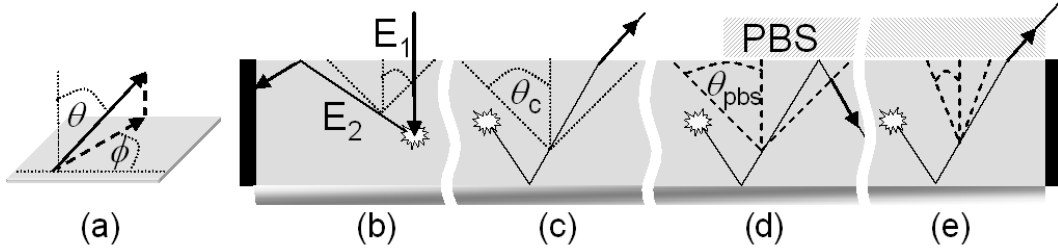


Fig. 2.1: Light guiding behavior of a fluorescent collector covered with solar cells at the sides and a mirror at its back side. a) Definition of photon ray spherical angles θ and ϕ . b) The dye absorbs photons with energy E_1 and emits them spatially randomized with energy E_2 . The system leads rays with $\theta > \theta_c$ to the collector edges. c) Rays with angle $\theta < \theta_c$ for total internal reflection leave the top surface. d) Applying a photonic band stop (PBS) filter keeps rays with $\theta < \theta_{pbs}$ in the system as well. This PBS is energy selective with $\theta_{pbs} = \theta_c$. Therefore, rays with energies $E = E_2$ are kept in the system. e) For an energy and angular selective PBS a reflection cone is assumed, such that -aside from the totally internally reflected photons- only rays with $E = E_2$ and $\theta < \theta_{pbs}$ are kept in the system.

2.1 Solar Cell

The photovoltaic efficiency

$$\eta = J_{SC}V_{OC}FF/P_{opt} \quad (2.1)$$

is the ratio between the maximum electrical power $P_{el} = J_{SC}V_{OC}FF$ and the impinging optical power $P_{opt} = 100 \text{ mW/cm}^2$. Here, FF is the fillfactor of the solar cell's current voltage characteristics. The open circuit voltage

$$V_{OC} = \frac{kT}{q} \ln(J_{SC}/J_0 + 1) \quad (2.2)$$

with Boltzmann constant k , elementary charge q and temperature T ($T = 300$ K throughout this work) depends on the ratio between short circuit current density J_{SC} and the saturation current density J_0 . Following the calculations in [13], the consideration of radiative losses only [14, 15] leads to

$$J_0 = \pi q \int_{E_{\min}}^{E_{\max}} QE(E)\Phi_{\text{em}}(E)dE \quad (2.3)$$

and the short circuit current density

$$J_{\text{SC}} = \pi q \int_{E_{\min}}^{E_{\max}} QE(E)\Phi_{\text{inc}}(E)dE. \quad (2.4)$$

Here, E_{\min} and E_{\max} denote the lower and upper energetic limit of the spectrum $\Phi_{\text{inc}}(E)$ incident onto the solar cell and of the spectrum $\Phi_{\text{em}}(E)$ emitted by the solar cell. The external quantum efficiency

$$QE(E) = \frac{N_{\text{coll}}(E)}{N_{\text{in}}(E)} \quad (2.5)$$

is the ratio between the number $N_{\text{coll}}(E)$ of collected electrons and the number $N_{\text{in}}(E)$ of incident photons [16].

2.2 Fluorescent Collector

Applying a fluorescent collector between the sun and a solar cell has spatial and spectral effects on the spectrum $\Phi_{\text{inc}}(E)$ incident on the solar cell. The spatial distribution of photons during the emission and the light guiding behavior of the acrylic plate leads photons onto the solar cell which have their incident point distant from the solar cell area. Thus, on the one hand, the fluorescent collector concentrates photons onto the cell. On the other hand, the spatial distribution is disadvantageous directly above a solar cell [17]. Here, photons usually reaching the solar cell are absorbed and due to the spatially randomized emission only partly directed towards the solar cell. Aside from changing the *spatial* distribution of solar photons reaching the solar cell, the fluorescent collector also causes a *spectral* change of the spectrum impinging onto the solar cell which therefore becomes

$$\Phi_{\text{inc}}^{\text{FC}}(E) = \Phi_{\text{inc}}(E)p_c^{\text{inc}}(E). \quad (2.6)$$

Here, $p_c^{\text{inc}}(E)$ is the ratio between photons reaching the solar cell area and photons incident on the fluorescent collector. Thus, the short circuit current density J_{SC}

of a solar cell attached to a fluorescent collector is different from the solar cell's J_{SC} (Eq. 2.4) alone. Fluorescent collectors also change J_0 by weighing the spectrum emitted by the solar cell as follows

$$\Phi_{\text{em}}^{\text{FC}}(E) = \Phi_{\text{em}}(E)p_{\text{c}}^{\text{em}}(E). \quad (2.7)$$

Here, $p_{\text{c}}^{\text{em}}(E)$ denotes the ratio between photons leaving the collector and photons emitted by the solar cell [13]. The collection probabilities $p_{\text{c}}^{\text{inc}}(E)$ and $p_{\text{c}}^{\text{em}}(E)$ depend on various system parameter like the absorption and emission in the fluorescent dye, the coverage fraction of the solar cells and the incident spectrum. The changed spectra $\Phi_{\text{inc}}^{\text{FC}}$ and $\Phi_{\text{em}}^{\text{FC}}$ (Eqs. 2.6 and 2.7) then replace Φ_{inc} and Φ_{em} in Eqs. 2.4 and 2.3, respectively. In order to identify the collection probabilities, I numerically analyze the system with statistical distributed photon energies as elaborately described in Sect. 3.1.

For the experiments in Sect. 4.5, I use ultra-violet (UV), red and yellow fluorescent paint with absorbance A and photoluminescent emission PL as seen in Figs. 2.2a, b and c respectively. [18–21]. In order to measure their properties, I apply them at the bottom of a glass plate. The experiments in Sects. 4.1, 4.2, 4.3 and 4.4 analyze a photovoltaic system with fluorescent collectors provided by PerspexTM (Acid Green, 6T66 [22]). The collectors consist of an acrylic plate doped with a green fluorescent dye with absorbance A and photoluminescence PL spectrum as in Fig. 2.2d. The absorbance of the fluorescent dyes used in these sections

$$A = 1 - T_{\text{D}} - R_{\text{AG}} \quad (2.8)$$

is derived by measuring the direct transmittance T_{D} of the fluorescent collector and the reflectance R_{AG} at the acrylic top surface [13]. The emission spectrum is detected by a photoluminescence measurement.

Absorbance A and photoluminescence PL always overlap for fluorescent dyes [23]. Photons emitted in the absorbance range of the dye have the chance to be reabsorbed. As indicated in Fig. 2.2b, the overlap is therefore called reabsorption range. The red fluorescent dye (Fig. 2.2b) has a narrow reabsorption range compared to the yellow fluorescent dye (Fig. 2.2c) which absorbs all emitted photons. In the yellow dye, emitted photons which are guided in a collector with yellow dye have a higher chance to be reabsorbed before they reach a solar cell than in red fluorescent dye. Thus, a narrower reabsorption range leads to a higher concentration of photons [24].

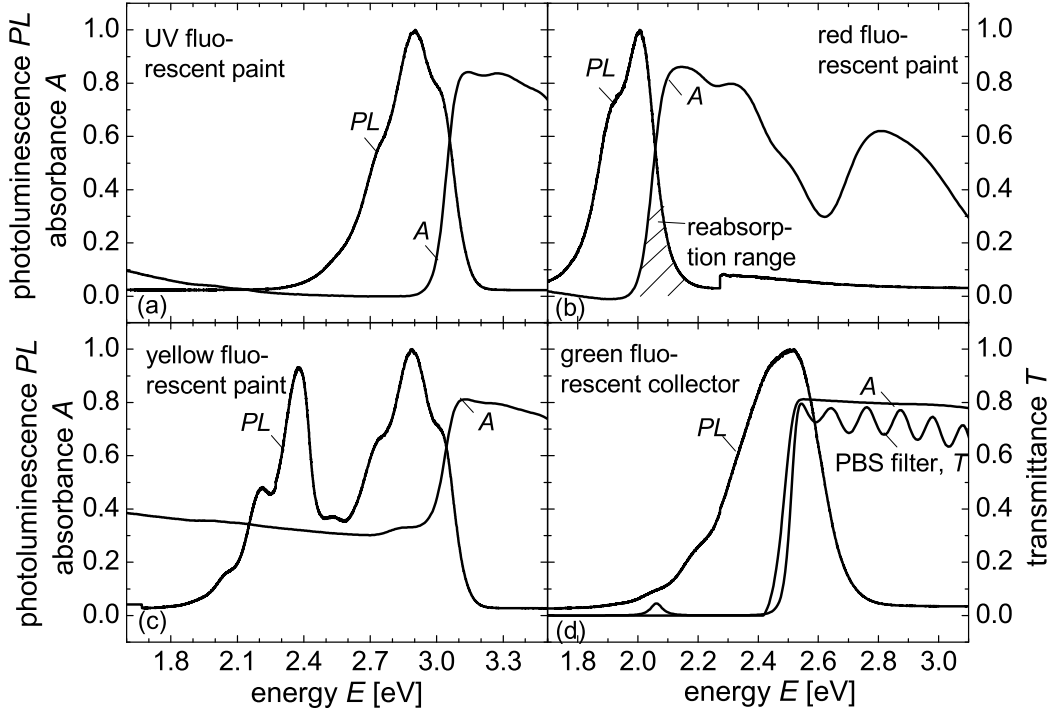


Fig. 2.2: Absorbance A and photoluminescence PL of the fluorescent materials used in Sect. 4.5. a) Ultra-violet (UV) fluorescent paint. b) Red fluorescent paint. c) Yellow fluorescent paint. d) Fluorescent collector used in Sects. 4.1, 4.2, 4.3 and 4.4. Also, the transmittance spectrum T_D of the photonic band stop (PBS) filter used in Sect. 4.2.

2.3 Photonic Band Stop Filter

A photonic band stop (PBS) filter selectively transmits incoming photons regarding their energy and incident angle. Thus, the presence of a reflecting photonic structure on a photovoltaic system with fluorescent collector changes the spectrum incident on the solar cell and the spectrum emitted by the solar cell. According to Eqs. 2.6 and 2.7, the PBS filter influences the solar cell efficiency. A carefully chosen PBS filter increases the current gain in photovoltaic systems with FCs significantly as shown for example in [6, 13, 17, 25]. On one hand, the increase follows from a reduced loss cone since the PBS filter reflects photons emitted by the dye as described in Figs. 2.1d,e. On the other hand, an effective PBS filter transmits all incoming photons with energies in the absorption range of the dye. In Sect. 3.2, I simulate the systems in their radiative limit assuming a perfect band stop which is energy selective only. Such omnidirectional photonic structures are realizable [26, 27] but are complex and

expensive.

State-of-the-art energy selective filters use layers of different refractive indices [28–31]. The simplest approach of these so-called Rugate filters is varying two different refractive indices. Figure 2.3 presents the transmission of filters fabricated with SiO_2 (refractive index $n_r = 1.5$) and Si_3N_4 ($n_r = 2.0$) [32]. Here, enhancing the number of layers from 5 to 11 decreases the transmission for the energy $E = 2.1$ eV from $T_D = 0.5$ to $T_D = 0.1$ (black lines). In order to keep photons emitted by the dye in the system, the transmission of Rugate filter is optimized for a defined energy range. The optimization holds for perpendicular incident photons, because photons with oblique angles see thicker layers. Thus, Rugate-filters always show a blue-shift in transmission for oblique angles represented in Fig. 2.3 by the grey lines [32, 33]. Therefore, photons with oblique angles are reflected at an higher energy range. I analyze the influence of an angular selectivity in an otherwise loss-free system in Sect. 3.3. The experiments in Sect. 4.2 analyze the benefits of a photonic structure for a photovoltaic system with a fluorescent collector. Here, I use a Rugate-filter with the transmittance T_D shown in Fig. 2.2d.

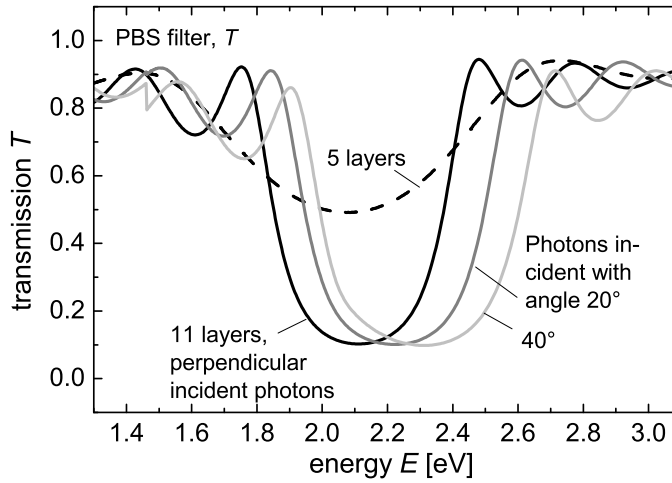


Fig. 2.3: Transmittance T_D of customized PBS filter. Using eleven instead of five layers decreases the transmission from $T_D = 0.5$ to $T_D = 0.1$. If the photons impinge with oblique angles, the transmission minimum shows a blue-shift from $E = 2.1$ eV to $E = 2.3$ eV [32].

2.4 Component Matching

In order to improve a photovoltaic module with a fluorescent collector and photonic structure, the system components need careful matching in two steps: i) scaling size and distance of the solar cell and ii) spectrally matching the fluorescent collector and the photonic structure to the solar cell and the incident spectrum.

i) The spatial concentration: The fluorescent collector distributes the emitted photons and guides them through the acrylic plate due to total internal reflection. Thus, photons reach solar cells far from their incident spot and the fluorescent collector works as a concentrator. Unfortunately, the distributional behavior is disadvantageous for underlying solar cells -the topic of this work. Here, the photons which normally directly hit the solar cell are distributed by the fluorescent dye. The experiments in Sects. 4.2 and 4.4 show that these losses above the solar cell are compensated if the surrounding photon catchment area is large enough.

In order to analyze the influence of the spatial concentration, the simulations in Sect. 3.2.3 assume a perfect spectral matching. Varying size and distance of the solar cells then leads to the conclusion that photovoltaic systems with fluorescent collectors are most effective for small distances between small solar cells.

ii) The spectral concentration: The fluorescent collector should absorb photons with an energy range where the solar cell's quantum efficiency is low compared to the energy range of the emitted photons. Such, the incoming photons gain higher output current. Also, with the shift into a more useful energy range the dye compensates radiative losses during emission.

In general, a fluorescent collector concentrates more photons if its reabsorption range is narrow. If the probability for a photon to be reabsorbed after its emission is low, its path length in the fluorescent collector is large. In Fig. 2.2b, the reabsorption range for the red fluorescent dye is marked. Here, the photon emission range lies between 1.8 eV and 2.2 eV. Emitted photons with energy $E > 1.96$ eV have an energy in the absorption range of the dye. The dye reabsorbs these photons. The concentration in a system with a fluorescent collector containing the red dye is higher than with yellow fluorescent dye (Fig. 2.2c). The yellow dye reabsorbs all emitted photons which then have a lower chance to reach a solar cell. The reabsorption experiment in Sect. 4.1 provides a simple set-up for measuring the reabsorption and therefore the concentration in a fluorescent collector.

The photonic structure should transmit all photons with energies in the absorption range of the dye and reflect all emitted photons. But, if a larger amount of the

incoming photons lie in the reflected energy range than in the transmitted range, more photons are kept outside the system than inside. Then, the photonic structure is disadvantageous.

For an exemplary component matching see App. A. As will be elaborately described in each section, spectrally matching the components is crucial for reaching the highest possible system efficiency.

Chapter 3

Monte-Carlo ray-tracing simulation

In order to model photovoltaic systems with fluorescent collector, I developed a ray-tracing simulation with MATLAB. Section 3.1 of this chapter describes the basics of the simulation with Monte-Carlo statistics. The simulation of photovoltaic systems with fluorescent collectors has two objectives. The idealization of system components allows the exploration of theoretical limitations for side- and bottom-mounted solar cells. Also, the Monte-Carlo ray-tracing simulation models experimental set-ups by handling realistic system components.

The simulations in Sect. 3.2 compare the classical set-up of fluorescent collectors with side-mounted solar cells [34] to a novel and technically less extensive set-up where the solar cells lie *under* the fluorescent collector [17]. In order to explore theoretical limitations, these simulations model the systems in their radiative limit [35]. Section 3.3 analyzes three loss mechanisms in otherwise loss-free systems: non-radiative losses in the dye, a non-perfectly reflecting back side mirror and an angular selective photonic structure on top [36].

3.1 Simulation method

Monte-Carlo simulations base upon the law of large numbers. Executing the same experiment a statistically relevant number of times obtains a result close to the expected value. Working with Monte-Carlo statistics is especially useful for numerically solving problems which are not or infeasible determined with analytical descriptions [37, 38].

In order to simulate the probability for photons to reach a solar cell attached to a fluorescent collector, photon rays are followed through the system. The program assigns statistically distributed properties to the traced photon rays by generating distributed random numbers. In order to sufficiently model the properties, three types of random number distributions need to be produced: Homogeneously distributed random numbers, a random number distribution regarding an analytical function and a random number distribution displaying discrete data. In the following, I explain the implementation of all three distributions.

Homogenous distribution

Homogeneously assigning random numbers to the photon rays displays an evenly illuminated collector surface, for example. Then, photons with randomly distributed coordinates $x \in [0, l]$, $y \in [0, l]$ hit a collector with edge length l .

A homogenous distribution of random numbers is also useful for selection processes, for example, if an energy selective photonic structure covers the top surface of the collector. Then, each photon occupies an energy E with a corresponding transmittance $0 < T_D(E) < 1$. The program assigns a random number $0 < \varrho < 1$ to the photons which is homogeneously distributed for each energy value E . The system transmits rays with $\varrho \leq T_D(E)$ and reflects rays with $\varrho > T_D(E)$.

Another example is the distribution of the spherical angle ϕ for photons emitted by the dye. In contrast, as clarified in App. B, a homogeneously distributed angle θ would lead to an unbalanced fluorescent emission sphere.

Inverse function

In order to evenly fill the emission sphere of the fluorescent dye, the photon rays need the spherical angle $0 < \theta < \pi$ to be distributed with the probability $p_\theta = \sin \theta/2$. Integrating this probability

$$\Pi(\theta) = \frac{1}{2} \int_0^\theta \sin \theta d\theta = \frac{1}{2}(1 - \cos \theta) \quad (3.1)$$

describes the distribution of the spherical angle θ . Here, $\Pi(\theta)$ is the cumulative distribution probability and is strictly increasing on the interval $[0, 1]$. Generating the inverse function

$$\theta(\Pi) = \arccos(1 - 2\Pi) \quad (3.2)$$

derives the random numbers of this distribution. Equation 3.2 maps the homogeneously distributed random numbers $\Pi(\theta) \in [0, 1]$ on the sine-like distributed random numbers $\theta(\Pi) \in [0, \pi]$.

Whenever a property of the photovoltaic system is describable with an analytical expression and the inverse function is feasible, the described method achieves a proper distribution of random numbers. Other examples are the energy selective absorption of photons in the dye which follows Beer's law or the subsequent emission for which Kirchhoff's law applies.

Inversion of discrete values

The simulation of real experiments executed in Sects. 4.1 and 4.2 requires the implementation of measured absorbance A and photoluminescence PL data of the dye in the Monte-Carlo simulation. In Sect. 4.3, an AM1.5G spectrum falls onto the experimental set-up. These properties have no analytical description, and the random numbers require discrete distributions. Thus, adapting the Monte-Carlo simulation to realistic systems requires the handling of discrete values. The simulation treats discrete data with the inversion method [13]. Here, tabulated data $D(E)$ for each energy E is cumulative summarized and normalized

$$\Delta(E) = \frac{\sum_{E'=E_{\min}}^E D(E')}{\sum_{E'=E_{\min}}^{E_{\max}} D(E')} \quad (3.3)$$

with the energies E_{\min} and E_{\max} denoting the lower and upper limit of $D(E)$. Note, that Eq. 3.3 is similar to Eq. 3.1 but summarizes discrete values instead of integrating an analytical function. The cumulative frequency $\Delta(E)$ is strictly increasing on the interval $[0, 1]$. The inversion $E(\Delta)$ of $\Delta(E)$ is carried out by simply exchanging the column of numbers. Thus, $E(\Delta) \in [0, 1]$ allows the transformation of equally distributed random numbers onto the statistically distributed random numbers of $D(E) \in [E_{\min}, E_{\max}]$.

Ray-tracing

The ray-tracing program typically handles a number $N_{\text{in}} = 5 \times 10^4$ photons in parallel. After entering the system, the dye absorbs the photons regarding the assumed absorption behavior. The re-emitted photons are either reabsorbed by the dye or hit one of the collector surfaces. At an uncovered surface, the photon is subject to total internal reflection if $\theta > \theta_c$ with $\sin(\theta_c) = 1/n_r$. In the presence

of a photonic band stop (PBS) filter, the photon is reflected according to the filter properties. Non-reflected photons are lost and the number N_{em} of photons emitted through a collector surface is increased accordingly. Also, a surface covering with a mirror is possible. Then, photons are reflected according to the modeled reflectance behavior. If a photon hits solar cell area, its probability to be collected depends on the chosen quantum efficiency of the solar cell. The program runs until all photons are collected by the solar cells, lost by re-emission from the collector surface, by non-radiative recombination in the dye, or by reflection losses at the mirrors. All the lost photons are summed up by the numbers N_{em} , N_{nr} , N_{rl} and the final result is $N_{\text{in}} = N_{\text{em}} + N_{\text{nr}} + N_{\text{rl}} + N_{\text{coll}}$ as well as the collection probability

$$p_c = N_{\text{coll}}/N_{\text{in}}. \quad (3.4)$$

Energy resolving the collection probability p_c , allows the calculation of the short circuit current density

$$J_{SC} = q \sum_{E=E_{\text{min}}}^{E_{\text{max}}} p_c(E)QE(E)\Phi_{\text{inc}}(E) \quad (3.5)$$

with the quantum efficiency QE of the solar cell and the energies E_{min} and E_{max} denoting the lower and upper limit of the regarded spectrum $\Phi_{\text{inc}}(E)$. With Eqs. 2.1 to 2.4, the Monte-Carlo ray-tracing model leads to the photovoltaic efficiency of the solar cell in the system analog to Sect. 2.1.

The loss and collection probability of photons depends strongly on the system parameters like absorption and emission in the dye, the solar cell's quantum efficiency, transmission of a PBS filter and even the incident photon angles and spectra. Section 3.2.1 explains highly idealized system parameters. The Monte-Carlo ray-tracing simulations use these idealizations in Sect. 3.2 and explore maximum collection probabilities theoretically achievable with solar cells attached to fluorescent collectors.

In Sects. 4.1, 4.2 and 4.3, Monte-Carlo ray-tracing simulations model real experiments. For this purpose, the system component properties are described with measurement data as elaborated in each section. The good accordance of the experimental and the simulated results proves that the Monte-Carlo ray-tracing program is a powerful tool to describe photovoltaic systems with fluorescent collectors.

3.2 Systems in their radiative limits

In this section, fluorescent photovoltaic collectors are examined theoretically with the help of Monte-Carlo simulations. The classical construction of mounting solar cells on each side surface of the collector is compared to alternative set-ups: solar cells only partly cover the collector side surfaces or they are mounted on the collector back surface.

The technological potential of fluorescent collectors (FCs) was examined already in the late 1970s and early 1980s as described by the review article of Goetzberger and Wittwer [5]. Recently, the basic idea has regained some interest in the context of efforts to build photovoltaic structures exceeding the classical efficiency limitations by the use of up- and down-converting dyes [39,40]. Theoretical tools to describe FCs thermodynamically have been developed [41–43]. Recently, numerical approaches analyzing the FC behavior gain more interest [7,44]. In order to estimate theoretical limitations, the photovoltaic systems with FCs have been highly idealized. However, realistic setups show loss mechanisms which need to be considered. The classic idea of assembling an FC in a photovoltaic system is based on its behavior of guiding emitted photons to the sides. Therefore, the classical setup mounts solar cells to the collector sides [6,25,34,45–47]. Technically, it seems less extensive to apply and connect solar cells at the bottom side of the collector. Experimentally, fluorescent collectors and photonic structures on top of solar cells prove to raise the current gain [17].

This section uses Monte-Carlo ray-tracing simulations for a comparison of the classical side-mounted system to a system where solar cells cover the FC back side. In order to find the maximum photon collection theoretically achievable, I assume only radiative losses as will be explained in the next section. The side-mounted system performs better in most cases, especially at larger collector sizes. However, for both systems the maximum collection probability for photons $p_c = 97\%$ is only achieved in the presence of a back side mirror and a photonic band stop (PBS) filter at the collector top surface acting as an energy selective filter. This maximal photon collection occurs in the statistical limit. Here, numerous small solar cells cover the FC with nearby spaces. Such a small-scale system is more favorable than a system with few large-scaled solar cells taking the same coverage fraction. The maximal number of collected photons is similar in a photovoltaic system with neither FC nor PBS, but the assembly saves 99% of solar cell area.

3.2.1 System geometries and idealized components

Figures 3.1a-d show the geometry of fluorescent collectors in the photovoltaic system analyzed in the following sections. Figure 3.1a depicts the conventional system [6, 25, 34, 45–47] with all four collector side surfaces fully covered with solar cells. Every increase of the collector length l in x - and y -direction, normalized to the collector thickness d , leads to a decreased coverage fraction

$$f = A_{\text{cell}}/A_{\text{coll}} = 4d/l \quad (3.6)$$

with the cell area $A_{\text{cell}} = 4dl$ and the collector aperture $A_{\text{coll}} = l^2$. Photons at the collector sides, for instance at (l, y_s, z_s) for the right collector side in Fig. 3.1a, are collected by the side-mounted solar cells.

Figure 3.1b shows an FC of length l and thickness d with the collecting solar cells only partially covering the side surfaces. For this configuration, the coverage fraction is

$$f = 4sd/l^2 \quad (3.7)$$

with the side length s of the solar cells. A mirror covers the FC back side. For this geometry, collection takes place only if the photon hits the solar cell, e.g. $y_s \leq s$, at the right surface.

The novel collector design of Fig. 3.1c uses quadratic solar cells with a side length s at the back side of the FC [17]. Thus, the solar cells in this bottom-mounted system cover a fraction

$$f = s^2/l^2 \quad (3.8)$$

of the surface. The remaining parts of the back side are covered with a reflector. The bottom-mounted solar cells collect photons if $x_s \leq s$ and $y_s \leq s$ is fulfilled.

The systems in Figs. 3.1b,c are repeated periodically in x - and y -direction. Photons hitting a collector side enter the opposed side, i.e. the photon is re-injected at the respective facing side with unchanged spherical angles (θ, ϕ) . Thus, photons traversing the collector see solar cells with a defined periodicity as exemplary shown for the bottom-mounted system in Fig. 3.1d.

The idealized simulations in Sect. 3.2 explore theoretical limitations of photovoltaic systems with fluorescent collectors and optional photonic band stop (PBS) filter. Figure 3.2 depicts the idealized system components. To allow the comparison between situations with and without PBS, photons impinge with energies $E = E_1$ only. Thus, at the beginning all incident photons are set to energy E_1 . All photons

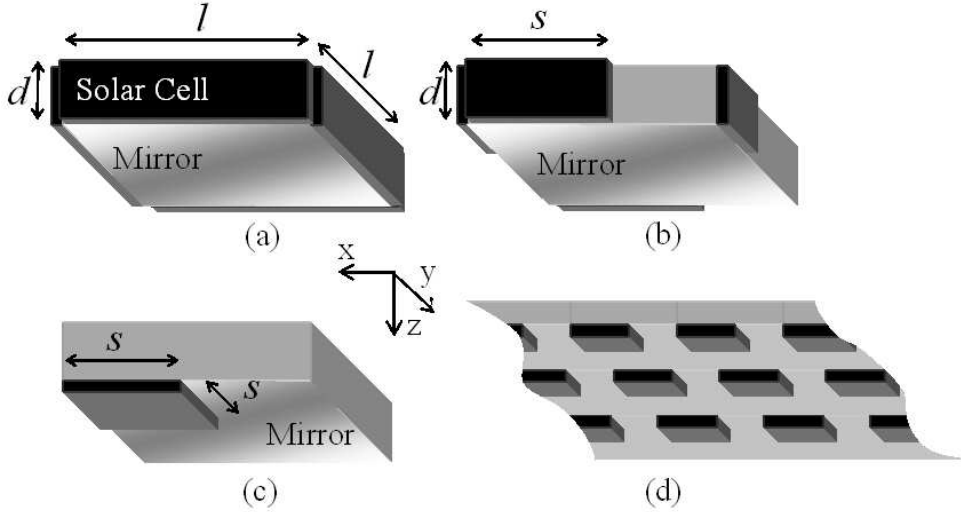


Fig. 3.1: Sketch of the fluorescent collector geometries compared in the following sections. a) Fluorescent collector geometry modeled in this section: solar cells cover all four sides of the collector fully. Therefore, increasing normalized collector length l/d decreases coverage fraction $f = 4ld/l^2$. Mirror covers the back side of collector. A photonic band stop (PBS) filter can be placed on top of the concentrator optionally. b) Side-mounted FC system where only a fraction of the collector side surfaces is covered with a solar cell area $A_{\text{cell}} = sd$. A mirror covers the bottom of the collector. c) Bottom-mounted collector with the solar cell area $A_{\text{cell}} = s^2$. The space between the cells at the FC bottom is covered by a mirror. d) Both systems are assumed to be periodically repeated in x - and y -direction. Exemplary, a detail of the bottom-mounted system shows the periodicity of applied solar cells.

enter into the collector with normal incidence at a random coordinate (x, y) with $0 < x < l$ and $0 < y < l$. The fluorescent dye absorbs incoming photons with a stepwise increasing absorption constant α from zero at energies $E < E_2$ to a value α_2 for $E \geq E_2$ and a further increase to α_1 for energies $E \geq E_1$. The emission coefficient e is linked to the absorption coefficient α via Kirchhoffs law

$$e(E) = \alpha(E)n_r\Phi_{\text{bb}}(E) \quad (3.9)$$

with the black body spectrum

$$\Phi_{\text{bb}}(E) = \frac{2}{h^3c^2} \frac{E^2}{e^{E/kT} - 1} \approx \frac{2E^2}{h^3c^2} e^{-E/kT} \quad (3.10)$$

where n_r is the refractive index of the collector material, h is Planck's constant,

c the speed of light and $kT = 0.026$ eV the thermal energy corresponding to the temperature $T = 300K$ of the collector and its surroundings [48].

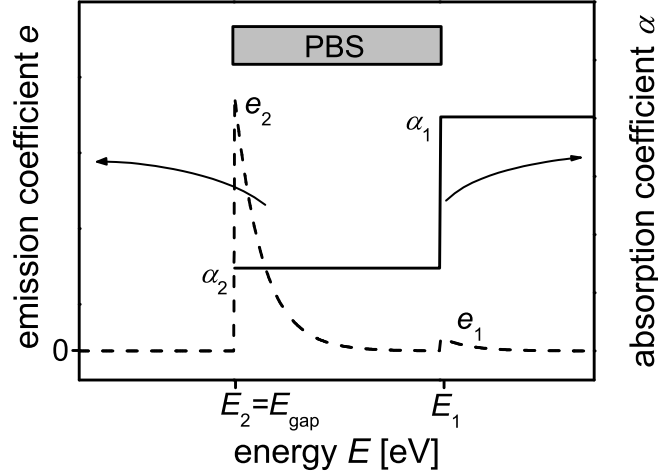


Fig. 3.2: Sketch of the absorption and emission behavior as assumed in this section. The dye absorption is given by a step function. Incoming photons have the energy E_1 and a high absorption coefficient α_1 . The lower absorption coefficient α_2 holds for the lower energy E_2 and leads with Kirchhoffs law (Eq. 3.9) to a high emission coefficient e_2 . The model also features the possibility of an energy selective photonic band stop (PBS) that keeps the emitted photons in the FC system. The solar cells has the band gap $E_{\text{gap}} = E_2$ and a quantum efficiency $QE = 1$ for all incoming photons with energy $E \geq E_{\text{gap}}$.

This absorption/emission scheme is the simplest approach to describe the detailed balance limit of FCs with a continuous spectral photovoltaic action [45, 46, 49]. The absorption and emission dynamics occur in terms of a two-level scheme considering the emission probabilities

$$p_1 = \frac{\alpha_1}{p} \int_{E_1}^{\infty} E^2 \exp\left(-\frac{E}{kT}\right) dE = \frac{\alpha_1 p_{\infty}(E_1)}{p} \quad (3.11)$$

and

$$p_2 = \frac{\alpha_2}{p} \int_{E_2}^{E_1} E^2 \exp\left(-\frac{E}{kT}\right) dE = \frac{\alpha_2 (p_{\infty}(E_2) - p_{\infty}(E_1))}{p} \quad (3.12)$$

for photon emission by the fluorescent dye in the range of photon energies $E > E_1$ and $E_1 > E > E_2$, respectively. The definition

$$p_{\infty}(E_x) = \int_{E_x}^{\infty} E^2 \exp\left(-\frac{E}{kT}\right) dE = kT(2(kT)^2 + 2E_x kT + E_x^2) \exp\left(-\frac{E_x}{kT}\right) \quad (3.13)$$

as well as the normalization factor p such that $p_1 + p_2 = 1$ holds in Eqs. 3.11 and 3.12. The choice of the energies E_1 , E_2 and the absorption coefficients α_1 , α_2 leads to the emission probabilities $p_2 \gg p_1$, in contrast to the absorption coefficients $\alpha_2 \ll \alpha_1$. Due to the dominance of the exponential factor in Eq. 3.13 the approximation

$$\frac{p_1}{p_2} \approx \frac{\alpha_1}{\alpha_2} \exp\left(\frac{E_2 - E_1}{kT}\right) \quad (3.14)$$

is valid. Thus, a choice of an energy difference $\Delta E = E_1 - E_2 = 200$ meV and of absorption coefficients $\alpha_1 = 100\alpha_2$ still ensures $p_2 \approx 20p_1$. In the following, the assumptions apply $E_1 = 2.0$ eV, $E_2 = 1.8$ eV and absorption coefficients $\alpha_1 = 3/d$, $\alpha_2 = 0.03/d$. Therefore, the system provides a high emission coefficient e_2 for photons with energy E_2 and a significantly lower emission coefficient e_1 for photons with high energies.

Figure 2.1c shows that emitted photons which impinge at the top surface with an incident angle θ lower than the critical angle θ_c for total internal reflection leave the collector. The application of a photonic band stop (PBS) filter avoids this loss mechanism by acting as an energy selective filter [50–52]. As indicated in Fig. 3.2, the PBS filter in the idealized simulation has a reflectance $R = 1$ and a transmission $T_D = 0$ for photon energies $E < E_{\text{th}}$. For the other part of the spectrum $R = 0$ and $T_D = 1$ is assumed. Therefore, E_{th} denotes the upper cut-off energy of the filter. As depicted in Fig. 3.2, I assume $E_{\text{th}} = E_1$. This highly idealized assumption is made in order to demonstrate the principal action of photonic band stop filters on FC systems. In order to examine the influence of an angular selectivity, I vary the reflection cone of the filter. Then, $\theta_{\text{pbs}} < \theta_c$ and only photons with $E = E_1$ and $\theta < \theta_{\text{pbs}}$ are guided to the sides. All other rays are subject to total internal reflection only.

In Fig. 3.1c, solar cells partly cover the collector back side. The remaining part as well as the bottom side of the system geometries in Figs. 3.1a,b is mirrored and reflects photons with a probability p_r with $p_r = 1$ for a perfect mirror and $p_r < 1$, otherwise.

The ray-tracing model identifies all photons reaching solar cell area. These photons add to the number N_{coll} of collected photons. Throughout the modeling of idealized photovoltaic systems, solar cells collect 100% of photons incident with energy E higher than the solar cell band gap E_{gap} . In order to analyze the principle limitations of applying FCs to photovoltaic systems, I choose $E_{\text{gap}} = E_2 = 1.8$ eV as indicated in Fig. 3.2.

3.2.2 Classical set-up: side-mounted solar cells

This subsection studies the influence of the collector and cell geometry on the photon collection properties of a classical collector system where the fluorescent concentrator is modeled with all edges fully covered with solar cells and the back side with a mirror as shown in Fig. 3.1a. Figure 3.3 shows the dependence of the photon collection probability p_c on the normalized collector length l/d calculated for side-mounted solar cells with PBS (open symbols) and without PBS (full symbols). Aside from the radiative limit with a probability $p_{nr} = 0$ for non-radiative processes after the absorption of a photon, also non-radiative recombination in the dye is considered by assuming $p_{nr} = 0.5, 0.95$.

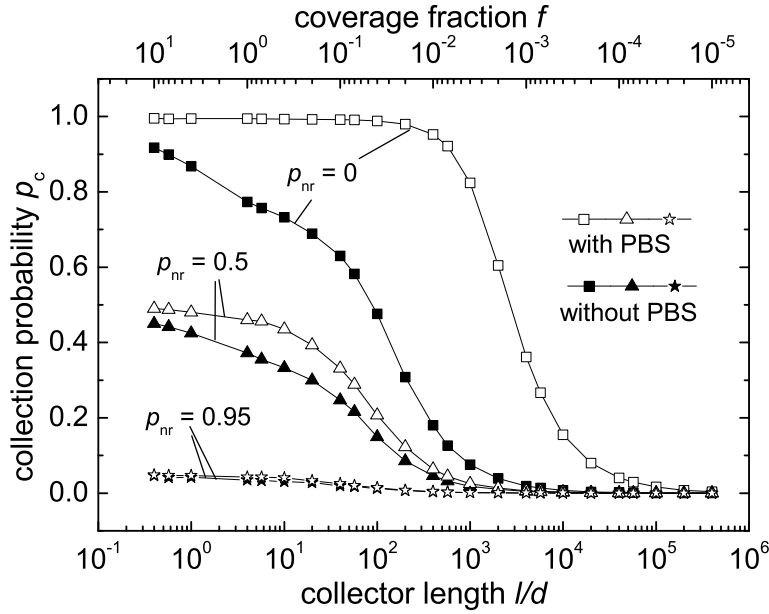


Fig. 3.3: Dependence of the collection probability p_c of a fluorescent collector fully covered with solar cells at its sides on the collector length l normalized to the thickness d . A perfect mirror covers the back side. In systems with a photonic band stop (PBS, open symbols) p_c is higher than in those without PBS (full symbols). For a system with PBS in its radiative limit ($p_{nr} = 0$) a collection probability p_c close to unity remains normalized collector lengths $l/d < 500$. In contrast, the system without PBS has a maximum p_c only slightly above 90%. With increasing collector length l/d which means a decreased coverage fraction f (top axis), the collection probability p_c decreases immediately. Considering non-radiative recombination in the dye ($p_{nr} > 0$) deteriorates p_c in all cases.

Most importantly, applying a PBS leads to a considerably higher photon collection. The reason lies in the suppressed emission from the top surface as shown in Fig. 2.1. This radiative loss occurs in the uncovered system whenever a photon falls into the critical angle θ_c of total internal reflection. In the system with PBS the photon additionally must be emitted at an energy $E \geq E_1$ which happens with a low but, for reasons of detailed balance, non-zero probability. The suppressed emission also results in high photon collection probabilities p_c of systems with PBS at larger collector lengths l/d . The systems without PBS collect considerably less photons already for slight increases of l/d . With increased l/d the number of photons that are absorbed by the dye more than once increases. Each absorption event leads to θ -randomization of the re-emitted photon and, in consequence, to a certain probability that the photon is lost by emission from the collector surface. The loss through the top surface, as mentioned above, is much more likely for the systems without PBS than for those with PBS. Therefore, the deterioration of p_c by large scales is higher in the uncovered systems. Figure 3.3 also shows the impact of non-radiative recombination in the dye ($p_{nr} = 0.5$ and 0.95). The system covered with PBS is especially sensitive to non-radiative recombination at $l/d > 100$. Before a photon reaches the solar cell at the collector side, it is most likely only absorbed once in small-scaled systems. Here, the maximum of p_c decreases proportionally to $(1 - p_{nr})$. But in large-scaled systems, the repeated reabsorption of photons leads, aside from more radiative losses, to a higher risk of non-radiative recombination. Whereas in the non-radiative case a value of $p_c > 90\%$ remains up to a normalized collector length $l/d \approx 500$, for $p_{nr} = 0.5$ the systems achieve $p_c \approx 50\%$ only for $l/d = 1$. A further increase of p_{nr} leads to lower collection probabilities significantly lower than 90%. As radiative losses are low in the systems with PBS the relative importance of non-radiative losses is higher. In contrast, the radiative emission losses are already high in the systems without PBS. Therefore, the deterioration in p_c caused by non-radiative recombination is not as significant over the whole range of l/d as in the systems with PBS. A larger p_{nr} diminishes the differences in p_c for the systems with and without PBS. However, applying a PBS is always advantageous, especially for the retardation of reaching the large-scale limit.

3.2.3 Novel concept: bottom-mounted solar cells

This subsection introduces the novel concept of mounting solar cells to the back side of the fluorescent collector. Also, it compares the collection probability in the

bottom-mounted system and in the side-mounted system and explores the influence of non-radiative dye.

Scaling effect

The classical side-mounted collector geometry has a strict relation between the collector length l and the cell coverage fraction $f = A_{\text{cell}}/A_{\text{coll}} = 4d/l$. In this subsection, I examine the bottom-mounted system shown in Fig. 3.1c where both quantities occur independently. For Fig. 3.4 the coverage fraction $f = 0.01$ is fixed and the collector length l is varied. Because of $f = s^2/l^2$, the cell side length s is $s = lf^{1/2}$.

Figure 3.4 demonstrates that the collection probability p_c at constant coverage fraction f drastically depends on the collector length l . The data in Fig. 3.4 display asymptotic behavior in both limits (small and large ratios l/d , dashed lines). A wide transition regime between the two limiting cases occurs where the collection probability p_c changes from high values at small l/d to significantly smaller values at large l/d . Such a behavior is typical for spatially extended inhomogeneous systems. If the characteristic feature length (here the collector length l) is large with respect to the length scale that is characteristic for interactions within the system (here the mean free path of photons), the system can be looked at as a parallel connection of spatially separated subsystems without interaction. The collection probability $p_{c,ls}$ in this *large-scale limit* [53] is then the weighted average of a portion f that has a (local) p_c of a collector with full back coverage (i.e. $p_c \approx 1$, for the system with $p_{nr} = 0$) and a portion $(1 - f)$ with $p_c = 0$. This is why the collection probability p_c of the system with PBS (open symbols in Fig. 3.4) approaches the coverage fraction f in this limit.

In contrast, approaching the *small-scale limit* ($l < 1/\alpha_2$), any ray, reflected forth and back within the collector, has often the possibility to hit a cell at the collector's back. In this situation, the system might be looked at as spatially homogeneous with statistical cell coverage at its back. In fact, the value of $p_{c,ss}$ in the small-scale limit is consistent with quasi-one-dimensional computations that simulate the back-side mounted solar cells by a probability $p_c = f$ for a photon at the back side to be collected by the cells [13]. Therefore, this case is denoted as the statistical limit.

The introduction of non-radiative recombination ($p_{nr} = 0.08$ in Fig. 3.4) leads to a deterioration of the collection probability in all cases. As already seen in Fig. 3.3, the system with PBS is much more sensitive to losses in the dye because of its overall high collection probability in the radiative limit. Especially important is

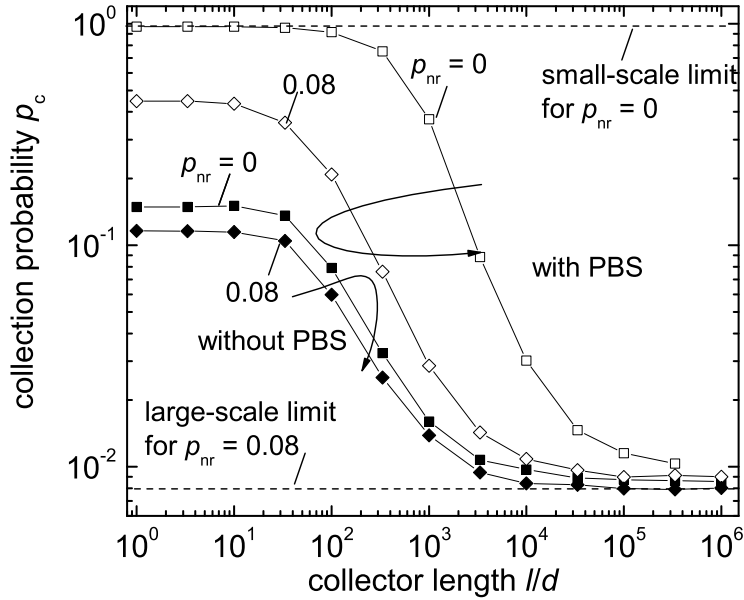


Fig. 3.4: Collection probability p_c of the fluorescent collector geometry with solar cells mounted at the bottom of the collector (Fig. 3.1c). The coverage fraction f is kept constant at $f = 0.01$ and the normalized collector length l/d is varied. All data feature a transition between two asymptotic situations at low and high ratios l/d . Only the systems with a photonic band pass (PBS, open symbols) achieve $p_c > 0.5$ at low ratios of l/d . For these systems, the maximum p_c as well as the transition from the small-scale to the large-scale behavior is strongly dependent on the non-radiative recombination probability p_{nr} . The systems without PBS (full symbols) have already a relatively low $p_c < 20\%$ even in the more favorable case of $l/d < 10$. Accordingly, the sensitivity to the introduction of non-radiative recombination in the dye ($p_{nr} > 0$) is less pronounced.

the influence of a finite p_{nr} on the transition between the small-scale to the large-scale limit. Whereas with $p_{nr} = 0$ all systems with $l/d = 100$ yield the same high collection probability the limit for $p_{nr} = 0.08$ reduces to $l/d = 10$. All data in Fig. 3.4 represent the same coverage $f = 0.01$, i.e. the same amount of solar cell area used per unit collector area. Nevertheless, the collection probability strongly depends on the chosen size of collector and solar cell. A proper scaling of these quantities is therefore necessary to tune the collection probability and, finally, the collector performance to its optimum. The experiments in this thesis in Sects. 4.2 and 4.4 confirm the importance of properly scaling size and distance of solar cells in

photovoltaic systems with fluorescent collectors.

Comparison to side-mounted system

The bottom-mounted system displayed in Fig. 3.1c instructively separates the scaling effect from the consequences of varying cell coverage. In order to compare this bottom-mounted FC with a side-mounted system, the side-mounted system displayed in Fig. 3.1b achieves the decoupling of coverage fraction and collector length. Keeping a constant coverage fraction f upon variation of the collector length l requires the adjustment of the solar cell side length s to

$$s = f \frac{l^2}{4d} \quad (3.15)$$

likewise $s/d = f(l/d)^2/4$ for the normalization of all quantities to the collector thickness d .

The maximum coverage fraction f_{\max} for the side-mounted system is given when the solar cell side length s equals the collector length l and the system in Fig. 3.1b becomes identical to the system in Fig. 3.1a. Increasing the collector length further leads then to a decreased coverage fraction. Figures 3.5a,b compare the collection probabilities of side- and bottom-mounted systems for a fixed collector length $l = 10d$ (Fig. 3.5a) and $100d$ (Fig. 3.5b). For the side-mounted system coverages up to $f_{\max} = 4d/l = 0.4$ and 0.04 , respectively are modeled.

Figure 3.5a shows that without applied PBS the side-mounted system performs better for low coverage fractions. The application of PBS on top of the collector yields higher photon collection for the bottom-mounted system in this region. In the region of $f \geq 10^{-2}$ both systems reach collection probabilities close to 100%. As shown in Fig. 3.4 a collector with length $l = 10d$ is with bottom-mounted solar cells in the statistical limit. The bottom-mounted system benefits from the application of PBS for the reduction of solar cell area.

Figure 3.5b shows the comparison of the two systems with collector length $l = 100d$. Since the side-mounted system performs as in Fig. 3.5a, it obviously still works in the statistical limit whereas the bottom-mounted passes into the large-scale region. Therefore, the FC system with solar cells covering the sides performs better at all coverage fractions with or without PBS. For small coverage fractions f the application of PBS assimilates the collection probabilities.

In conclusion, the bottom-mounted solar cells collect as many photons as the side-mounted solar cells in the small-scale limit. However, since the bottom-mounted

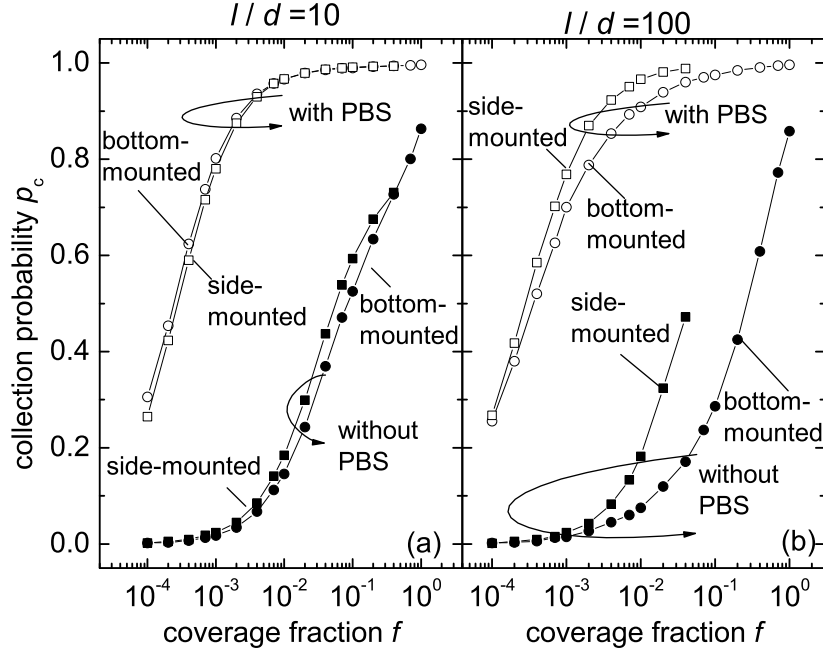


Fig. 3.5: Comparison of FC systems with solar cells at the sides or at the back as sketched in Figs. 3.1b and 3.1c. Both systems have a constant collector lengths l/d and the coverage fraction f is varied. a) For the collector length $l = 10d$ the side-mounted system is only modeled up to coverage fraction $f_{\max} = 4d/l = 0.4$ where the cells cover all sides completely. As seen in Fig. 3.4 the bottom-mounted system works in the small-scale limit. Side-mounted solar cells provide slightly higher collection probabilities for $10^{-3} \geq f \geq 4 \times 10^{-2}$ without the application of a PBS filter. Applying PBS eliminates the difference in collection probability p_c for high coverage fractions. Both systems achieve approximately 100% for coverage fractions $f \approx 1$. For coverage fractions $f \leq 10^{-2}$ mounting solar cells at the back side of FC is of slight advantage. b) The collector length $l = 100d$ reaches a maximum coverage fraction $f_{\max} = 4d/l = 0.04$ for the side-mounted system. Mounting solar cells at collector sides leads to higher collection probabilities for all cases. As shown in Fig. 3.4 for this collector length the bottom-mounted system is already in the transition regime to the large-scale limit whereas the side-mounted system obviously still remains in the small-scale limit.

systems leave the optimum small-scale limit at smaller collector lengths l/d , size and distance of their solar cells need to be smaller. As seen in Figs. 3.3 and 3.4, non-radiative losses in the dye significantly deteriorate the collection probability. The next section systematically adds different loss mechanisms to an otherwise ideal

system. In order to compare the influence of the losses in side-mounted systems with their influence in bottom-mounted systems, the next section uses the system geometries from Fig. 3.1b (solar cells partly covering the collector edges) and Fig. 3.1c (bottom-mounted solar cells).

3.3 Influence of loss mechanisms

The previous section analyzes the systems in their radiative limit and therefore calculates the theoretically highest possible collection probabilities. Figures 3.3 and 3.4 regard non-radiative losses in the dye for the system with fully side-mounted and with bottom-mounted solar cells, respectively. However, these two systems are not comparable as explained for Figs. 3.5a,b. In this section, the focus lies on the comparison of the side-mounted and the bottom-mounted collector geometries. In order to decouple the reduction of the covering fraction from the enlarging of the collector length, I compare solar cells partly covering the collector sides (Fig. 3.1b) with solar cells covering the back side of the collector (Fig. 3.1c). Monte-Carlo simulations calculate the photon collection in these photovoltaic systems. In each system, a mirror covers the bare back sides of both systems. On top lies optionally a photonic structure acting as an energy selective filter. This section analyzes ideal systems in the radiative limit as well as the influence of a non-perfect mirror at the back side and of a non-ideal reflection cone at the PBS filter.

In order to compare the side-mounted and the bottom-mounted system, I assume constant coverage fractions $f = 0.01$ for all simulations and an additional $f = 0.9$ for Figs. 3.8a,b. For the side-mounted system, the simulations are limited to a collector length $l = l_{\max} = 4d/f = 400d$ and $4.44d$ where the side length s of the solar cells equals the collector length l .

The results show that non-perfect reflection at the back side mirror causes a higher deterioration in the photon collection than non-radiative recombination in the dye discussed in the former sections. This is because in the analyzed systems the reabsorption is a rare event compared to a reflection at the back side. Therefore, the quality of the back side mirror merits especial care. Assuming a restricted reflection cone of the photonic band stop filter causes higher losses in the side-mounted system than in the bottom-mounted system. This is caused by the randomization of the photon angles during their emission from the dye. Thus, a good quality of the filter is especially necessary in systems with low coverage fraction of solar cells.

Non-radiative losses in the dye

Figures 3.6a,b examine the systems in their radiative limit with a probability $p_{nr} = 0$ for non-radiative losses and the influence of non-radiative recombination in the dye ($p_{nr} = 0.02, 0.08$ and 0.1).

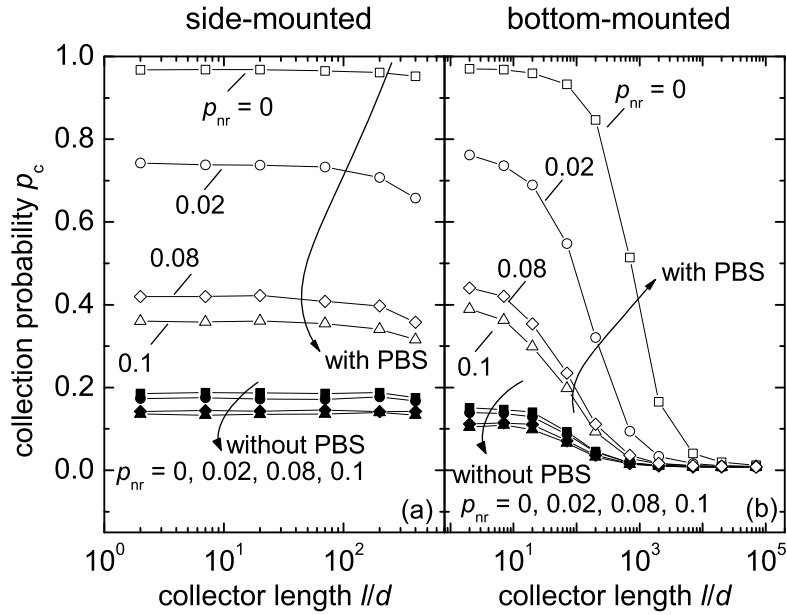


Fig. 3.6: Influence of non-radiative losses in the dye. a) Side-mounted system. The inclusion of non-radiative losses deteriorates the photon collection p_c in all cases. The effect is more significant in the system with applied PBS. b) Bottom-mounted system. The simulation covers a wider range of collector lengths. For small l/d the system behaves similar to the side-mounted system. Systems in their radiative limit show a significant drop in p_c for $l/d = 100$. The inclusion of non-radiative losses reduces this limit to $l/d = 10$.

Figure 3.6a shows the results for the side-mounted system. In the radiative limit, the application of a PBS increases the photon collection from $p_c \approx 19\%$ to $p_c \approx 95\%$. These values remain constant up to the maximal simulated collector length $l_{\max} = 400d$. This means that the reabsorption length in this system lies considerably under the collector length. The inclusion of non-radiative losses reduces p_c . The influence in the system with PBS is more significant than in the system without. As radiative losses are lower in the systems with PBS than in the systems without PBS, the relative decrease due to non-radiative losses is higher.

Figure 3.6b presents the results for the bottom-mounted system. At small col-

lector lengths, the system performs similar to the side-mounted system in Fig. 3.6a. Note, that the simulation covers a larger range of collector lengths l/d . Increasing the collector length l/d raises the number of reabsorption events in the dye. Every reabsorption process with a subsequent spatially randomized emission of photons causes losses due to total internal reflection as shown in Fig. 2.1. Therefore, large l/d deteriorates the photon collection significantly. Enlarging the systems degrades p_c even more than the inclusion of non-radiative recombination in the dye. However, the lowering in the photon collection occurs with $p_{nr} = 0$ at $l/d = 100$, but this limit reduces to $l/d = 10$ for $p_{nr} = 0.1$.

Reflection losses at mirror

Mirrors cover the collector back sides either fully in the side-mounted system or partly in the bottom-mounted system. Figures 3.7a,b depict the influences on the photon collection p_c of both systems for a reflection $R = 1$.

Figure 3.7a presents the results for the side-mounted system. Since less radiative losses occur in the system with PBS the contribution of non-radiative reflection losses at the back side mirror is more significant. Therefore, the decrease in the photon collection is higher.

Figure 3.7b shows the photon collections for the system with bottom-mounted solar cells. For small l/d the system behaves similar to the side-mounted system. The larger the system the more often a reflection takes place which increases the number of lost photons. Therefore, included reflection losses decrease the photon collection already at $l/d = 10$, whereas for a mirror with $R = 1$ this drop occurs at $l/d = 100$. In systems with coverage fraction $f = 0.01$ at any of the calculated collector length the reabsorption is a rare event compared to the number of reflections at the FC back side as the following example clarifies. Most photons emitted by the dye experience the absorption coefficient $\alpha_2 = 0.03/d$ as mentioned above. With $d = 3$ cm, a typical thickness for industrialized fluorescent collectors, the photons are reabsorbed after 100 cm. A photon emitted with an angle $\theta = 45^\circ$ hits a collector side every 4.2 cm. Since the coverage fraction $f = 0.01$ is very low, most likely the photon is reabsorbed before it hits a solar cell. Such, a photon with $\theta = 45^\circ$ is reflected 23 times before it is reabsorbed. Therefore, a non-perfect mirror has a stronger influence than an equally high non-radiative recombination loss in the dye. A reflection $R = 98\%$ at the back side mirror causes a drop $p_c \approx 70\%$ for small l/d which is higher than the drop $p_c \approx 25\%$ caused by the non-radiative recombination

loss as shown in Figs. 3.6a,b. Therefore, the used mirror has to feature a superior quality compared to the fluorescent dye.

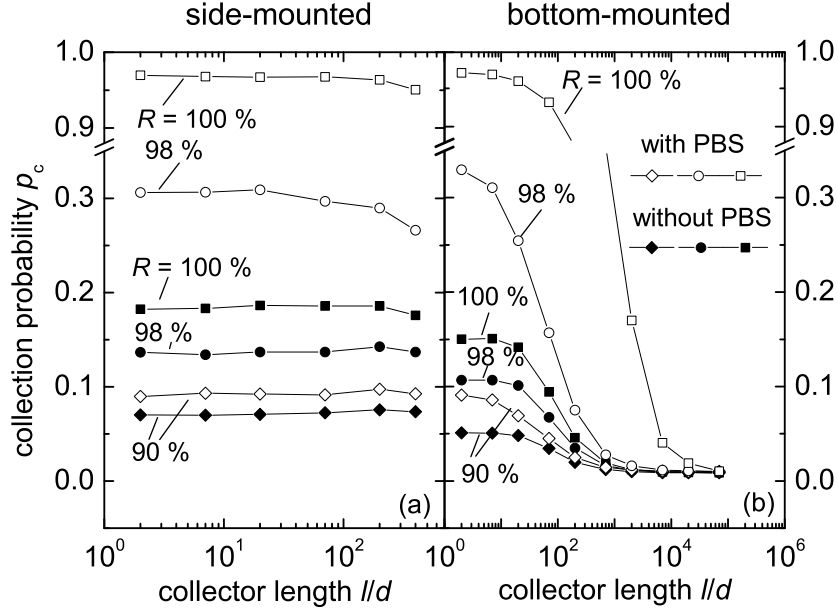


Fig. 3.7: Influence of non-perfect mirror at the back side of the FC in systems with a coverage fraction $f = 0.01$. a) Side-mounted solar cells. Inclusion of non-radiative losses in the dye decreases the photon collection significantly. The relative deterioration in a system with applied PBS is higher than in the system without PBS. b) Bottom-mounted solar cells. At small l/d the system shows a similar behavior as the side-mounted system.

Non-perfect photonic structure

Figures 3.8a,b present the results for a non-perfect photonic structure. In the simulations, the application of a photonic band stop as an energy selective filter increases the photon collection in all cases. However, in realistic filters blocking the photons depends not only on the energy but also on the angle of incidence of the photon (for example [54]). In order to analyze the influences of such a non-perfect PBS filter the angle of its reflection cone θ_{pbs} is varied. A perfect PBS ($\theta_{\text{pbs}} = \theta_c = 42.2^\circ$, see Fig. 2.1d) reflects every photon with energy E_1 regardless of its angle. A PBS with $\theta_{\text{pbs}} < \theta_c$ transmits rays with $E < E_1$ and $\theta_c > \theta > \theta_{\text{pbs}}$ which then add to the lost rays. Figures 3.8a,b outline the influence of smaller reflection cones ($\theta_{\text{pbs}} = 10^\circ$ and 20°) on side- and bottom-mounted systems with coverage fractions $f = 0.01$ and

0.9.

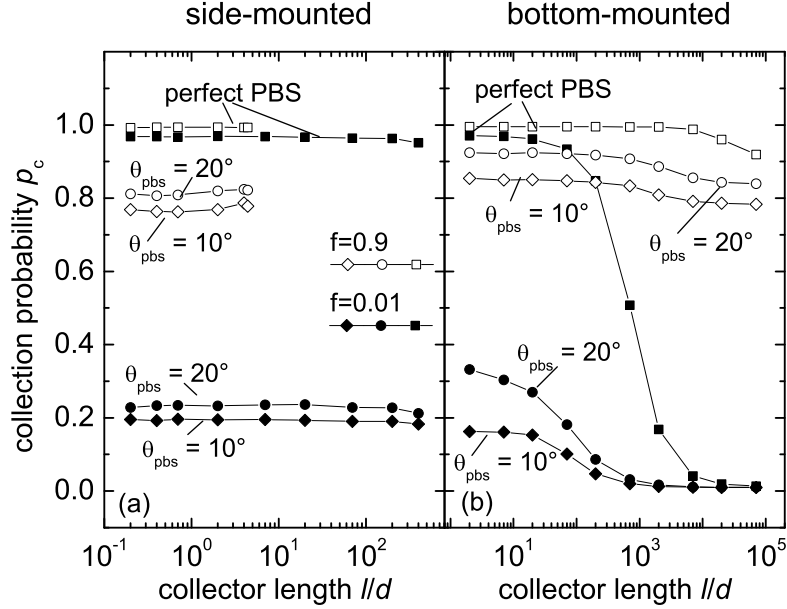


Fig. 3.8: Influence of a photonic band stop filter with angular selectivity. a) Side-mounted system. Coverage fraction $f = 0.9$ achieves higher photon collections p_c than $f = 0.01$ for all θ_{pbs} . b) Bottom-mounted system. For small scales the system shows a better performance than the side-mounted system, because this system benefits from the randomization of photon direction.

Figure 3.8a depicts the results for the side-mounted system. The application of a non-perfect PBS filter decreases the photon collection at all collector lengths. However, a relatively higher drop occurs for the system with $f = 0.01$. Here, a higher reabsorption rate occurs due to longer distances between the cells. Therefore, photons are more often re-emitted with their direction spatially randomized. The frequent randomization carried out also in unfavorable angles contributes to the number of lost photons.

Figure 3.8b presents the calculation for the bottom-mounted system. At small l/d this system collects more photons under the application of a non-perfect PBS filter than the side-mounted system. This is due to the effect that the unfavorable angles for the PBS are very favorable angles for solar cells at the FC back side. Therefore, the collection of a photon is more likely than in the side-mounted system. At large l/d the photon collection in the system with $f = 0.01$ drops more significant than

in the system with $f = 0.9$ which again is due to the larger distances between solar cells in the system with less solar cell area.

3.4 Conclusion and Outlook

Monte-Carlo simulations compare photovoltaic fluorescent collectors in side-mounted and bottom-mounted systems as well as the systems with or without the application of a photonic band stop filter on top. The filter greatly enhances the overall collection probability by suppressing emission of converted photons from the surface of the collector. Also, the sensitivity of the collector to repeated reabsorption and re-randomization of the fluorescent photons is reduced. The collection probability of systems with identical coverage fraction, i.e., the same amount of solar cell area per unit collector area is heavily influenced by the scaling of the solar cell size. Many small solar cells generally perform better than few large solar cells with the same overall area (scaling effect). The systems in their radiative limits are compared to systems which include loss mechanisms. The comparison of collectors with solar cells mounted at the collector side to a system with the cells at the bottom shows that in most cases the side-mounted system displays a higher collection efficiency. A non-perfect reflection at the back side mirror causes a higher deterioration in the photon collection than a comparable non-radiative recombination in the dye. This is because in the analyzed systems the reabsorption is a rare event compared to a reflection at the back side. Therefore, the quality of the back side mirror merits especial care. Assuming a restricted reflection cone of the photonic band stop filter causes higher losses in the side-mounted system than in the bottom-mounted system which is caused by the randomization of the photon angles during their emission from the dye. All loss effects are especially significant for systems without a filter. A good quality of the filter is especially necessary in systems with low coverage fraction of solar cells. In comparison to the classical side-mounted system, the system with solar cells at the back side performs equally good for small scales. Therefore, applying fluorescent collectors technically less extensive *on top* of solar cells is a promising approach if the solar cells are properly scaled in size and distance. The experiments undertaken in the next sections follow this idea by applying fluorescent collectors on top of amorphous and crystalline silicon solar cells.

Chapter 4

Experimental results

In the following sections, I present five experiments to explore the benefits of fluorescent collectors. The reabsorption measurement in Sect. 4.1 is a novel concept and simple approach to describe the concentration of photons characteristic for a fluorescent collector. The reabsorption coefficient derived with this experiment is used in Sect. 4.2 to predict the amount of photons collected by a solar cell. Section 4.3 discusses the differences between geometrical and fluorescent concentration. Finally, Sects. 4.4 and 4.5 show two applications of fluorescent dye in crystalline silicon solar cell modules which increase the efficiency.

4.1 Measuring and modeling reabsorption

This section introduces a novel and easy characterization method for the reabsorption processes in a fluorescent collector. An analytical fit extracts the reabsorption coefficient characteristic for the analyzed collector which then is used in Sect. 4.2.3 to predict light beam induced current (LBIC) measurements.

The ability of a fluorescent collector (FC) to concentrate photons depends strongly on the reabsorption processes in the dye [24]. This section analyzes the reabsorption in a fluorescent collector (Acid Green, 6T66 by PerspexTM [22]) with absorption A and photoluminescent emission PL as depicted in Fig. 4.1 and a thickness $d = 3$ mm. The reabsorption range lies in the marked area in Fig. 4.1. Here, emitted photons have an energy the dye absorbs. Thus, photons emitted in this energy range have a chance to be reabsorbed by the dye. Photons emitted in the reabsorption range where the absorbance A is low have long path lengths in the fluorescent collector. The longer the path length in the system, the higher the possible distance between

the photon incidence spot and a solar cell. In other words, collectors with low reabsorption concentrate more photons.

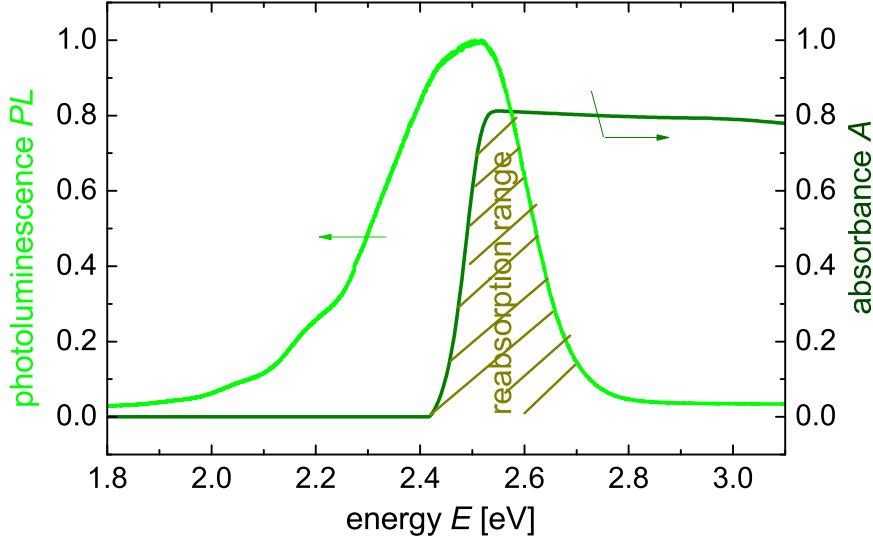


Fig. 4.1: Absorbance A and photoluminescent emission PL of the fluorescent collector analyzed in this section. Photons emitted in the marked area have the chance to be reabsorbed by the dye molecules.

In order to measure the concentration in a fluorescent collector, usually light beam induced current (LBIC) measurements are carried out [17, 24, 25]. LBIC-measurements are time-consuming and need a sophisticated set-up (see Sect. 4.2.1). This section presents a simple set-up quickly providing images to which an analytical fit determines the reabsorption coefficient of the investigated fluorescent collector. In Sect. 4.2.3, I insert the results for the reabsorption coefficient from this section into an analytical description for the LBIC-measurements. The very good agreement of the analytically derived with the measured results proves that the fast reabsorption measurement developed in this section provides a powerful tool to substitute extensive LBIC-measurements.

4.1.1 Measuring reabsorption in fluorescent collectors

Figure 4.2 sketches the principle of the reabsorption measurement. Light of an LED hits the collector top surface at a circular opening with diameter $d_{\text{LED}} = 5$ mm within a black cover. A black circle out of paperboard covers the back surface of the collector with diameter $d_c = d_{\text{LED}}$, such that photons transmitted by the collector

are absorbed by the black material and therefore invisible to the camera (Fig. 4.2, ray #1). Ray #2 indicates that photons absorbed once and emitted with an angle smaller than the angle of total internal reflection $\theta_c = 42.2^\circ$ (from a refractive index $n_r = 1.5$ for acrylic glass) leave the collector back side for

$$x < x_{\text{reabs}} = d \tan(\theta_c) = 2.7 \text{ mm} \quad (4.1)$$

where $d = 3 \text{ mm}$ is the collector thickness. Photons emitted with an angle $\theta > \theta_c$ need to be reabsorbed in order to have a chance to leave the collector through the back surface. Therefore, photons reabsorbed at least once as rays #3 and #4 leave the collector back side at $x > x_{\text{reabs}}$. A camera with opening angle γ detects all photons leaving the collector at the back surface outside the black circle.

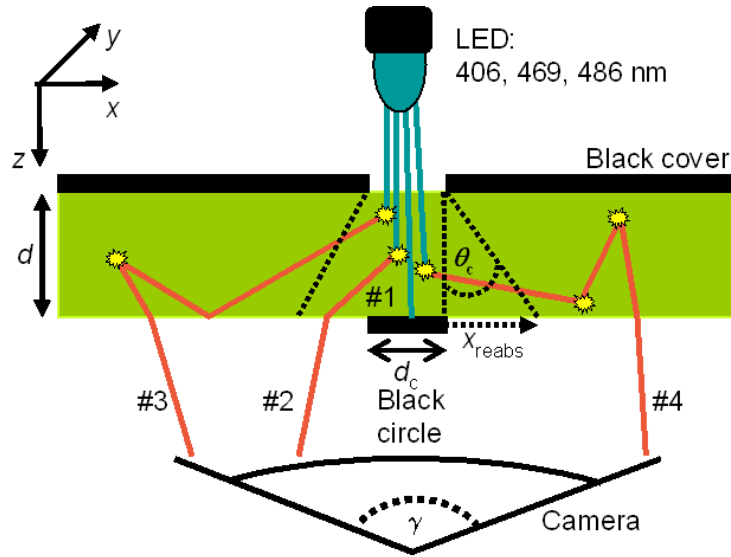


Fig. 4.2: Principle of reabsorption measurement. Light of an LED is canalized onto the collector surface. Photon ray #1 transmitted by the fluorescent collector hits a black absorbing circle. The dye absorbs photon ray #2 once and emits it with an angle smaller than the angle of total internal reflection. Ray #2 leaves the collector back side at $x < x_{\text{reabs}}$. In contrast, photon ray #3 is reabsorbed once and then emitted with a small angle. Thus, it leaves the collector back side outside x_{reabs} . Also, photon rays like ray #4 reabsorbed twice or more leave the collector back surface. A camera with lens aperture γ detects outgoing photons absorbed at least once.

The digital camera provides an image which is turned into grey-scale as exemplary shown in Fig. 4.3. Along the white arrow in x -direction, a line-scan of the intensity is extracted and used for fitting the reabsorption coefficient α_{reabs} .

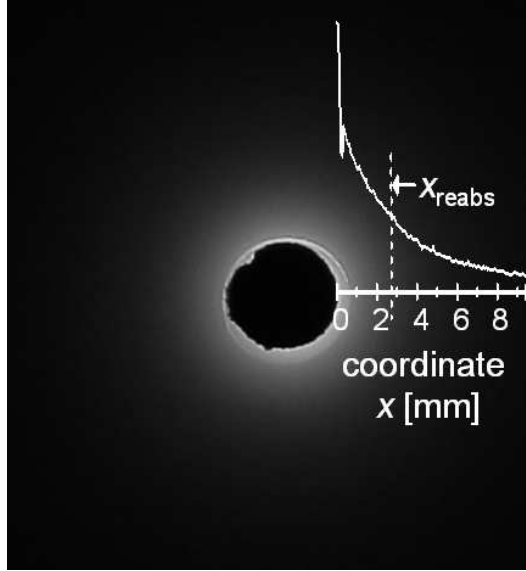


Fig. 4.3: Grey-scale of camera image taken with set-up shown in Fig. 4.2. Line-scan for fitting the reabsorption coefficient is extracted along white arrow in x -direction.

Figure 4.4 shows line-scans from three images taken with 406 nm, 469 nm and 486 nm incident wavelength. The camera aperture F and exposure time t was $F = 2.8$ and $t = 6$ s for 406 nm and 469 nm as well as $F = 3.2$ and $t = 2$ s for 486 nm.

4.1.2 Comparison to Monte-Carlo simulation

Aside from the line-scans taken from the grey-scale images, Fig. 4.4 also contains line-scans simulated with the Monte-Carlo model described in Sect. 3.1. For the FC, I assume an idealized absorption and emission behavior as in Fig. 3.2 with the values $E_1 = 2.62$ eV, $E_2 = 2.52$ eV, $\alpha_1 = 3$ mm⁻¹ and $\alpha_2 = 0.021$ mm⁻¹. These values display the green FC depicted in Fig. 2.2d. The absorption coefficient α_2 stands for the reabsorption coefficient α_{reabs} which will be determined in Sect. 4.1.3. Modeling the system in this idealized fashion provides line-scans similar to the measured ones. Note, that the intensity of the Monte-Carlo line-scan is zero at $x = 0$ mm whereas the experimental line-scan has a high value. This is due to the assumption that in the simulation, all photons are emitted at $x = 0$ mm, whereas in the experiment the LED photons impinge on a wider range of x on the collector surface. With the black mask sketched in Fig. 4.2, I ensure that for the experimental line-scan,

intensities at $x_{\text{reabs}} \geq 2.7$ mm stem only from photons which are subject to at least one reabsorption process as explained above. Therefore, the experimental and the Monte-Carlo line-scan in Fig. 4.4 are comparable. The reabsorption coefficient is then extracted from the data 2.7 mm away from $x = 0$ (i.e. $x \geq x_{\text{reabs}} = 2.7$ mm).

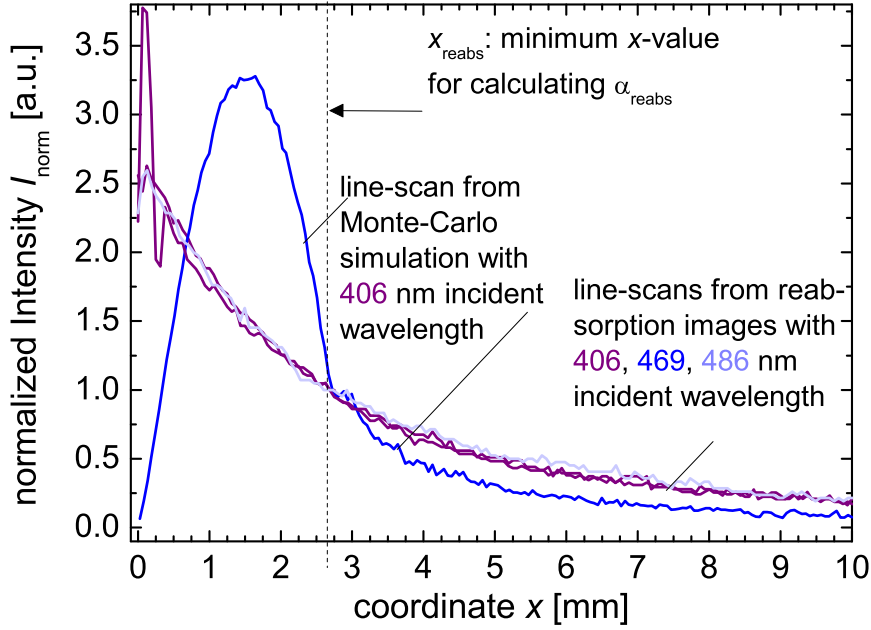


Fig. 4.4: Simulated and measured line-scans of the reabsorption experiment. For $x \geq x_{\text{reabs}} = 2.7$ mm photons leaving the collector are subject to at least one reabsorption event. The decline of the idealized modeled curve changes, whereas the trend of the measured data remains unchanged due to superposition with impinging and diffuse photons.

The Monte-Carlo line-scan shows a discontinuity in the intensity curve at x_{reabs} , whereas the descent of the experimental data remains constant. I explain this difference with the following idealized factors in the model. The modeled surrounding is completely dark, whereas in the experiment the concentrator also collects diffuse rays. In the simulation, the photons impinge perpendicular and punctual onto the collector top surface and therefore enter the collector with $\theta = 0^\circ$. In reality, the LED distributes its photons with different angles as implied in Fig. 4.2. In the simulation, all photons with adequate angle leave the collector, whereas in the

examined collector the photons experience other loss mechanisms like heat loss or stains and scratches on the surface. The camera in the experimental set-up collects rays with steep angles, whereas the Monte-Carlo simulation counts all outgoing rays independent from their angle.

For the simulated line-scan a local maximum occurs at $x = 1.5$ mm. This maximum occurs because the emission in the dye is pronounced towards the collector edges (for further explanation see App. B). Thus, after the first absorption less photons are directed towards the collector back side. The experimental line-scan inserted in Fig. 4.3 also shows a local maximum at $x \approx 0.34$ mm. The simulated and the experimental data differ for two reasons. First, as mentioned above, the LED in the experiment directs photons with a wide range of angles onto the surface, whereas the simulation assumes only perpendicular incident photons. Thus, in the experiment the first absorption occurs at several coordinates x in contrast to the simulation and possible line-scan maxima overlap. Second, the experimentally detected maximum occurs in my opinion as a reflection artifact since a halo appears around the black circle.

All intensity data I in Fig. 4.4 is normalized to $I(x_{\text{reabs}})$. As shown in Fig. 4.1, the absorbance $A \approx 80\%$ is similar for 406 nm, 469 nm and 486 nm incident wavelength. Although 469 nm and 486 nm lie in the reabsorption range, the line-scans achieved at these incident wavelengths equal the line-scan from 406 nm. This correspondence indicates that the collector emits into a certain wavelength range independent from the incident wavelength (explained for example in [23]). Thus, the absolute value of the intensity of the photons leaving the collector back side changes with the incident wavelength, the camera aperture and the exposure time but not the descent of the intensity. Since the collector emits always in the same wavelength range, I use *one* reabsorption coefficient for all wavelength as elaborated in the next section.

4.1.3 Analytical fit

The analytical fit is based on the idea sketched in Fig. 4.5. Here, exemplary a ray of photons with intensity I_0 is followed through the system. The ray enters the system at $(0, 0, 0)$. After entering the system with absorption coefficient α , it is absorbed and -neglecting non-radiative losses- emitted with the intensity

$$I_1^{\text{abs}}(z) = I_0 e^{-\alpha z}. \quad (4.2)$$

Theoretically, more than one reabsorption event with subsequent emission at the collector back side is possible as sketched for I_3^{abs} and I_3^{out} in Fig. 4.5. But, I neglect further reabsorption events for two reasons. First, the intensity I_{out}^n with $n > 2$ is significantly lower than for $n \leq 2$. Second, the reabsorption coefficient α_{reabs} includes all wavelengths emitted by the dye. Therefore, it describes every ray absorption after the first one. Assuming a higher number of reabsorption events leads then to lower α_{reabs} . For every determined α_{reabs} it is therefore necessary to specify the considered order of reabsorption events. In the next Sect. 4.2, the reabsorption coefficient derived with the analytical fit from this section predicts experimental results using an analytical description which is based on the same number of reabsorption events.

As seen from Eq. 4.4, the intensity I_2^{out} of photons leaving the collector back side depends on the intensity I_2^{abs} . The line-scan from the grey-scale image in Fig. 4.3 stems from a superposition of outgoing photons emitted in a distance lower than 2.7 mm around the line of extraction. Within this distance all photons emitted by the dye reach the back side with $\theta_c \geq \theta \geq 0^\circ$ (see Eq. 4.1) and therefore leave the collector. In order to fit the reabsorption coefficient α_{reabs} , I derive the line-scan in two steps: First, I calculate a map of the intensity $I_2^{\text{abs}}(x, y)$ after the first absorption for the coordinates (x, y) . Second, I derive the output intensity I_2^{out} after the first reabsorption. Here, I_2^{out} describes the intensity that reaches the line of extraction from each coordinate (x, y) .

Intensity $I_2^{\text{abs}}(x, y)$ map after first absorption

For the first step, I use Eq. 4.3 and calculate the intensity I_2^{abs} which reaches the coordinates (x, y, d) when the photon ray starts with an intensity I_1^{abs} at $(0, 0, d/2)$ ($d = 3$ mm is the collector thickness). The line-scan extracted from the grey-scale image (Fig. 4.3) lies in the interval $0 \text{ mm} < x < 10 \text{ mm}$. As explained above, the photons reaching the line of extraction are emitted within a distance of 2.7 mm. Thus, I choose the limits $x_{\text{min}} = -2.7 \text{ mm}$ and $x_{\text{max}} = 12.7 \text{ mm}$ for the intensity map of I_2^{abs} . The line-scan is assumed to be at $y = 0 \text{ mm}$. Then, the intensity map limits are $y_{\text{min}} = -2.7 \text{ mm}$ and $y_{\text{max}} = 2.7 \text{ mm}$. Rays starting from $(0, 0, d/2)$ and reaching each point (x, y, d) with $-2.7 \text{ mm} < x < 12.7 \text{ mm}$ and $-2.7 \text{ mm} < y < 2.7 \text{ mm}$ occupy the spherical angles (θ, ϕ) . Exemplary, Figs. 4.6a,b depict (θ, ϕ) for rays reaching $(x_{\text{min}}, y_{\text{min}})$ and $(x_{\text{max}}, y_{\text{min}})$. The reabsorption of photons in the dye takes place along the ray radius R as indicated by the dashed arrow in Fig. 4.6b.

Figure 4.6c shows how I regard multiple total internal reflections by assuming a fluorescent collector with thickness $d^* = iid - d/2$ ($ii = 1, 2, 3, \dots$). For example, ray #1a is totally internally reflected once at the collector back side before it reaches the point $(x_{\min}, y_{\min}, 0)$. In order to describe the behavior of ray #1a, I use the properties of ray #1 instead. Note, that ray #1 also depicts the behavior of a mirrored ray #1a which is totally internally reflected at the top surface and then reaches (x_{\min}, y_{\min}, d) as exemplary shown for rays #2 and #2a. The dashed grey arrow indicates that the radius $R(x, y, ii)$ depends on the assumed collector thickness $d^*(ii)$, i.e., the number of total internal reflections.

Although, the absorption occurs along R , the line-scan extracted from the grey-scale image represents the intensity decrease in x -direction. Therefore, the radius

$$R(ii) = \begin{cases} \frac{x}{\sin \theta(ii) \cos \phi} & \text{for } x \neq 0 \\ \frac{y}{\sin \theta(ii) \sin \phi} & \text{for } x = 0 \end{cases} \quad (4.5)$$

is described with the cartesian coordinates x and y as well as the spherical coordinates

$$\phi == \begin{cases} \arctan(x/y) + \pi & \text{for } x < 0 \\ \arctan(x/y) & \text{for } x > 0 \\ \pi/2 & \text{for } x = 0 \text{ and } y > 0 \\ -\pi/2 & \text{for } x = 0 \text{ and } y < 0 \end{cases} \quad (4.6)$$

and

$$\theta(ii) = \arctan \frac{\sqrt{x^2 + y^2}}{z(ii)} \quad (4.7)$$

as sketched in Figs. 4.6a,b (see [56], p. 198, 217). The coordinate

$$z(ii) = iid - d/2 \quad (4.8)$$

describes the collector thickness the photon ray sees experiencing ii events of total internal reflection. Note, that with Eq. 4.8, I approximate the analytical description in two ways: All photons are emitted at $d/2$ and the photons reaching a point (x, y) occupy either $z = 0$ for $ii = 2, 4, \dots$ or $z = d$ for $ii = 1, 3, \dots$

I calculate $I_2^{\text{abs}}(x, y, \theta(ii))$ for $\theta(x, y, z(ii)) \geq \theta_c$ because in this first step I describe the intensity reaching a point (x, y) due to total internal reflection. Thus, I increase ii as long as there are points (x, y) reached with $\theta(x, y, z(ii)) \geq \theta_c$. Exemplary in Fig. 4.6c, ray #4 reaches (x_{\max}, y_{\min}) with an angle $\theta = \theta_c$ after seven events of total

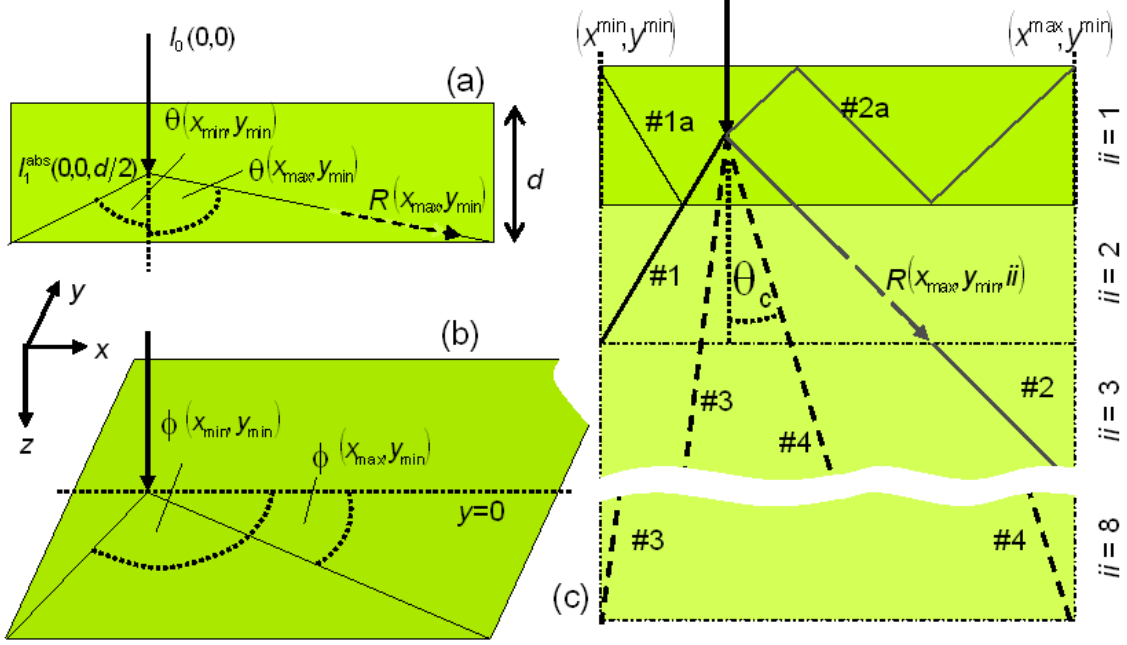


Fig. 4.6: Principle sketch for the derivation of an intensity I_2^{abs} map after the first absorption. a) Photons enter the system at $(0,0)$. The fluorescent dye absorbs and emits photons spatially randomized at $(0,0,d/2)$. Photon rays reaching the coordinates (x,y) occupy the spherical angle θ . b) In the $x-y$ -plane, the rays have the spherical angle ϕ . c) Multiple total internal reflection process are regarded by virtually increasing the collector thickness. For example, for the description of ray #1a which is totally internally reflected once at the back side, I use the properties of ray #1. As shown for ray #2a, rays #1 and #2 not only describe rays emitted with $\theta < 90^\circ$ but also rays with $\theta > 90^\circ$. Latter experience the same number of total internal reflections but hit the top surface first. According to Eq.4.3, the emitted intensity $I_2^{\text{abs}}(x,y,ii)$ is calculated for each collector thickness $d^* = iid - d/2$ for each point (x,y) .

internal reflection ($ii = 8$). In contrast, ray #3 would reach (x_{\min}, y_{\min}) with $\theta < \theta_c$. Therefore, ray #3 is not totally internally reflected and neglected in the calculation.

The coordinate (x,y) is reached by the photon intensity

$$I_{2,\text{tot}}^{\text{abs}}(x,y) = \sum_{\theta(ii)=\theta_c}^{90^\circ} 2I_2^{\text{abs}}(x,y,\theta(ii)). \quad (4.9)$$

The factor 2 regards the fact the description with the virtually increased system in Fig.4.6c also holds for photon rays emitted with $\theta > 90^\circ$. Then, the first event of total internal reflection takes place at the top surface as exemplarily explained above

for rays #1 and #1a as well as #2 and #2a.

Output intensity after first reabsorption

Figure 4.7 indicates the derivation of the intensity $I_{2,\text{tot}}^{\text{out}}$ on the black line at $y = 0$. The result corresponds to the line-scan extracted from the experimental grey-scale image (Fig. 4.3) and serves as the fitting function with the fitting parameter α_{reabs} .

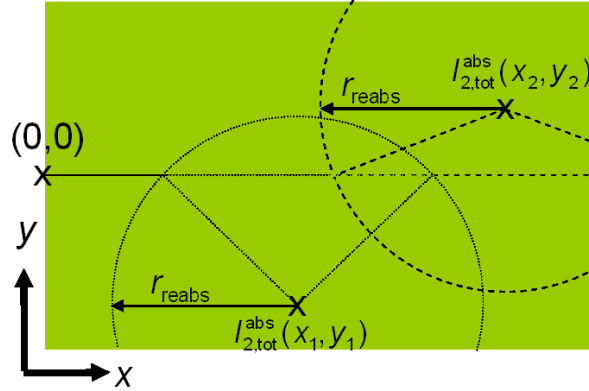


Fig. 4.7: Sketch for the derivation of the photon intensity leaving the collector back side at the black line at $y = 0$ which corresponds to the line-scan extracted from the experimental grey-scale image from Fig. 4.3. For each point (x_j, y_k) , Eq. 4.10 calculates the intensity leaving at the black line. In this example, the intensities of (x_1, y_1) and (x_2, y_2) overlap. In order to derive the total outgoing intensity $I_{2,\text{tot}}^{\text{out}}$, Eq. 4.11 summarizes the intensities which reach the black line at $y = 0$ mm from all points (x_j, y_k) .

Taking the map of $I_{2,\text{tot}}^{\text{abs}}(x_j, y_k)$ from Fig. 4.6b, I calculate for every point (x_j, y_k) with Eq. 4.4 the intensity that leaves the collector back side at the black line

$$I_2^{\text{out}}(x', y') = \frac{1}{R(x', y')^2} \sin(\theta(x', y')) I_2^{\text{abs}}(x_j, y_k) e^{-\alpha_{\text{reabs}} R(x', y')} \quad (4.10)$$

with $R = \sqrt{x'^2 + y'^2 + z'^2}$. Here, $x' = x - x_j$ and $y' = 0 - y_k$ are the coordinates, the black line occupies relatively to the treated point (x_j, y_k) . I approximate that all photons are emitted at $z_j = d/2$ after the first reabsorption. Calculating the photon intensities at the collector back side leads to $z' = d - z_j = d/2$. Note, that Eq. 4.10 regards the change in the coordinate system unlike Eq. 4.4.

In contrast to I_2^{abs} in the first calculation step, the calculation of I_2^{out} considers only photons emitted with an angle lower than the angle of total internal reflection. These are photons which leave the collector within a radius r_{reabs} as exemplary

sketched for two points (x_1, y_1) and (x_2, y_2) in Fig. 4.7. According to Eq. 4.1, $z' = d/2$ leads to $r_{\text{reabs}} = 1.4$ mm. As sketched in Fig. 4.7, the intensities $I_2^{\text{out}}(x', y')$ calculated from each point (x_j, y_k) overlap. In order to derive the whole line-scan, I calculate

$$I_{2,\text{tot}}^{\text{out}}(x, y) = \sum_{j=1}^n \sum_{k=1}^m I_2^{\text{out}}(x - x_j, 0 - y_k). \quad (4.11)$$

Here, n and m depend on the number of points I choose to calculate for the derivation of $I_{2,\text{tot}}^{\text{out}}$.

Result

Figure 4.8 presents the results for the fitting process. The grey line is the measured line-scan from the grey-scale image taken with 406 nm incident wavelength (also pictured in Fig. 4.4). The black dotted line represents the results of the fitting process which derives a reabsorption coefficient $\alpha_{\text{reabs}} = 0.021 \text{ mm}^{-1}$. The analytically derived outgoing intensity is in very good agreement with the measured results.

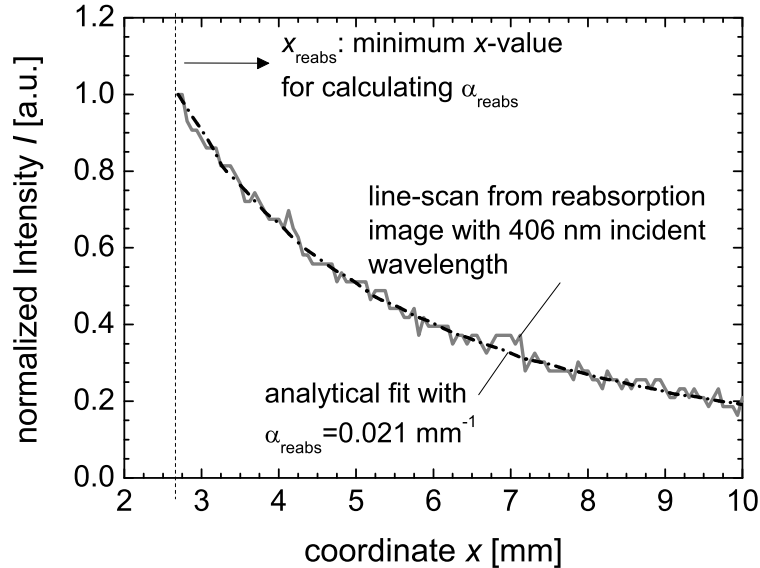


Fig. 4.8: Results of the fitting process. The grey line is the experimental result as also presented in Fig. 4.4. The black dotted line is achieved with the fitted reabsorption coefficient $\alpha_{\text{reabs}} = 0.021 \text{ mm}^{-1}$.

4.1.4 Conclusion and Outlook

This section presents a simple and quick measurement of the reabsorption in a fluorescent collector. The analytical description of the reabsorption processes in a fluorescent collector developed in this section fits the measurement results perfectly. The reabsorption for the fluorescent collector analyzed in this section is determined to be $\alpha_{\text{reabs}} = 0.021 \text{ mm}^{-1}$. In the next section, I use the results of this section to predict the results of a light beam induced current (LBIC) experiment. LBIC-measurements not only need more material (light source, solar cell, translation stage, Lock-In amplifier, etc.) but also take long times. Predicting the LBIC-results with a fast reabsorption measurement, is a time- and cost-saving improvement.

However, the reabsorption coefficient α_{reabs} derived in this section holds for the analyzed fluorescent collector (Fig. 4.1) only. A different collector thickness as well as different absorption and emission behavior of the dye leads to different α_{reabs} .

4.2 Current increase of a-Si cell under fluorescent collector

The first part of this section presents a set-up with a fluorescent collector on top of an amorphous silicon (a-Si) solar cell which achieves 7% more current than the solar cell alone. With a photonic band stop (PBS) filter on top, the current increases even by 95% [17]. In the second part, I explain the connection between reabsorption and light beam induced current (LBIC) measurements and describe the experiment with the reabsorption coefficient $\alpha_{\text{reabs}} = 0.021 \text{ mm}^{-1}$ derived in the former section.

4.2.1 Measuring concentration in fluorescent collectors

Figures 4.9a-c present the three experimental set-ups. For all measurements, I use the same amorphous silicon (a-Si) solar cell of size $14 \times 14 \text{ mm}^2$ which is attached to a glass superstrate. The solar cell was manufactured by Florian Einsele. It consists of a positively (p) and a negatively (n) doped layer with an intrinsic (i) layer in between. The p- and n-layer are 20 to 50 nm thick while the absorbing i-layer has a thickness of $1 \mu\text{m}$. In order to measure the light beam induced current (LBIC), a laser beam with 3.01 eV falls perpendicular and punctual onto the top surface of each experimental set-up. Photons which reach the solar cell from the incident spot induce a short circuit current I_{SC} which is measured with a Lock-In amplifier. The solar cell lies on a translation stage which positions the solar cell towards the light beam. I perform LBIC measurements every 0.2 mm on an area of $45 \times 45 \text{ mm}^2$ with the solar cell in the center. For the first measurement depicted in Fig. 4.9a, the solar cell is attached to the glass superstrate. Rays hitting the surrounding glass are transmitted. Only photons incident on solar cell area induce current. Figure 4.9b sketches the second measurement: A fluorescent collector (FC) lies on top of the a-Si cell. This is the same collector (Acid Green, 6T66 by PerspexTM [22]) as in the reabsorption measurement. The area surrounding the solar cell is covered with white paint (Acrylic Spray Paint No. 7100.200 by RICO DESIGN) which acts almost like a Lambertian reflector. The FC is optically coupled with Glycerin directly above the solar cell. The photovoltaic active area increases, because part of the rays emitted by the dye with spatially randomized direction is guided to the solar cell via total internal reflection. Figure 4.9c presents the third measurement: A PBS filter covers the system with FC as in the second measurement. The application of a PBS filter traps rays usually leaving the collector because they have a lower angle than the

angle of total internal reflection.

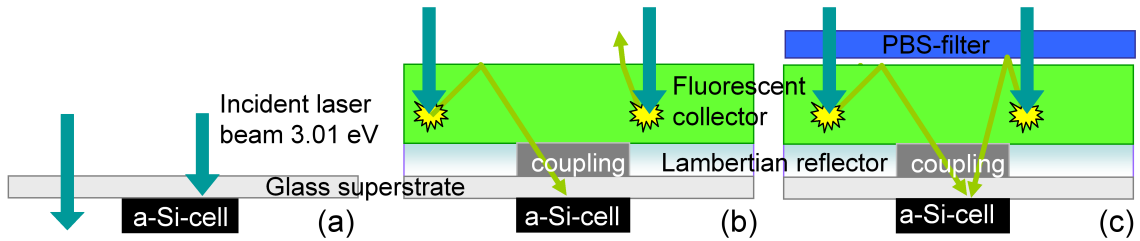


Fig. 4.9: Set-ups for LBIC measurements. a) Solar cell under glass superstrate. Rays hitting the surrounding glass are transmitted. Photons incident on solar cell area induce current. b) Fluorescent collector (FC) on top of a-Si cell. The photovoltaic active area increases, because the dye emits spatially randomized photons. c) A PBS filter traps rays usually leaving the collector with a lower angle than the angle of total internal reflection.

Figures 4.10a,b characterize the components for the experiment. Figure 4.10a

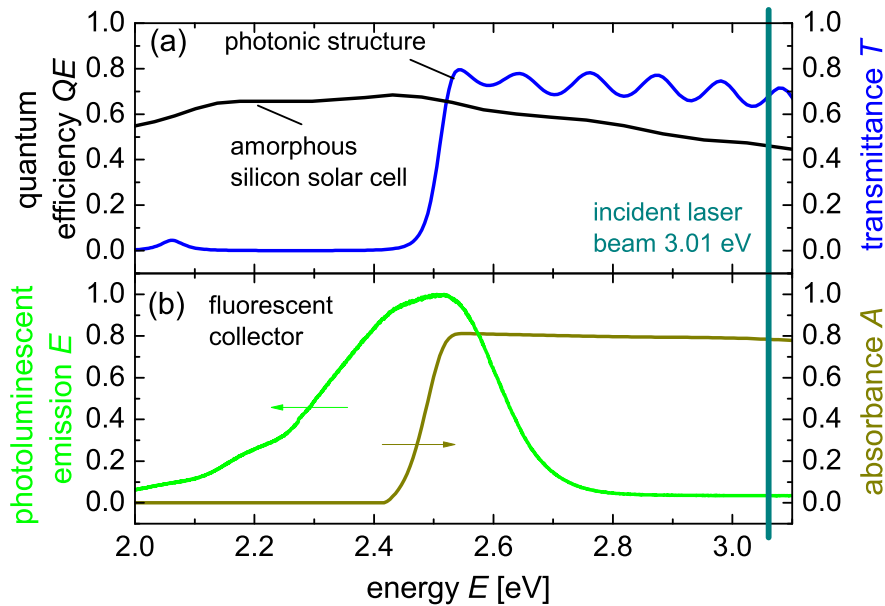


Fig. 4.10: a) Quantum efficiency QE of amorphous silicon (a-Si) solar cell and transmittance T_D of photonic band stop (PBS) filter. b) The fluorescent collector absorbs and emits photons such that the QE of the a-Si cell is more suitable for the emitted photons. The photonic structure reflects most of the emitted photons and transmits 68% of the incoming photons with energy 3.06 eV.

presents the quantum efficiency QE of the a-Si cell. As seen in Fig. 4.10b, the FC absorbs photons with energy above 2.4 eV, while its emission range lies between 2.2 eV and 2.7 eV. Thus, the FC absorbs photons for which the quantum efficiency $QE < 60\%$ of the solar cell is below $QE \approx 65\%$ for the emitted photons. Figure 4.10a also shows that the PBS filter transmits photons with energy above 2.5 eV. Therefore, the PBS reflects the emitted photons from the FC but transmits 68% of the incoming photons with 3.01 eV.

Solar cell

Figure 4.11 presents the LBIC results for the solar cell alone. The solar cell is applied to a glass superstrate. The surrounding glass reflects and absorbs incident light as shown in Fig. 4.9a but is not photovoltaic active. The current generating area is limited to the solar cell with area 1.96 cm^2 in the center of the measured area. The maximum current on the solar cell is $10.9 \mu\text{A}$. The over-all collected current $I_{\text{coll}} = 8.5 \text{ mA}$ is calculated by summarizing all measured current values.

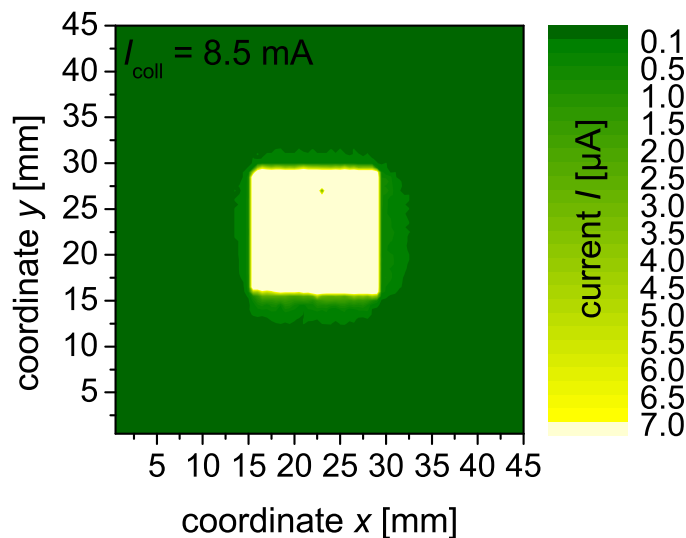


Fig. 4.11: LBIC measurement results for the solar cell directly exposed to the light beam. The system collects an over-all current $I_{\text{coll}} = 8.5 \text{ mA}$.

Solar cell under fluorescent collector

Figure 4.12 shows the results for the LBIC measurement of the FC on top of the solar cell as sketched in Fig. 4.9b. In contrast to Fig. 4.9a, rays hitting the surrounding area of the solar cell also induce current. The emission of photons in the FC occurs spatially randomized, enhancing the photovoltaic active area to $\approx 20.25 \text{ cm}^2$. Total internal reflection guides the photons to the collector sides. The FC is optically coupled to the solar cell which disables the total internal reflection. Here, the back side of the FC transmits the photons which then induce current in the solar cell. Unfortunately, a certain part of the emitted light leaves the collector because its emission angle lies below the angle for total internal reflection. As a result, the current induced directly above the solar cell decreases to $6.2 \mu\text{A}$. The larger photovoltaic active area compensates this loss and the over-all collected current $I_{\text{coll}} = 9.1 \text{ mA}$ is 7% higher compared to the solar cell alone.

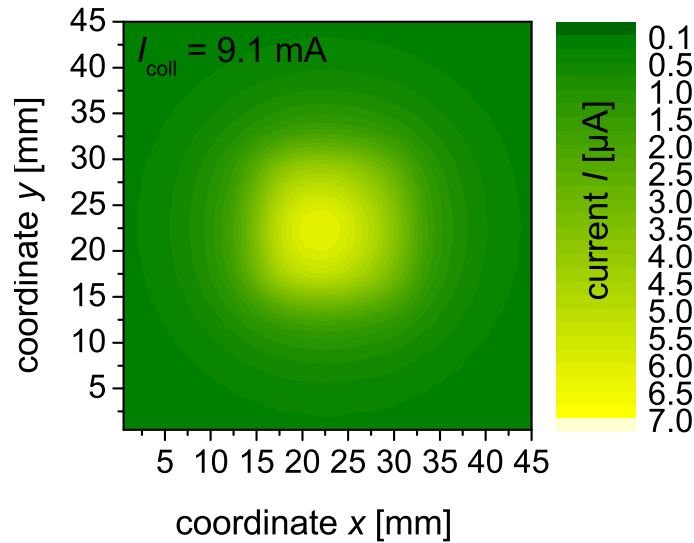


Fig. 4.12: LBIC measurement results for the fluorescent collector (FC) on top of the solar cell. Directly above the solar cell the current decreases by 43% compared to the solar cell alone. The photovoltaic active area increases and therefore the over-all collected current rises from 8.5 mA to 9.1 mA.

Solar cell under fluorescent collector and photonic structure

Figure 4.13 depicts the results for the photovoltaic system with the a-Si cell below the FC and the PBS filter on top. The pattern appears due to the interferential

behavior of the filter. All current values increase compared to the system described in Fig. 4.9b. The maximum current above the solar cell rises, too. As sketched in Fig. 4.9c the filter also traps photons which leave the system in Fig. 4.9b because their angle is below the angle of total internal reflection. Still, the values above the solar cell are lower than for the solar cell directly exposed to the light beam. As seen in Fig. 4.10a the values decrease, because the filter reflects 68% of the incoming laser beam (3.01 eV) normally inducing current on the solar cell. Also, the FC emits photons spatially randomized and some photons are guided to the collector sides without reaching the solar cell. However, since the PBS reflects most of the emitted photons regardless of their angle, the current induced above the solar cell increases compared to the FC alone. The losses directly above the solar cell are effectually compensated by the gain from the surrounding area. Therefore, the over-all collected current $I_{\text{coll}} = 16.6 \text{ mA}$ outreaches I_{coll} of the solar cell alone by 95%.

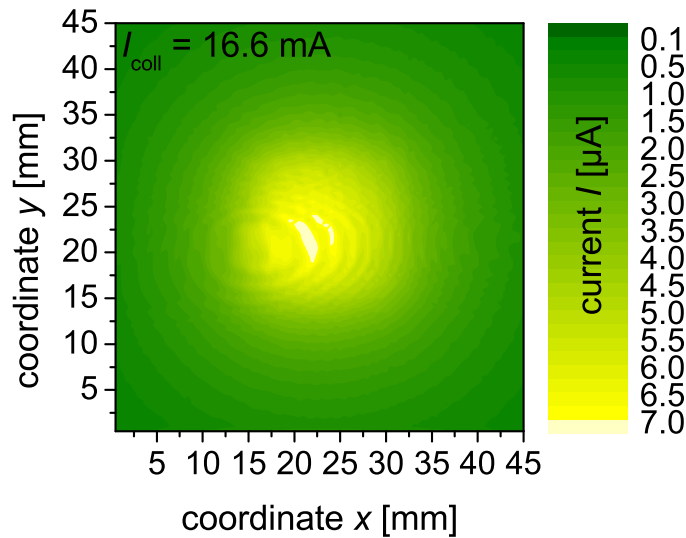


Fig. 4.13: LBIC measurement for the photonic band stop (PBS) on top of the FC and the solar cell. All measured values increase compared to the system without PBS. While the maximum current of $7.45 \mu\text{A}$ directly above the solar cell is significantly lower than in Fig. 4.11a, the over-all collected current I_{coll} increases by 95%.

4.2.2 Comparison to Monte-Carlo simulation

Figure 4.14a compares line-scans taken at $y = 22.5$ mm of the three performed LBIC measurements. Note, that $y = 22.5$ cm lies slightly off-center. Obviously, for the solar cell alone the photovoltaic active area is restricted to the solar cell area. The FC increases the photon collecting area. While the current induced above the solar cell significantly decreases, the larger area compensates this loss as discussed above. Compared to the FC alone, the application of the PBS filter not only increases the current collected above the solar cell but also the photovoltaic active area. At the edges of the measured area, the current collected is still above zero. Thus, even points further away from the solar cell than measured contribute to the current. Figure 4.14b presents the results for the Monte-Carlo ray-tracing simulations of the line-scans.

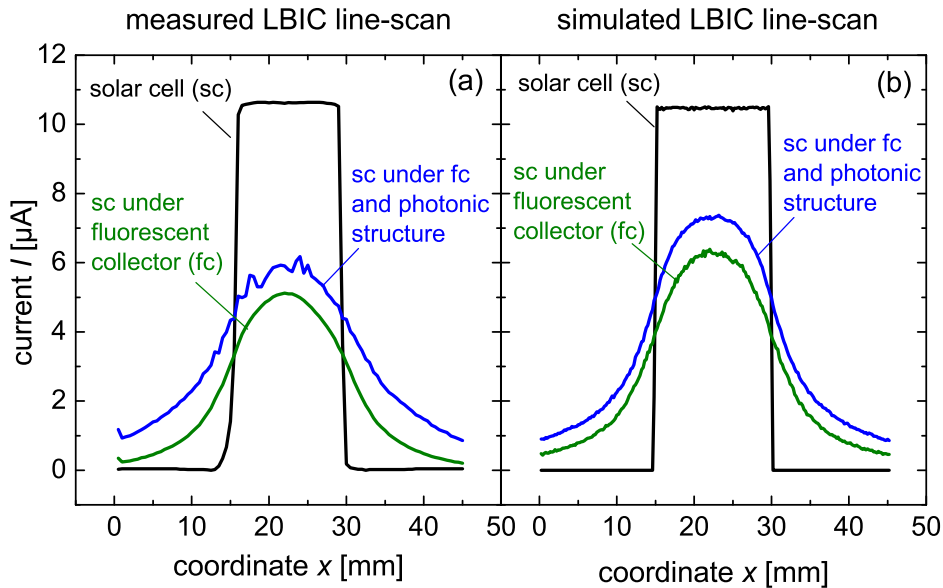


Fig. 4.14: a) Comparison of LBIC line-scans extracted at $y = 25$ mm. Above the solar cell the application of the FC as well as the PBS decreases the current significantly. However, both components enlarge the photovoltaic active area by collecting photons also from the surrounding area. At the edges of the measured area, the current in the system with PBS is not zero which leads to assuming an even larger photovoltaic active area. b) Monte-Carlo ray-tracing simulation results for realistic components as shown in Fig. 4.10. The lambertian reflector and the optical coupling are assumed to be ideal which results in better values for the current than in the measurement.

The Monte-Carlo ray-tracing simulation described in Sect. 3.1 calculates the current for realistic components. The simulation fits the measurement but shows slightly better values which result from the assumption of a perfect Lambertian reflector and an ideal optical coupling above the solar cell. A main factor for the success of this photovoltaic system is the scaling. The enlargement of the photovoltaic active area has an absolute value depending on the emission and absorption behavior of the FC, the transmission and reflection at the PBS and the back and front side quality of the FC. The larger the solar cell area the less compensative the enlargement of the current collecting area.

4.2.3 Link to Reabsorption

The line-scan for the fluorescent collector from Fig. 4.14a differs from the line-scan of the reabsorption experiment in the previous chapter 4.1. In the reabsorption measurement, the line-scan represents the intensity at each point $(x, 0, d)$ stemming from photons incident at $(0, 0, 0)$. The line-scan extracted from the LBIC-experiment represents how many photons from the photon ray incident at each point $(x, 0, 0)$ reaches the solar cell at (x_{sc}, y_{sc}, d) .

Figures 4.15a-c indicate the derivation of the analytical expression which describes the line-scan of the LBIC-experiment. Figure 4.15a sketches that a photon ray incident at $(x, y, 0)$ is absorbed and emitted at $(x, y, d/2)$ with intensity $I_1^{\text{abs}} = I_0 \exp^{-\alpha d/2}$ (compare Eq. 4.2). Part of the ray reaches the solar cell which lies at the coordinates $x_{sc}^{\text{min}} \leq x_{sc} \leq x_{sc}^{\text{max}}$ and $y_{sc}^{\text{min}} \leq y_{sc} \leq y_{sc}^{\text{max}}$. In order to reproduce the experimental line-scan, I choose $x_{sc}^{\text{min}} = 15$ mm, $x_{sc}^{\text{max}} = 29$ mm. Since the extracted line-scan lies at $y = 22.5$ mm, I choose this as the reference line and therefore $y_{sc}^{\text{min}} = -7.5$ mm and $y_{sc}^{\text{max}} = 6.5$ mm. For each point $(x' = x - x_{sc}, y' = y - y_{sc})$, the spherical angles

$$\theta(ii) = \arctan \frac{\sqrt{x'^2 + y'^2}}{z(ii)} \quad (4.12)$$

and

$$\phi = \begin{cases} \arctan(x'/y') + \pi & \text{for } x' < 0 \\ \arctan(x'/y') & \text{for } x' > 0 \\ \pi/2 & \text{for } x' = 0 \text{ and } y' > 0 \\ -\pi/2 & \text{for } x' = 0 \text{ and } y' < 0 \end{cases} \quad (4.13)$$

are calculated as exemplary shown for $(x_{sc}^{\text{min}}, y_{sc}^{\text{max}})$ and $(x_{sc}^{\text{max}}, y_{sc}^{\text{max}})$ in Figs. 4.15a,b. As in Sect. 4.1.3, I consider multiple events of total internal reflection by assuming

a larger collector thickness $d^* = iid - d/2$ (Fig. 4.15c). The spherical angle $\theta(ii)$ depends on

$$z(ii) = iid - d/2 \quad (4.14)$$

which describes the collector thickness the photon ray sees experiencing ii events of total internal reflection. Note, that with Eq. 4.14, I approximate that all photons are emitted at $d/2$.

In Fig. 4.15c photon ray 1 reaches the solar cell at the virtual thickness $d^*(ii)$ for $ii = 2$. This ray 1 is used to describe ray 1a which experiences one total internal reflection at the top surface. Seeing a collector thickness $d^*(ii = 3)$, ray 2 represents ray 2a which is totally internally reflected twice, first at the bottom surface and then at the top surface. Thus, photons traveling through collector thicknesses $d^*(ii)$ with $ii = 2, 4, \dots$ display photons with $\theta(ii) > 90^\circ$, whereas for $ii = 1, 3, \dots$, the photons occupy $\theta(ii) < 90^\circ$.

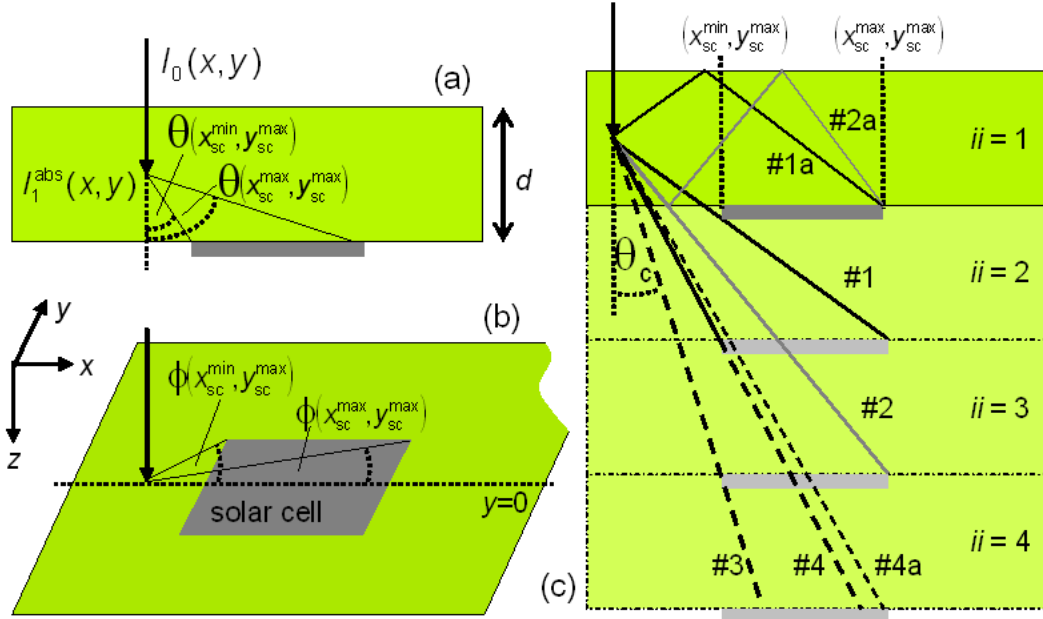


Fig. 4.15: Principle sketch for derivation of experimental line-scan in Fig. 4.14a. a) An incoming photon ray at $(x, y, 0)$ is absorbed and emitted at $(x, y, d/2)$ with intensity I_1^{abs} . The photon reaches the solar cells with spherical angles θ and b) ϕ . c) A virtually thicker collector regards multiple total internal reflections analog to the explanations for Fig. 4.6c.

Figure 4.15c points out two restrictions concerning the spherical angle $\theta(ii)$, exemplarily clarified at $ii = 4$ (dashed lines) for ray 3 and rays 4, 4a, respectively. First,

a shadowing effect occurs for photons emitted at certain angles. For example, if ray 4a reaches the solar cell point $(x_{sc}^{\max}, y_{sc}^{\max})$ after three events of total internal reflection, one of the events of total internal reflection occurs on solar cell area. Therefore, photons with angles that already reach the solar cell after one total internal reflection ($ii = 2$, black line) cannot be counted for $ii = 4$. Thus, ray 4 replaces ray 4a and the maximum angle $\theta(4)$ equals the minimum angle $\theta(ii = 2)$. Note, that photons reaching the solar cells after two events of total internal reflection ($ii = 3$, grey line) do not interfere with photons hitting the solar cell after one reflection ($ii = 2$), because they display rays emitted with angles $\theta > 90^\circ$. However, they do interfere with photons which directly reach the solar cell ($ii = 1$). The second restriction for $\theta(ii)$ lies in the principle of total internal reflection. Photons reaching $(x_{sc}^{\min}, y_{sc}^{\max})$ need an angle $\theta(ii) < \theta_c$ for $ii = 3$. Since the collector only guides photons with $\theta(ii) > \theta_c$, the solar cell area reachable for a photon emitted at (x, y) in this example is reduced. As an example, in Fig. 4.15c, ray 3 is the ray with the lowest angle $\theta(ii = 3) = \theta_c$ reaching the solar cell after three total internal reflections.

With Eqs. 4.12 to 4.14, I calculate the radius

$$R(ii) = \begin{cases} \frac{x'}{\sin \theta(ii) \cos \phi} & \text{for } x' \neq 0 \\ \frac{y'}{\sin \theta(ii) \sin \phi} & \text{for } x' = 0 \end{cases} \quad (4.15)$$

along which the intensity decreases. In order to derive the overall intensity reaching the solar cell from one point (x, y) , I use two steps.

First, I calculate the intensity for each thickness $d^*(ii)$

$$I^{\text{out}}(x, y, ii) = \sum_{x'=x-x_{sc}^{\min}}^{x-x_{sc}^{\max}} \sum_{y'=y-y_{sc}^{\min}}^{y-y_{sc}^{\max}} \frac{1}{R(x', y', ii)^2} \sin \theta(x', y', ii) I_1^{\text{abs}}(x, y) e^{(-\alpha_{\text{reabs}} R(x', y', ii))} L. \quad (4.16)$$

Here, the factor

$$L = \left[\frac{1}{2\pi} \int_{\phi_{\min}}^{\phi_{\max}} \int_{\theta_{\min}(ii)}^{\theta_{\max}(ii)} \cos \theta(ii) d\theta d\phi \right]^{[(ii-1)/2]} \quad (4.17)$$

regards the losses occurring during the reflection process at the Lambertian reflector covering the collector back side (for further explanation see [55], p. 372). For example, photons reaching the solar cell after two reabsorption events ($ii = 3$ in Fig. 4.15c) are reflected at the back side once. Thus, they experience an approximately Lambertian reflection once where the angles $\theta(3)$ needed for reaching the

solar cell are weighted with the factor L . For ii events of total internal reflection, the loss occurs $\lfloor (ii - 1)/2 \rfloor$ times.

In the second step, all intensities $I^{\text{out}}(x, y, ii)$ are summarized for evaluating the total intensity

$$I_{\text{out}}^{\text{tot}}(x, y) = \sum_{ii=1}^l I_{\text{out}}(x, y, ii). \quad (4.18)$$

The number l depends on the distance between the photon incidence and the solar cell.

Figure 4.16 depicts the experimental line-scan (grey line) and the line-scan calculated with the analytical solution derived in this section (dashed black line). In order to calculate the latter, I insert the reabsorption coefficient $\alpha_{\text{reabs}} = 0.021 \text{ mm}^{-1}$ fitted in the experiment in the former chapter in Sect. 4.1.3 into Eq. 4.16. Both line-scans are normalized to their particular maximum. The analytically derived line-scan matches the experimental line-scan very well. Together with the quick reabsorption measurement from Sect. 4.1, the mathematical description derived in this section provides a good tool to substitute the long-lasting and extensive LBIC-measurements.

The analytically derived line-scan predicts the relative intensity due to concentration. In order to analytically describe the measurement results in Fig. 4.11, I derive the $I_{\text{out}}^{\text{tot}}(x, y)$ map for an area of $45 \times 45 \text{ mm}^2$ with quadratic solar cell with edge length 14 mm in the center. The distance between the calculation points is 0.2 mm in x - and y -direction. Then, I normalize the $I_{\text{out}}^{\text{tot}}(x, y)$ map to its maximum $I_{\text{out}}^{\text{tot,max}}$ and multiply it with the maximum measurement value $I_{\text{max}}^{\text{fc}} = 6.2 \mu\text{A}$. The sum

$$I_{\text{coll}}^{\text{sim,fc}} = \frac{I_{\text{max}}^{\text{fc}}}{I_{\text{out}}^{\text{tot,max}}} \sum I_{\text{out}}^{\text{tot}}(x, y) = 9.9 \text{ mA} \quad (4.19)$$

corresponds to the experimentally gained $I_{\text{coll}}^{\text{exp,fc}} = 9.1 \text{ mA}$ (see Sect. 4.2.1). Assuming $I_{\text{max}}^{\text{sc}} = 10.9 \mu\text{A}$ on the cell area and no current gain on the surrounding area leads to $I_{\text{coll}}^{\text{sim,sc}} = 9.2 \text{ mA}$ as the calculation analogue to the LBIC-result $I_{\text{coll}}^{\text{exp,sc}} = 8.5 \text{ mA}$ from Sect. 4.2.1. Thus, the calculated results predict a current increase of 8% due to the application of the particular fluorescent collector analyzed in this section. This results agrees perfectly with the experimental result. Therefore, the fast reabsorption measurement from Sect. 4.1 together with its analytical description and the mathematical solution for the LBIC measurement are good substitute for the extensive LBIC measurements.

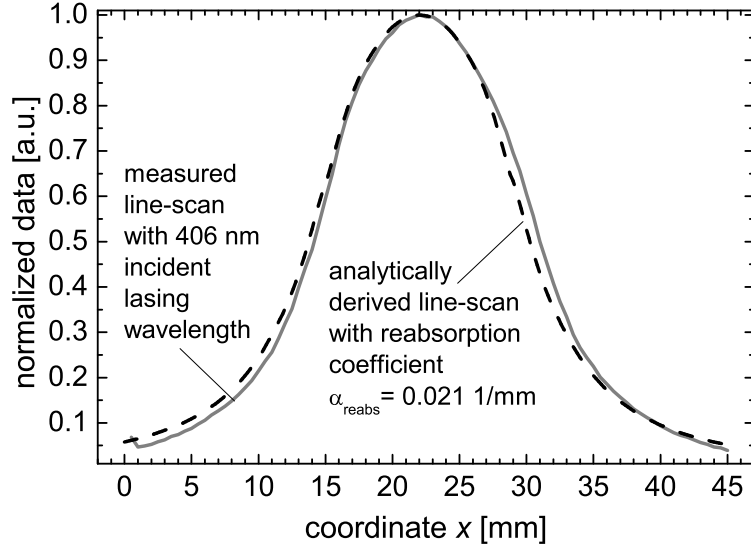


Fig. 4.16: Measured line-scan from the LBIC experiment with fluorescent collector and solar cell (Fig. 4.14a) and analytically derived line-scan (grey line and dashed line, respectively). Both data are normalized to their maximum. The line-scans agree very well with inserted reabsorption coefficient $\alpha_{\text{reabs}} = 0.021 \text{ mm}^{-1}$ which is extracted from the reabsorption measurement of the former chapter (Sect. 4.1.3).

4.2.4 Conclusion and Outlook

The results presented in the first part of this section leave space for improvement by better adjusting the components. First, the fluorescent collector should absorb with a narrower re-absorption range. Reabsorption takes place for photons emitted in the energy range of the FC absorption. Every absorption event randomizes the direction of the photons and leads to losses depending on the total internal reflection. Second, the filter could have a higher transmission at the incident photon energy. Every photon reflected at the filter is lost for the system.

The second part of this section proves that the quick and easy reabsorption measurement from Sect. 4.1 provides a good substitute for the long-lasting and material extensive LBIC experiments in this section. The analytical descriptions for both experiments and their connection due to the reabsorption coefficient predict the results for the LBIC experiments in very good agreement.

However, the mathematical model derived in this section does not describe the photovoltaic system with fluorescent collector and photonic band stop filter on top. I calculate the current $I_{\text{coll}}^{\text{sim,pbs}}$ collected by this system by multiplying the normalized $I_{\text{out}}^{\text{tot}}(x, y)$ map with the maximum collected current $I_{\text{max}}^{\text{pbs}} = 7.45 \mu A$. According to Eq. 4.19, the system with photonic filter then collects the calculated current $I_{\text{coll}}^{\text{sim,pbs}} = 11.9 \text{ mA}$ which is a lower value for the over all collected current than the experimental value $I_{\text{coll}}^{\text{exp,pbs}} = 16.6 \text{ mA}$. Therefore, the analytical description does not hold for a photovoltaic system with photonic band stop (PBS) filter. In order to substitute the LBIC measurement of the photovoltaic system with filter, an analytical description has to be developed. Also, the reabsorption measurement has to be executed with a fluorescent collector and a filter.

4.3 Geometrical and dispersive concentration

The previous sections examine the concentration in fluorescent collectors which occurs due to spatial distribution of the photons during the emission process in the dye and the total internal reflection of the acrylic glass plate. Classical photovoltaic concentration follows geometrical rules: a reflecting surface guides incident photons onto a solar cell.

This section presents an outdoor experiment which adds the dispersive concentration of fluorescent collectors to geometrical concentration of classical systems. Restricted to the trough aperture, the fluorescent collector leads to a decreased current gain. But, a current increase is realizable by simply increasing the collector area. In contrast, a current increase with geometrical concentration requires an additional concentration system with additional solar cell area. Another advantage of fluorescent collectors is their collection of incident photons independently from their incident angle. In contrast, geometrically concentrating systems need careful and material extensive tracking in order to reach highest output current.

4.3.1 Geometrically concentrating troughs under fluorescent collectors

For the purpose of comparing distributive concentration in fluorescent collectors and geometrical concentration as used in classical concentration systems, ERNST KIENZLE GMBH & CO KG customized 5 troughs out of acrylic glass blocks. Figures 4.17a and b sketch two trough geometries seen from the bottom. Figure 4.17a shows the trough with side surfaces beveled in one dimension. An angle $\beta = 56^\circ$ lies between the oblique opposite side surfaces and the ground. The other two opposite side surfaces (in the sketch the front and back surface) are perpendicular. Since in this direction the trough remains invariant, I call this trough two dimensional (2d-trough). The solar cell lies at the bottom of the trough. Figure 4.17b depicts the V-trough which also has two beveled ($\beta = 22^\circ$) and two perpendicular side surfaces but a bifacial solar cell standing in the middle. All troughs are of height $h = 2$ cm.

Figures 4.17c and d show photographs of the acrylic glass troughs. The solar cells applied to the troughs are cut out off two screen-printed industrial mono crystalline silicon (c-Si) solar cells with edge length 15.6 cm (manufactured at *ipe* and Q-CELLS). The trough cells consist of a photovoltaic active area $A_{\text{cell}} = 2 \times 2 \text{ cm}^2$

and the area of the busbar at one cell edge. The photovoltaic active area covers the bottom surface of the 2d-trough, while the busbar area overhangs the trough surface. Here, cell connectors manufactured by SOLSOL GMBH are soldered to the front and back side of the solar cell in order to contact the cell and measure the output current. In the V-trough, the bifacial solar cell is represented by two back-to-back trough cells covering two surfaces in the middle. Again, cell connectors are soldered to the overhanging busbar area.

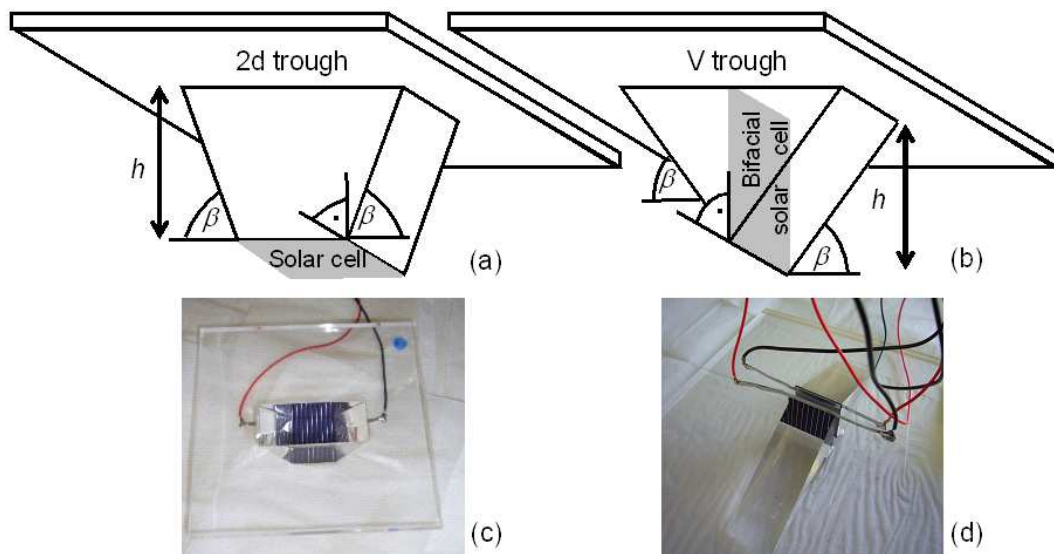


Fig. 4.17: a) Bottom view of 2d-trough: Two opposite side surfaces beveled, two perpendicular with solar cell at the bottom. b) Bottom view of V-trough: similar to 2d-trough but with bifacial solar cell in the middle. c) Photograph of 2d-trough from top. d) Photograph of V-trough from bottom: two back-to-back cells in the middle represent the bifacial solar cell.

Both trough geometries work with geometrical concentration. Figure 4.18a sketches that the beveled side surfaces guide impinging photons onto the solar cell due to total internal reflection. Photons hitting the side surfaces with incident angles below the angle for total internal reflection leave the trough. Photons impinging outside the trough aperture onto the acrylic glass plate are transmitted unless their angle is so oblique that they are totally internal reflected in the plate.

In Fig. 4.18b a fluorescent collector lies on top of the trough, optically coupled to the acrylic glass plate with Glycerin. A black mask around the trough aperture restricts the fluorescent material, in order to keep the photon collection area

comparable to the uncovered system in Fig. 4.18a.

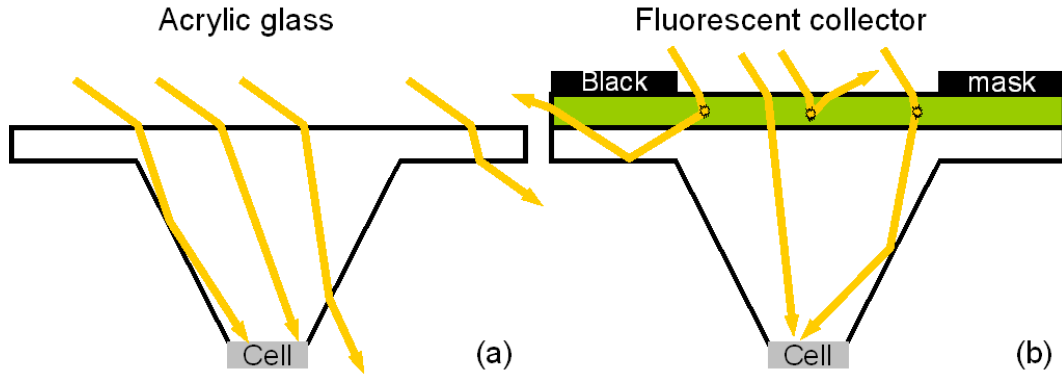


Fig. 4.18: a) In both systems from Figs. 4.17a-d the side surfaces guide incoming photons onto the solar cell due to total internal reflection. The concentration in these systems follows geometrical rules. b) A fluorescent collector on top absorbs photons and emits rays spatially randomized, thus adding a dispersive component to the geometrical concentration.

The fluorescent dye spatially randomizes photons and adds a dispersive component to the otherwise geometrically concentrating system. Figure 4.19 presents the absorbance A and emittance E of the fluorescent collector (Acid Green, 6T66 by Perspex™ [22]). The collector transmits all photons with wavelength $\lambda > 512$ nm. These transmitted photons then underlie the same conditions as the rays in Fig. 4.18a, i.e. they change their directions following geometrical rules. In contrast, absorbed photons change their direction, because the dye molecules emit them spatially randomized. Figure 4.18b indicates three possible pathways for the emitted photons. One part leaves the system through the top surface. Another part of the emitted photons is directed into the trough where they experience geometrical concentration. The third part is guided due to total internal reflection in the plate on top of the trough and leaves the system through the collector edges or is reabsorbed. Figure 4.19 shows another benefit of the fluorescent conversion: 80 % of photons with $\lambda < 512$ nm are absorbed by the dye. After the emission process, they reach the solar cell with $450 < \lambda < 650$ nm, a wavelength range where the solar cell achieves higher quantum efficiencies QE . Exemplary, Fig. 4.19 presents the QE -results of the cell in the 2d-trough with fluorescent collector on top. Figure C.1 in App. C presents that the other cells show similar quantum efficiencies.

Figure 4.20a depicts a third geometry (the 3d-trough) which has all four trough

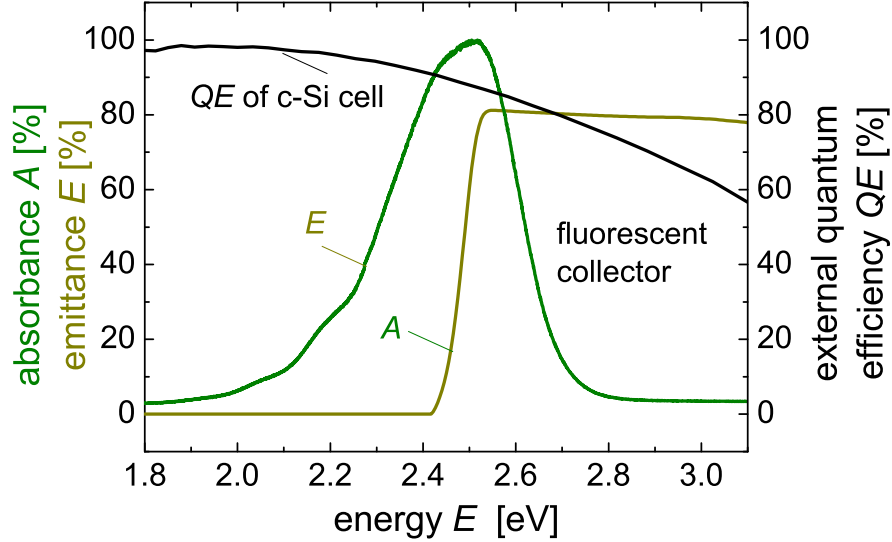


Fig. 4.19: Absorbance A of the fluorescent collector is highest for wavelengths $\lambda < 512$ nm. The emittance E occurs in the wavelength range $450 < \lambda < 650$ nm. Therefore, the dye emits photons with wavelengths which reach a higher quantum efficiency QE in the solar cell than the absorbed photons.

sides beveled with angle $\beta = 46^\circ$ and a c-Si solar cell covering the trough bottom. The trough consists of acrylic glass and an optically coupled fluorescent collector lies on top. With the 2d-trough from Fig. 4.17a and the 3d-trough, I perform two measurements: The top of the fluorescent collector either is covered with a black mask as shown in Fig. 4.18b or remains uncovered as in Fig. 4.20b. As already seen in Sect. 4.2, the application of the fluorescent collector leads to losses directly above the solar cell. As indicated in Fig. 4.18b, the collector induces the same loss mechanism directly above the trough aperture. In order to compensate these losses, the fluorescent collector has to enhance the photovoltaic active area. Figure 4.20b points out that without mask the fluorescent collector increases the photon collection area. Part of the photons hitting the plate outside the trough aperture reaches the solar cell due to spatial distribution during the emission process in the dye and due to subsequent total internal reflection. Since the whole area of the fluorescent plate collects photons, the photon collection area of the trough then increases to $10 \times 10 \text{ cm}^2$ from $2 \times 4.7 \text{ cm}^2$ (2d-trough) and $5.9 \times 5.9 \text{ cm}^2$ (3d-trough).

The measurements presented in this section were taken at July, 7th - 9th 2010 on the roof top of the *ipe* in Stuttgart, Germany (latitude / longitude: $48^\circ 46' 0'' \text{ N}$

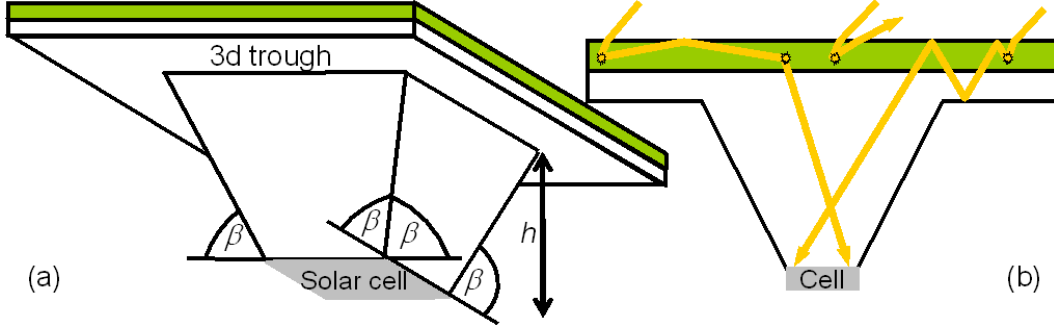


Fig. 4.20: a) 3d-trough: all four trough side surfaces are beveled, a solar cell covers the bottom and a fluorescent collector the top surface. b) Restricting the fluorescent collector area to the trough aperture as in Fig. 4.18b induces losses which are reduced by an uncovered collector leading to an enlarged photon collection area.

/ $9^{\circ} 11' 0''$ E). The troughs lie on a black underground with the acrylic top surfaces parallel to the ground. The perpendicular sides of the 2d- and the V-trough face north and south. Altogether, 5 troughs (2d- and V-trough with and without fluorescent collector and 3d-trough with collector) and a reference cell lie in the sun. The measurements with and without black mask on top of the fluorescent collector are carried out on two different days. Each solar cell is in a circuit with a resistance $R_{\text{tcells}} = 1 \Omega$. Because of this low resistance, the solar cells are considered short circuited. A KEITHLEY 27200 picks off the voltage above the resistances. A computer runs the KEITHLEY 27200 and calculates the measured voltage data into current data gained by the cells.

The solar cells in the troughs and an additional reference cell without a trough produce the short circuit currents I^{tcell} and I^{ref} , respectively. The short circuit currents $I_{\text{sosim}}^{\text{tcell}}$ and $I_{\text{sosim}}^{\text{ref}}$ of each solar cell without trough and of the reference cell, respectively, are measured with the same experimental set-up under the solar simulator of the *ipe*. The simulator provides an AM1.5G spectrum and an optical power $P_{\text{opt}} = 100 \text{ mW cm}^{-2}$. Therefore, the normalized data of the reference cell

$$I_{\text{norm}}^{\text{ref}} = \frac{I^{\text{ref}}}{I_{\text{sosim}}^{\text{ref}}} \quad (4.20)$$

denotes the fraction of one sun reached for every measuring point. Normalizing the measurement data for the trough cells

$$I_{\text{norm}}^{\text{tcell}} = \frac{I^{\text{tcell}}}{I_{\text{sosim}}^{\text{tcell}}} \quad (4.21)$$

merges the effect of applying a trough on top of the cell with the effect of a changed incident spectrum. Therefore, analyzing the influence of the trough requires the normalized data

$$I_{\text{norm}} = \frac{I_{\text{norm}}^{\text{tcell}}}{I_{\text{norm}}^{\text{ref}}} = \frac{I_{\text{tcell}}}{I_{\text{tcell}}^{\text{ref}}} \frac{I_{\text{sim}}^{\text{ref}}}{I_{\text{ref}}} \quad (4.22)$$

which decouples the influence of the changed spectrum. For $I_{\text{norm}} > 1$, the trough concentrates photons and the cell in the trough outreaches the performance of the cell without trough for the solar spectrum incident at this measuring point. Therefore, I refer to the normalized data I_{norm} as the concentration c as well.

In the following, I present the results for the measurements described above as well as simulation results gained with the Monte-Carlo model. While Sect. 3.1 elaborates the basic simulation method, I here shortly describe the assumptions made in the simulation for the experiments with the troughs. The Monte-Carlo simulation traces incoming rays with several combinations of incident angles described as the spherical coordinates (θ, ϕ) with $0^\circ < \theta < 180^\circ$ and $0^\circ < \phi < 360^\circ$. The program also regards the energy range $1 \text{ eV} < E < 4 \text{ eV}$ of incoming rays. For the troughs filled with acrylic glass, the energy of incoming photons remains unchanged, while the fluorescent collector changes the energy for photons of a certain wavelength range. Figure 4.21 presents the simulated absorbance A and emittance E spectra. I use idealized spectra for the fluorescent collector which closely display the realistic collector spectra shown in Fig. 4.19. The fluorescent collector emits all absorbed photons without non-radiative losses. The optical coupling with the underlying trough is perfect as well. The solar cell has idealized properties as written in Tab. C.1 in App. C which result in the internal quantum efficiency IQE presented in Fig. 4.21. Since $IQE = 1$ is constant throughout the wavelength range influenced by the fluorescent shift, the absorbed photons achieve the same quantum efficiency as the emitted photons. Thus, the fluorescent material shows no *spectral* effect in the simulated troughs. In contrast to the measurements, the simulation only analyzes the influence of the *spatial* distribution in the fluorescent dye.

For each combination (θ, ϕ, E) , the program calculates a photon collection probability $p_c(\theta, \phi, E)$ for each system. An analytical model developed by Ulbrich [57] identifies the composition of solar angles (θ, ϕ) and energies E for each hour of each day but neglects rays reflected by the surrounding (for example buildings). Thus, the program calculates the composition of the photon flux $\Phi(\theta, \phi, E)$ impinging onto the trough top surface. The simulated trough is parallel to the ground, analog to the measurement. Here, the troughs are considered as filters on top of the silicon

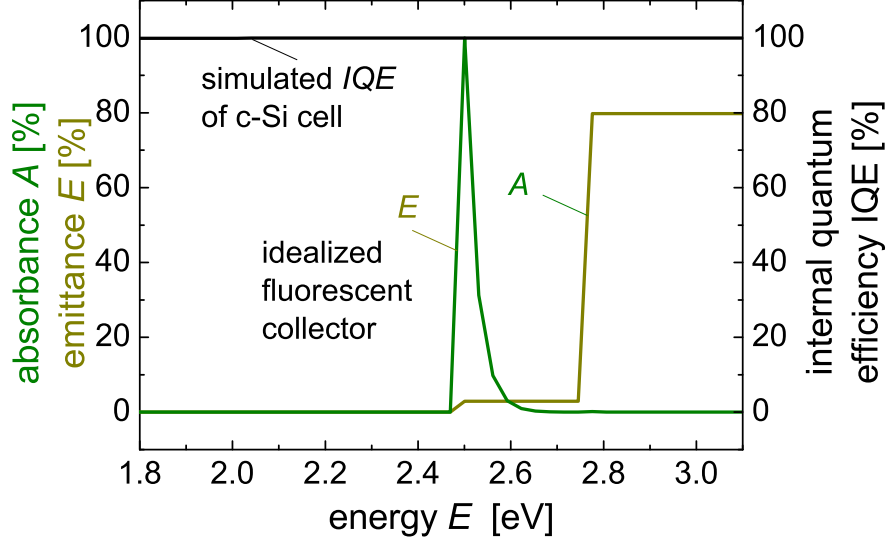


Fig. 4.21: Simulated internal quantum efficiency IQE of the idealized solar cell and idealized absorbance A and emittance E spectra of the fluorescent collector. Since $IQE = 1$ remains constant for the wavelength range influenced by the fluorescent shift, the simulation neglects the spectral influence and only regards the spatial distribution in the dye.

solar cells which transmit photons depending on their angles (θ, ϕ) and, in case of the fluorescent collector, their energy E . As described in Sect. 2, the maximum electrical output power P_{el} changes with different incoming spectra. Therefore, the solar direct and diffuse photon flux $\Phi_{inc}(\theta, \phi, E)$ impinging onto the cell is weighted by the collection probability $p_c(\theta, \phi, E)$ gained from the Monte-Carlo simulation. The modeled solar cells in the troughs and a reference cell assumed to lie uncovered in the sun produce the currents I_{tcell}^{sim} and I_{ref}^{sim} , respectively. In order to examine the trough behavior, I report the normalized data

$$I_{norm}^{sim} = \frac{I_{tcell}^{sim}}{I_{ref}^{sim}}. \quad (4.23)$$

As in the measurement, the normalized data I_{norm}^{sim} from the simulation corresponds to the concentration c^{sim} in the system.

4.3.2 Outdoor measurement results for July, 2010

The following data was measured from July, 7th 2010 till July, 9th 2010 in Stuttgart, Germany ($48^\circ 46' 0''$ N / $9^\circ 11' 0''$ E). Figure 4.22 shows that the reference cell took

similar data $I_{\text{norm}}^{\text{ref}}$ (see Eq. 4.20) for these three days and the selected times. Therefore, the measured data at the trough cells is comparable. The morning of July, 7th and the afternoon of July, 9th are disregarded due to cloudy weather. Figure 4.22 also includes the simulated reference data $I_{\text{ref}}^{\text{sim}}$ for July, 8th. This curve is normalized to its maximum. The simulated curve features a slightly different shape which appears due to the idealizations described above. Nevertheless, the agreement is sufficient enough to compare the measured and simulated systems.

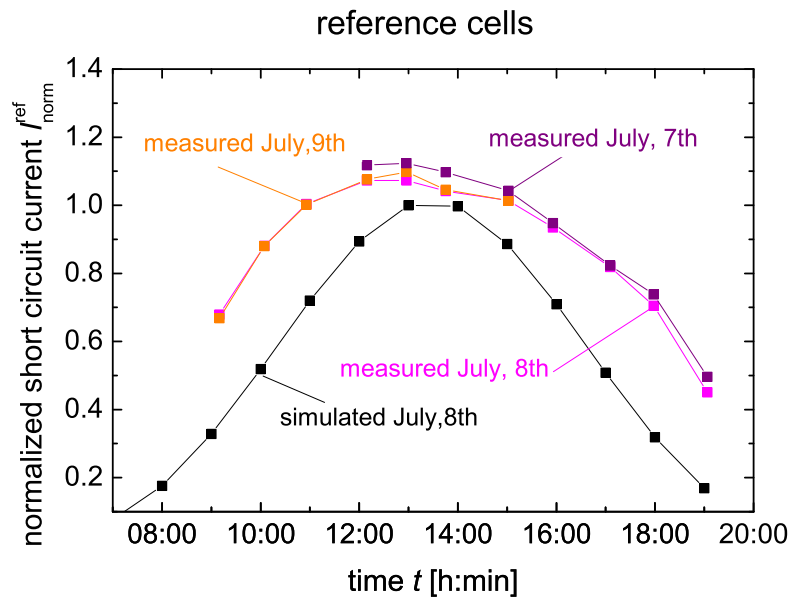


Fig. 4.22: Reference cells measured at July 7th-9th, 2010 and simulated for July, 8th. The good agreement allows a comparison of the measured and simulated trough cells.

2d-troughs

Figure 4.23a shows the measured and normalized current I_{norm} for the 2d-troughs. Over all, the trough filled with acrylic glass performs best. Around noon, the troughs reach their maximum concentration. While the fluorescent trough de-concentrates incoming photons with $c = I_{\text{norm}} < 1$ throughout the day, the acrylic glass trough concentrates incoming photons from 11.00 h to 16.00 h, reaching its maximum concentration $c = 1.6$ around noon. The decrease due to the fluorescent collector on top is highest around noon, when the solar photons come from steep angles. Figure 4.23b presents the simulation results. The simulated acrylic glass trough

performs similar to the measured system. But, since the simulated reference cell (Fig. 4.22) provides lower values for morning and evening than the measured reference cell, the normalized data of the simulated trough cell is higher at those times. In the experiment, the surrounding provides diffusely reflected photons for example from buildings. Disregarding the surrounding, the simulation achieves lower values around noon. In contrast to the acrylic glass trough, the simulated fluorescent trough reaches significantly higher values than the measured system due to the idealized loss-free properties assumed in the model for the fluorescent collector, optical coupling and solar cell.

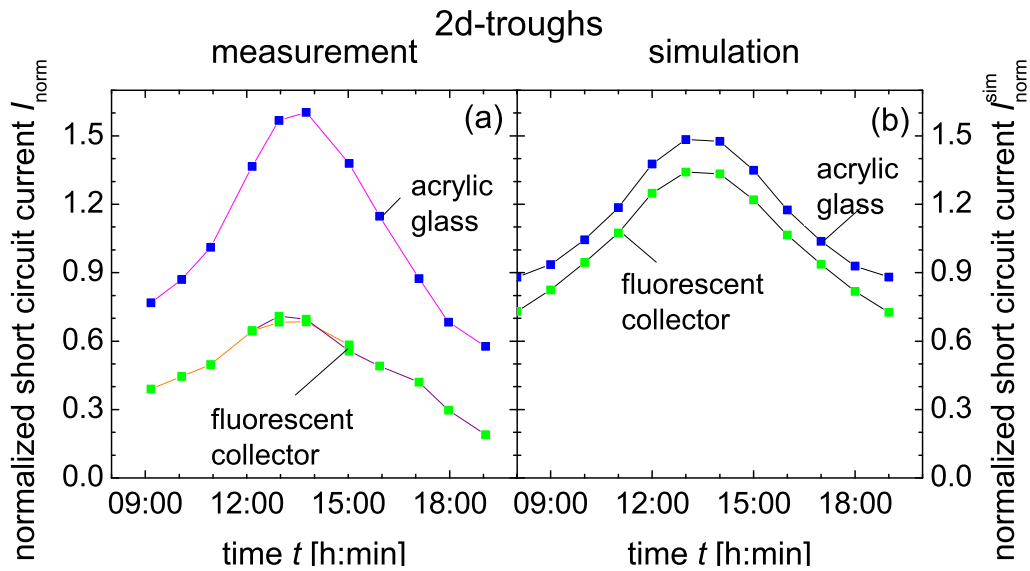


Fig. 4.23: a) Measurement of 2d-troughs. The acrylic glass trough performs best and reaches its maximum concentration $c = 1.6$ around noon. b) Simulation. Acrylic trough performs similar to the measurements, whereas the fluorescent collector performs significantly better than measured which results from the idealizations assumed in the model.

V-troughs

Figure 4.24a analyzes the V-troughs. In contrast to the 2d geometry, these troughs show a significant drop around noon. With $\beta = 22^\circ$, the angles of the beveled trough side surfaces are flat. Such, perpendicular incoming photons are transmitted through the beveled sides and not totally internal reflected onto the cells. In contrast, these flat surfaces are advantageous in the early and late hours and then lead to

higher concentrations. In Fig. 4.24b, the simulation presents a similar behavior for both troughs. Around noon, the trough with fluorescent collector on top slightly outreaches the uncovered acrylic trough. Here, the distribution in the dye leads to more favorable angles than from the incoming spectrum alone. Of course, this behavior holds for the idealized system components. However, in the measurements, the difference between acrylic glass and fluorescent collector trough around noon is less significant than in the morning and the evening.

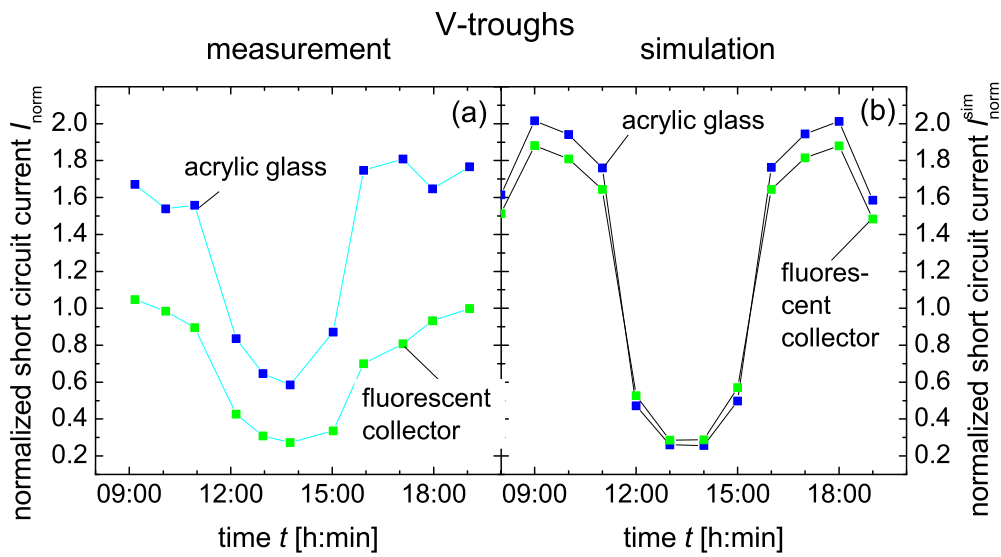


Fig. 4.24: a) Measurement of V-troughs. In contrast to the 2d-troughs, this trough geometry shows a significant drop around noon which is explainable by flat side surface angles. b) The simulation of the systems indicates that the distribution of photons in the dye is advantageous around noon where the current gain of fluorescent collector system slightly outreaches the gain in the acrylic glass trough.

Enlarged collector area

Figure 4.25a presents the results for the measurements with fluorescent collectors on top of a 2d- and a 3d-trough where either a black mask restricts the fluorescent collector to the trough aperture or the system remains uncovered. With mask, the 3d-trough (stars) performs better than the 2d-trough (circles) throughout the day. However, both systems de-concentrate with $c < 1$. Removing the mask, enlarges the collector area 2.9 times for the 3d-trough and 10.6 times for the 2d-trough.

In both trough systems, the concentration increases; around noon even to $c \geq 1$. Figure 4.25b depicts the ratio

$$c_{FC} = I_{\text{without mask}}^{\text{norm}} / I_{\text{with mask}}^{\text{norm}}. \quad (4.24)$$

According to Eq. 4.22, the measured and normalized data $I_{\text{without mask}}^{\text{norm}}$ is derived from the fluorescent collector system without mask and $I_{\text{with mask}}^{\text{norm}}$ from the system with mask. Around noon, the concentration raises 1.5 times due to removing the mask. This value holds for the 3d-trough as well as for the 2d-trough. In the morning and the evening, when more photons with oblique angles impinge on the trough, the increase of the concentration is even higher.

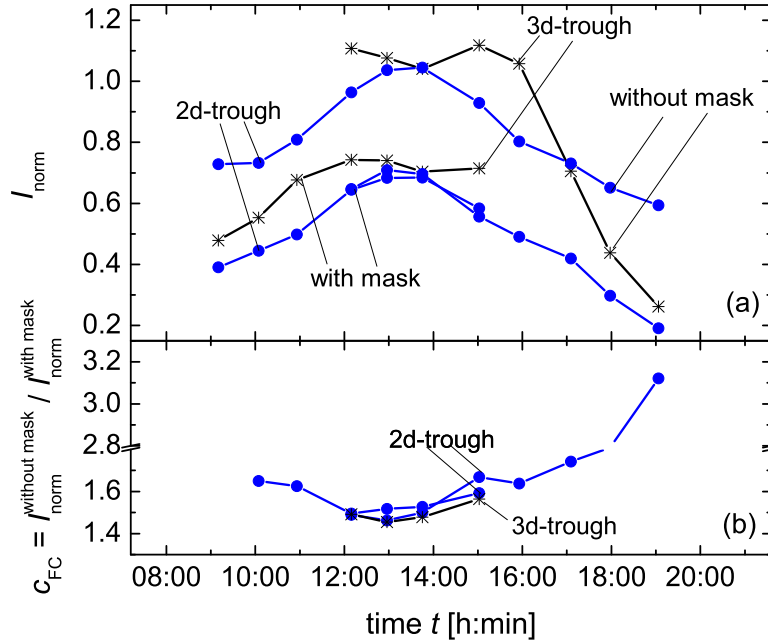


Fig. 4.25: a) Measurement data for the 2d-trough and the 3d-trough with fluorescent collector on top. Removing the mask limiting the collector to the trough aperture leads to an increased concentration. b) The ratio between the data achieved without mask to the data measured with mask. The least increase appears around noon. The accentuation of oblique angles as in the morning and the evening leads to a higher the concentration ratio.

4.3.3 Conclusion and Outlook

The simulations in Figs. 4.23b and 4.24b of the fluorescent collector with idealized properties indicate that improving the components would lead to a higher output current. Still, even idealized fluorescent material restricted to the trough aperture leads to losses due to distributing the photons during emission, as also seen in Sect. 4.2. Covering the flat V-trough with a fluorescent collector leads to slightly higher values around noon in the simulation. Here, the distribution in the dye leads photons into more favorite angles than the total internal reflection at the trough side surfaces alone. However, the trough de-concentrates with $c \approx 0.3$. Figure 4.26 shows the incident spectrum at different times simulated for July, 08th. At 8.00 h (19.00 h) 20% of the incoming photons lie in the absorption range of the fluorescent collector. Although at 13.00 h (14.00 h) only 15% of the incident photons lie in the absorption range, the system with fluorescent collector on top outreaches the uncovered system, at least theoretically. In conclusion: Bottom-mounted solar cells as in the 2d-trough most likely experience losses due to the application of a fluorescent collector on top, while side-mounted systems under certain circumstances benefit from the spatial randomization of photons in the dye. But in the case of the V-trough analyzed in this section, the beneficial effect of the fluorescent collector holds for times when the output current is already low.

In Sect. 3.2, idealized Monte-Carlo simulations show that a side-mounted system collects nearly 100% of the incoming photons, with a perfect reflector at the back side and a photonic structure on top that transmits all incoming photons and reflects almost all photons emitted by the collector. Aside from the idealized properties, this high collection probability is possible, because the incident photons are monochromatic. Figure 4.26 indicates that with an incident photon spectrum, only the absorbed part of the incoming photons is distributed. From this absorbed part only a part is totally internal guided towards the solar cell. Even a photonic structure on top reflecting all emitted photons independent from their angles is of disadvantage, because it also reflects incoming photons in the wavelength range of the emission of the dye and therefore prevents part of the incoming photons from entering the system. The measurements in this section show clearly that the dispersive concentration of fluorescent dye reaches lower output current than the geometrical concentration of trough systems. The fluorescent collector on top is disadvantageous for the bottom-mounted cell in the 2d-trough and for the side-mounted cell in the V-trough. The simulations in this section as well as the investigations of Claus Vill-

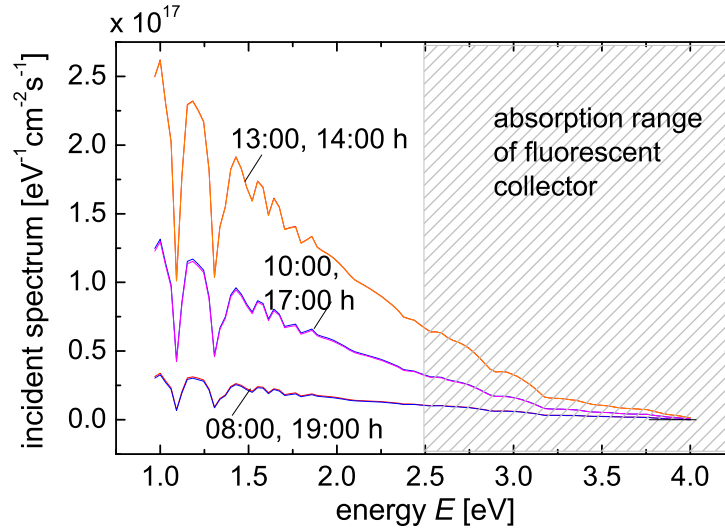


Fig. 4.26: Spectra used in the simulation. At 8.00 h (19.00 h) 20 % of incoming photons lie in the absorption range of the fluorescent collector. At 13.00 h (14.00 h) only 15 % of the incident photons have the chance to be absorbed.

ringer [58] predict certain situations where the bifacial solar cells in V-troughs gain more current with a fluorescent collector on top than without. However, these are situations where the over-all current gain is already low.

Combining dispersive and geometrical concentration

So far, the best way to use fluorescent material in a geometrically concentrating system is not at all. But, Fig. 4.25b shows that an enlarged collector area increases the concentration in the system. Around noon, when photons impinge with the steepest angle, the larger aperture increases the concentration 1.5 times in the 3d-trough as well as in the 2d-trough. Note this as a coincidence, because the trough geometries are not comparable: On one hand, the trough aperture of the 3d-trough is about 3 times larger than the 2d-trough aperture. Therefore, the losses directly above the trough aperture should be higher in the 3d-trough and the compensation due to an enhanced photon collection area lower, since the additional area is relatively smaller than in the 2d system. On the other hand, the 3d-trough guides more of the photons transmitted by the fluorescent collector onto the solar cell. The enhancement of the concentration is even higher than 1.5 times for early and late times than for noon. Here, oblique angles are more pronounced. Throughout the year, July is a time with

a large amount of steep solar angles. A higher increase than 1.5 times should be expected for the other times of the year.

In Figs. 4.23a,b and 4.24a,b, the simulation and the measurements agree sufficiently. With reservations regarding the non-ideal system components, a comparison of the simulated annual yield gives a good prediction for measurements. Figure 4.27 presents the normalized monthly power yield

$$P_{\text{norm}}^{\text{month}} = \sum_{i=1}^{28,30, \text{ or } 31} \frac{P_{\text{tcell}}^{\text{day } i}}{P_{\text{ref}}^{\text{day } i}}, \quad (4.25)$$

which is derived by simulating the output power $P_{\text{tcell}}^{\text{day } i}$ and $P_{\text{ref}}^{\text{day } i}$ for the trough cells and the reference cell, respectively, for each day i of one month. The 2d-troughs perform best: The acrylic glass trough concentrates throughout the year, while the fluorescent collector on top leads to de-concentration from September till March. The V-troughs show lower monthly power yields throughout the year than the 2d-troughs. The decrease due to the fluorescent collector on top is less significant than in the 2d troughs. Figure 4.27 also presents the values for the normalized annual yield $P_{\text{norm}}^{\text{year}}$ derived by summarizing the monthly yields for each trough and normalizing it to the sum of the monthly yields of the reference cell. Here, all troughs reach similar values with $P_{\text{norm}}^{\text{year}} = 1.2$ and 1.1 for the 2d-troughs without and with fluorescent collector on top and $P_{\text{norm}}^{\text{year}} = 1.0$ for the V-troughs.

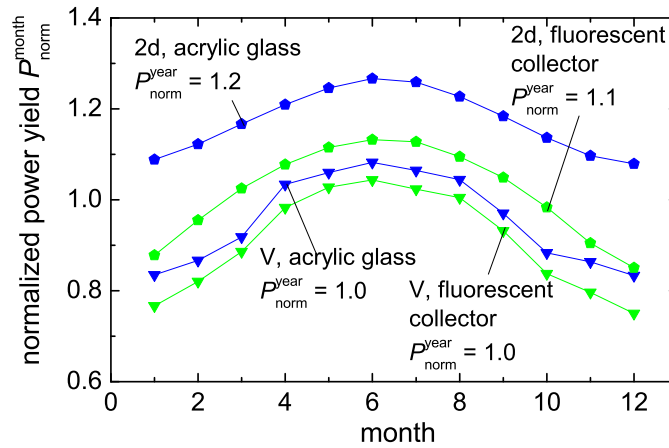


Fig. 4.27: Simulation of the normalized monthly power yield $P_{\text{norm}}^{\text{month}}$ of 2d- and V-trough geometry out of acrylic glass and with a fluorescent collector on top.

Judging from Fig. 4.25, the measurements predict an at least 1.5 times higher concentration in the systems with fluorescent collector on top by increasing the col-

lector area. A conservative estimation with 1.5 increases the normalized annual yield to $P_{\text{norm}}^{\text{year}} = 1.5$ for the V-trough and $P_{\text{norm}}^{\text{year}} = 1.65$ for the 2d-trough. Both values outreach the performance of the acrylic glass 2d-trough. Applying a fluorescent plate on top of a trough is much simpler and needs less solar cell material than building an additional trough with additional solar cell material as is necessary to increase the annual yield of the geometrically concentrating troughs.

Future research

Improving realistic geometrically concentrating systems by adding dispersive concentration due to fluorescent material works best if the distribution of the dye occurs outside the trough aperture. Such, the photon collection area is enlarged without causing losses due to distribution. In order to analyze and understand the benefits of fluorescent concentration, careful adjustment of collector size and trough distance as well as measurements over a longer period should be subject of future research.

Applying the fluorescent collector to the trough surrounding only guides the absorbed part of the incoming photons onto the cell. Of course, as shown in Fig. 4.19, the fluorescent collector emits into a wavelength range where the quantum efficiency of a c-Si solar cell is higher than in the absorption range. Such, additionally to the benefit of being spatially distributed, the fluorescent collector provides an advantageous spectral shift for the photons. However, photons transmitted by the collector are lost for the system. The next section examines fluorescent collectors on top of solar cells with surrounding white material reflecting the transmitted photons back into the collector and compares it to surrounding black material absorbing transmitted photons.

This section couples geometrical and dispersive concentration. The experimental results show that the geometrical concentration alone achieves higher concentrations than together with an additional low concentrating fluorescent collector. In order to achieve best performances, geometrical concentrating systems should be tracked [58, 59]. The next section presents a plane fluorescent collector on top of a photovoltaic module, a system which collects photons from all angles and therefore reaches highest values independent from tracking.

4.4 Output power increase of c-Si module under fluorescent collector

The previous sections described experiments with single solar cells under fluorescent collectors. For analyzing the benefits of fluorescent material in photovoltaic *modules*, the following experiment is carried out with two parallel connected mono crystalline silicon (c-Si) solar cells.

In this chapter, I examine the benefits of fluorescent collectors in a photovoltaic module in two experiments which base upon the findings of the LBIC-experiments with the amorphous silicon solar cell (Sect. 4.2). Here, the fluorescent dye molecules cause losses directly above the cell. The larger the cell, the more losses occur due to the spatial distribution of photons during the emission process. Therefore, I choose two small solar cells with area $A_{\text{cell}} = 4 \text{ cm}^2$ and then vary the distance between them in the first experiment in this section. The electrical output power P_{el} raises from $P_{\text{el}} \approx 125 \text{ mW}$ to $P_{\text{el}} \approx 173 \text{ mW}$ for underlying absorbing, black paperboard. For white, reflecting material under the cells, the power increases further to $P_{\text{el}} \approx 189 \text{ mW}$.

The LBIC-experiments also point out that the fluorescent collector guides photons impinging on the surrounding area onto the cell and such, compensates losses occurring directly above the cell. Thus, in order to overcome the efficiency reached under a clear module glass, the fluorescent area needs to be larger than the cell area. Therefore, the second experiment in this section varies the size of the fluorescent collector area surrounding the solar cell. The results determine the collector area to be at least 6 times larger than the solar module area in order to overcome the electrical power gained under clear module glass.

4.4.1 50% power increase due to fluorescent collector

Figure 4.28a depicts a side view of the experimental set-up: Acrylic glass lies on top of two solar cells. The cells are parallel connected, in order to detect a current gain due to a fluorescent collector on top. Using fluorescent collectors as cheap and easy to apply low concentrators is especially interesting in photovoltaic technologies where the cell size is limited and module area is not covered with photovoltaic active material. In Sect. 4.2, I use an amorphous silicon (a-Si) solar cell in order to examine the effect of fluorescent collectors. For this purpose, I artificially limit the cell, although a-Si usually covers large areas. In this section, I examine mono crystalline

silicon (c-Si) solar cells, since in this technology the cell area A_{cell} is limited to a certain size (state-of-the-art: $A_{\text{cell}} = 156 \times 156 \text{ cm}^2$). Also, photovoltaic inactive areas occur in the modules with c-Si cells, because usually the cells have round edges and lie apart from each other. In the experiments presented in this section, I use small solar cells cut out from an industrialized screen-printed c-Si solar cell manufactured at the *ipe*.

In order to determine the benefit of fluorescent material, the acrylic glass on top of the solar cells is either clear or doped with fluorescent dye (Acid Green, 6T66 by Perspex™ [22]). Each solar cell area is $A_{\text{cell}} = 4 \text{ cm}^2$ plus busbar (see top view of solar cell in Fig. 4.28b). On top of the busbar as well as on the solar cell back side, industrial cell connectors with width 2 mm manufactured by SOLSOL GMBH are soldered providing the electrical connection. The cells are optically coupled with Glycerin to the acrylic glass on top. Here, total internal reflection is out of action in contrast to the surrounding area. The solar cells are attached to an acrylic glass plate and under the cells lies a paperboard, either black or white.

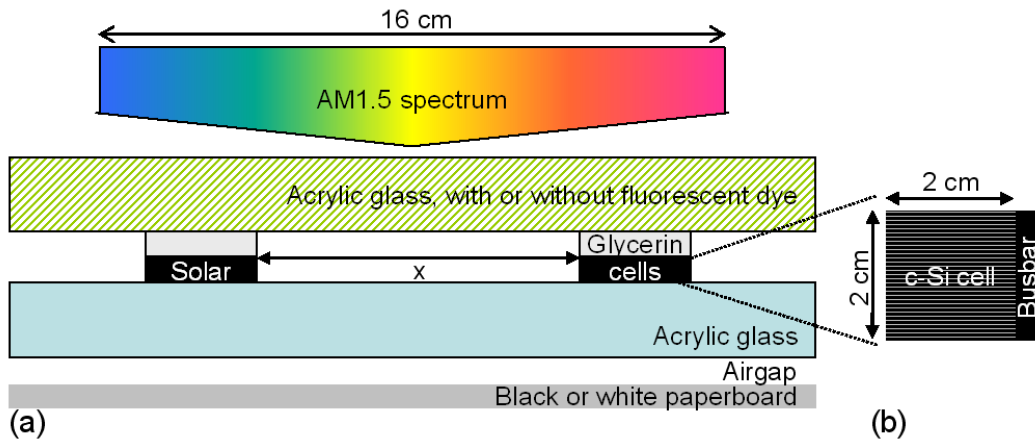


Fig. 4.28: a) Set-up for I/V -measurements. Acrylic glass lies on top of two crystalline silicon solar cells. In order to determine the benefit of fluorescence decoupled from the surrounding dielectric material, the acrylic glass is either doped with fluorescent dye or clear. b) Each solar cell area is $A_{\text{cell}} = 4 \text{ cm}^2$ plus busbar. Glycerin couples the cells optically to the acrylic glass on top. Under the solar cells lies white or black paperboard.

In [2], the inactive module area is covered with a white texture, distributing incoming solar photons Lambertian. Total internal reflection then guides part of the photons onto the cells. Here, the principle of concentration due to *spatial* dis-

tribution is similar to the process in fluorescent collectors. Figure 4.29 shows an additional advantage due to the *spectral* shift during fluorescence. The fluorescent collector used in this section shifts the wavelengths of the absorbed photons into a wavelength range where the quantum efficiency QE of the c-Si cell is higher. A higher QE leads to more electrons per incoming photons. Of course, the beneficial shift only occurs for about 80 % of the photons with wavelengths $\lambda < 486$ nm where the fluorescent dye absorbs. All other photons are transmitted through the collector. Either they directly hit the solar cell or the surrounding area. In the first experiment in this section, I examine two different covers of the surrounding area: Absorbing, black and reflecting, distributing, white paperboard. The black material absorbs all transmitted photons, while the dispersive, white material sends part of the transmitted photons back into the collector.

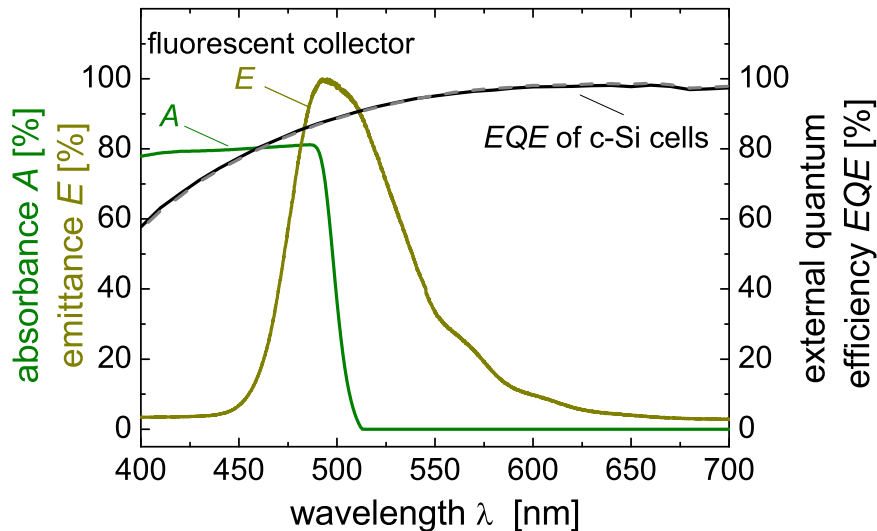


Fig. 4.29: The fluorescent collector emits photons in a wavelength range where the quantum efficiency QE of the mono crystalline silicon (c-Si) solar cells is higher than for the absorbed wavelengths. The higher QE leads to more electrons per incoming photons. Additionally to the *spatial* concentration due to distributing the photons during emission, the fluorescent collector improves the *spectral* range of incoming photons for the solar cells.

As seen in Fig. 4.28a, the set-up lies under the approximated AM1.5G spectrum of the *ipe* solar simulator in the center of an illuminated area $A_{\text{ill}} \approx 256 \text{ cm}^2$. To avoid edge effects the area of the acrylic glass exceeds A_{ill} . The impinging optical

power is $P_{\text{opt}} = 100 \text{ mW cm}^{-2}$. While the illuminated, parallel connected solar cells experience different voltages V , the output current I is measured. From this so-called I/V -curve, the open circuit voltage V_{OC} at $I = 0 \text{ mA}$ and the short circuit current I_{SC} at $V = 0$ are extracted. Then,

$$P_{\text{el}} = V_{\text{OC}} I_{\text{SC}} FF \quad (4.26)$$

with the fillfactor FF is the maximum electrical output power provided by the module.

Figure 4.30 presents the module power for various distances x for the four possible combinations of fluorescent collector or acrylic glass on top with underlying either white or black paperboard. For the application of clear acrylic glass on top of the solar cells, white paperboard ($P_{\text{el}} \approx 128 \text{ mW}$) under the set-up is of slight advantage over black paperboard ($P_{\text{el}} \approx 125 \text{ mW}$). Here, the randomized distribution leads impinging photons back into the acrylic glass, giving part of them the chance to be guided to a solar cell due to total internal reflection. The power P_{el} stays the same for small ($x = 1 \text{ cm}$) and larger ($x = 5 \text{ cm}$) distances. Therefore, the beneficial contribution of a white surrounding lies for solar cells of this size and material at 0.2%.

Replacing the clear acrylic glass with a fluorescent collector results in a power increase from $P_{\text{el}} \approx 125 \text{ mW}$ to $P_{\text{el}} \approx 170 \text{ mW}$ for all distances if the underlying paperboard is black. Since the black material absorbs impinging photons, this difference is directly ascribed to the spatial distribution and spectral shift in the fluorescent collector. Using underlying white instead of black paperboard, increases the efficiency even further. For small distances ($x = 1 \text{ cm}$ and 2 cm), the power increase is $\Delta P_{\text{el}} \approx 45 \text{ mW}$. But for $x = 5 \text{ cm}$ the power increase amounts to $\Delta P_{\text{el}} \approx 60 \text{ mW}$. Thus, increasing the distance x increases the power output under a fluorescent collector but not under a clear acrylic glass. I explain this as follows: The white paperboard spatially distributes photons and reflects part of them back into the collector. The clear acrylic glass only guides photons entering with proper angles onto a solar cell. The fluorescent collector provides the same mechanism for photons with wavelengths not absorbed by the dye. Additionally, photons in the proper wavelength range experience the benefits of spatial and spectral concentration. The smaller the distance x between the solar cells, the larger the part that one cell darkens from the photon collection area of the other cell and the higher the losses for the module.

The results of this experiment demonstrate that adding fluorescent material to

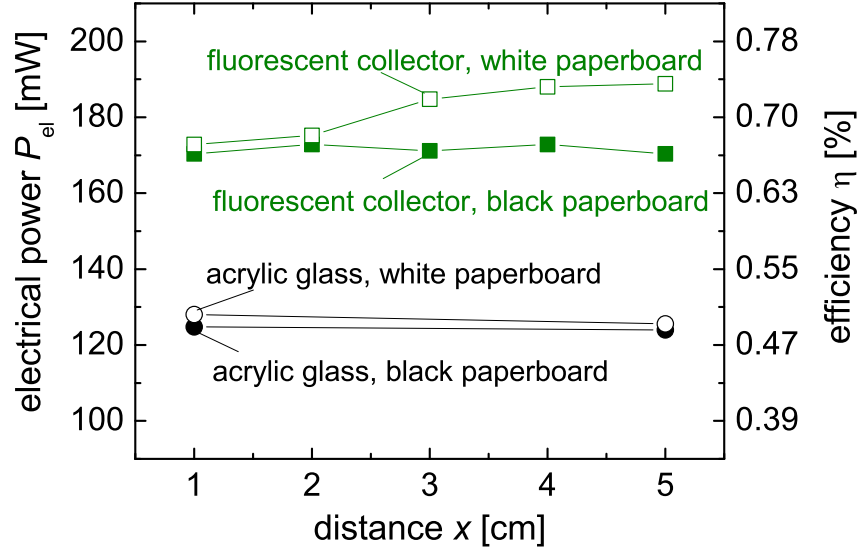


Fig. 4.30: Fluorescent collector on top of the solar cells increases the electrical output power significantly from 125 mW to 170 mW. A white paperboard underneath the solar cell adds further beneficial distribution and increases the efficiency up to 189 mW.

the module glass enhances the electrical output power. But looking at the module efficiency η which is readable at the right axis in Fig. 4.30 reveals very low values $\eta < 1\%$ compared to $\eta \approx 15\%$ as a common efficiency for c-Si modules. The derivation of η demands the specification of a reference area A_{ref} as seen in Eq. 2.1 which requests the short circuit current density $J_{SC} = I_{SC}/A_{ref}$. Assuming the solar cell area $A_{cell} = 8 \text{ cm}^2$ as A_{ref} leads to efficiencies $\eta > 15.5\%$ and 21.3% for clear and doped glass, respectively ($x = 5 \text{ cm}^2$, black paperboard). However, this assumption leads to the wrong impression that the collector guides more photons *per unit area* onto the solar cell. In other words, that the additional fluorescent collector area works as good as additional solar cell area. But actually, this experiment compares a fluorescent collector with a clear acrylic glass. Therefore, in this experiment the illuminated area $A_{ill} \approx 256 \text{ cm}^2$ is the comparative parameter and explains the low η -values. Although, A_{ill} is the same for the clear and the doped acrylic glass, the photovoltaic active area A_{opt} differs, since the whole fluorescent collector area is optically active while under the acrylic glass only the solar cell area uses photons to produce current. The following experiments clarifies the meaning of the reference area but also finds

the threshold area a fluorescent collector needs in order to overcome the efficiency gained under clear acrylic glass.

4.4.2 Threshold area

The following experiment determines the threshold area, at which this module achieves a higher electrical power P_{el} under a fluorescent collector than under a clear glass ($P_{el} \approx 125 \text{ mW}$, see Fig. 4.30). The set-up used is the similar as in Fig. 4.28 with black paperboard underneath and a fixed cell distance $x = 4 \text{ cm}$. As sketched in Fig. 4.31 on top of the fluorescent collector lies a black paperboard mask. The paperboard has openings surrounding the solar cells with the distance y between each cell edge and the opening edge which is varied. Again, the *ipe* solar simulator provides an approximated AM1.5G spectrum and $P_{opt} = 100 \text{ mW cm}^{-2}$. The results for output electrical power P_{el} and efficiency η of the module are derived from the measured I/V -curves.

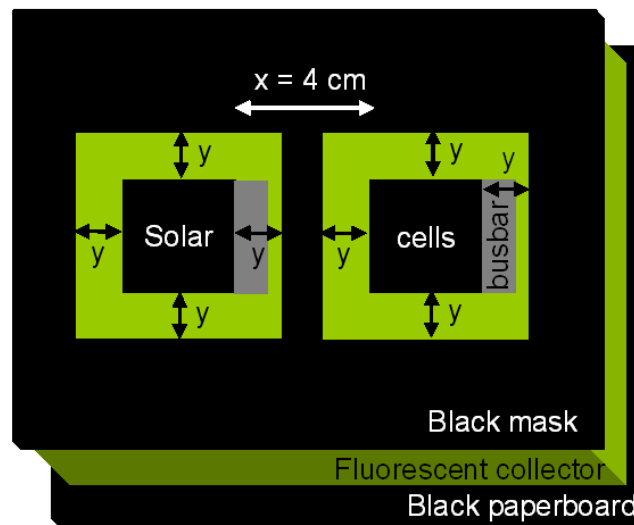


Fig. 4.31: Set-up to determine the threshold area for the fluorescent collector which has to be illuminated, in order to reach an efficiency exceeding the efficiency derived with a clear acrylic glass.

Figure 4.32a presents the electrical power results from I/V -curves measured with the set-up shown in Fig. 4.31. If $y = 0 \text{ cm}$, the fluorescent collector area is restricted to the photovoltaic active solar cell area. The module then reaches an electrical output power $P_{el} \approx 96 \text{ mW}$, while under a clear acrylic glass, the output power

is $P_{el} \approx 125$ mW. The decrease of $\Delta P_{el} \approx 30\%$ is therefore the loss induced by the fluorescent dye directly above the solar cell. Illuminating also the busbar area achieves $P_{el} \approx 105$ mW. On top of the busbar the cell connector is soldered. The connectors are usually an optical inactive part of the module, since under glass, photons impinging onto the cell connectors are reflected and leave the system. The fluorescent collector is beneficial for two reasons. First, it absorbs incoming photons and guides part of them onto the solar cell before they reach the connector. Second, photon rays reflected by the connector travel a second time through the collector experiencing a higher absorbance A .

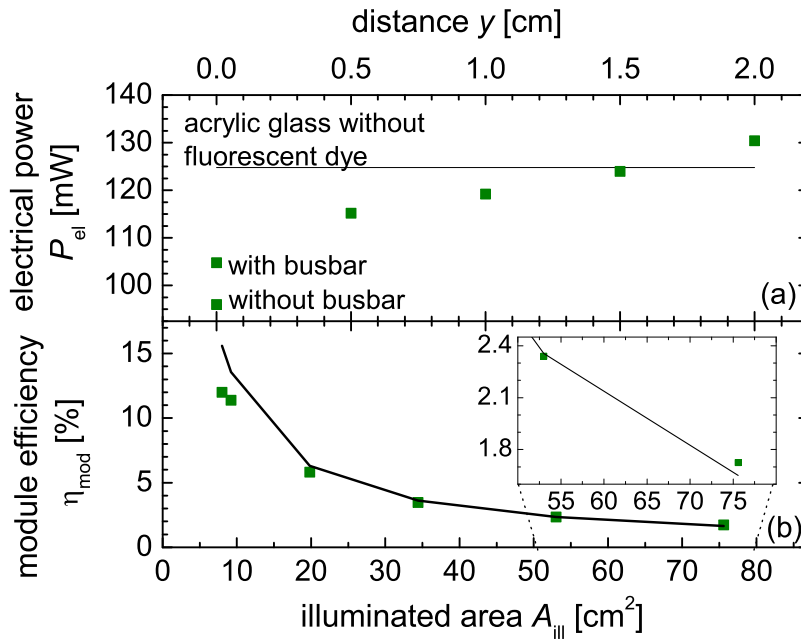


Fig. 4.32: a) Electrical output power and b) efficiency results from I/V -curves measured with the set-up shown in Fig.4.31. The mask opening $y = 1.5$ cm marks the threshold area, from which the efficiency derived by the fluorescent collector outreaches the efficiency measured under clear acrylic glass.

For $y \leq 1.5$ cm the photon collection area is too small to compensate the losses induced directly above the solar cell. But from $y = 1.5$ cm, the electrical power P_{el} derived by the fluorescent collector outreaches P_{el} measured with clear acrylic glass. For the combination of black paperboard, this fluorescent collector and this solar cell size and material, the threshold area of the fluorescent collector is $2(2 \text{ cm} + 2 \times 1.5 \text{ cm})^2 = 50 \text{ cm}^2$. Therefore, the collector area needs to be at least 6.25 times

larger than the photovoltaic active solar cell area $A_{\text{cell}} = 8 \text{ cm}^2$, in order to outreach P_{el} gained under clear acrylic glass.

Figure 4.32b depicts the results for the module efficiency η calculated with Eq. 2.1. In order to derive the short circuit current density $J_{\text{SC}} = I_{\text{SC}}/A_{\text{ill}}$, I determine the illuminated area

$$A_{\text{ill}} = 2(2y + l)^2 \quad (4.27)$$

with the solar cell edge length $l = 2 \text{ cm}$. Note, that illuminating the active solar cell area $A_{\text{ill}} = 8 \text{ cm}^2$ differs slightly from the area $A_{\text{ill}} = 8.8 \text{ cm}^2$ for additionally illuminating the busbars. The inset in Fig. 4.32b shows that for $y = 2 \text{ cm}$ ($A_{\text{ill}} = 75.6 \text{ cm}^2$) $\eta = 1.73 \%$ under the fluorescent collector outreaches $\eta = 1.65 \%$ under clear acrylic glass.

4.4.3 Conclusion and Outlook

The first experiment predicts benefits by applying fluorescent material in a module of mono crystalline silicon solar cells for the electrical output power. Requirements are a proper absorption and emission scheme of the fluorescent material, and a distributing, reflecting material works beneficially underneath the surrounding area of the solar cell. Additionally, the cell distances should be large enough to use the full potential of the spatial distribution. The second experiment shows that the loss induced by the fluorescent collector directly above the solar cell is compensated by collecting photons from the surrounding area.

Still, the module efficiencies η based on the illuminated area are very low. Thus, covering module area with fluorescent collectors instead of solar cells leads to a significant waste of incident photons. On the other hand, simply doping the clear acrylic glass with fluorescent dye leads also to losses due to distribution during the emission.

In conclusion, the application of fluorescent collectors is interesting for niche products. Greenhouses, for example, could use photovoltaic systems which cover only part of their facade. Then, doping the facade glass with fluorescent dye leads to higher electrical output power without additional shading. In general, building integrated photovoltaic systems which need a certain degree of transparency are good candidates for fluorescent material, especially if the angle towards the sun is not optimal, since the electrical power output for the absorbed photons is independent of the incident solar angle because of the spatial distribution of the photons during the emission process in the dye.

The application of fluorescent material in conventional photovoltaic modules is useful for the activation of photovoltaic inactive areas. While the cell area should be covered with clear module glass, the photovoltaic inactive areas like cell interspaces and cell connectors in a solar module should feature both, fluorescent dye and underlying distributing material. The space between the cells in a module should be optimized, such that the highest amount of photons is collected. Optical inactive areas such as cell interspaces and electrical cell connectors occur in each photovoltaic technology, crystalline or thin-film. Future experiments should analyze more fluorescent dyes, in order to find the optimum spectral shift for each solar cell technology. Then, the optimum cell interspace must be found which requires the balance between the highest possible amount of collected photons and the lowest electrical losses due to long cell connectors. Optical inactive area such as electron collecting fingers and busbars on crystalline solar cells should be activated by guiding photons onto the solar cells. In a first step, the next section analyzes an encapsulated mono crystalline silicon solar cell with white and fluorescent cell connectors.

4.5 Efficiency increase in photovoltaic modules by colored cell connectors

In the previous sections, the fluorescent collectors cover the whole solar cell area. Due to spatially distributing the photons during emission, fluorescent dyes *always* lead to losses directly above the cell. However, fluorescent material is advantageous for guiding photons from the cell surrounding area onto the solar cell. This section analyzes the benefits of fluorescence in photovoltaic modules when applied to photovoltaic inactive areas such as cell interconnecting wires.

In photovoltaic modules metallic ribbons collect the current and, at the same time, shadow the cells from the sun. For example, 4% of a mono crystalline silicon (c-Si) solar cell area is optical inactive. In this chapter, I present a simple coloring of dispersive paint on top of the connectors of an encapsulated c-Si solar cell. By guiding impinging photons onto the cell and enhancing the optical active area, the coloring induces an increased short circuit current density. White paint alone and fluorescent paint on top of white paint increase the calculated efficiency from $\eta = 16.0\%$ to $\eta = 16.2\%$. In a module, the photovoltaic inactive area is larger than 4% due to contact fingers and cell interspaces and thus, the expected efficiency increase is even higher.

Figure 4.33 reveals the basic mechanisms for photons impinging on cell connectors and the improvement due to coloring the connectors with dispersive fluorescent paint. Here, a conventional connector reflects the impinging ray #1 with its incoming angle (ray #2). Perpendicular incident light therefore leaves the system and the connector shadows the solar cell completely. White colored connectors distribute incoming rays approximately Lambertian. By hitting the glass-air surface with an angle larger than the angle of total internal reflection θ_c , ray #3 potentially hits the solar cell and induces a current. The former optical inactive area now provides photons leading to an increased efficiency. Ray #4 inside the loss cone of total internal reflection leaves the system. Fluorescent paint on top of white paint also distributes the incoming photons approximately Lambertian. Additionally, the fluorescent paint shifts the photons to a lower energy range (ray #5). These photons reach the solar cell with wavelengths where the cell's quantum efficiency is higher (see Fig. 4.34b-d). Ray #6 which is not absorbed by the fluorescent paint underlies the same conditions as rays #3 and #4. The discussed principle holds for all incoming photons regardless of their angle. Such, the loss of photons hitting the glass-air

surface is constant for all positions of the sun. In comparison to textured cell connectors [3, 60], the activation system covers a broad range of angles and shows the same efficiency gain for tracked and non-tracked systems.

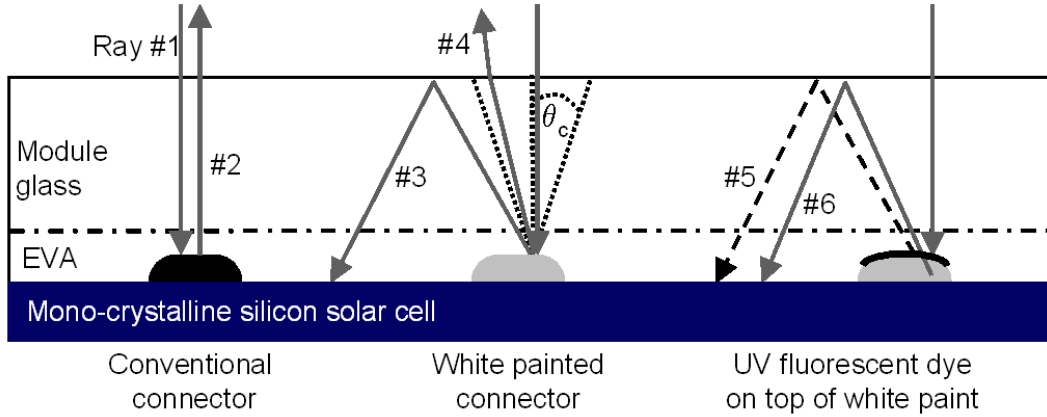


Fig. 4.33: Conventional connector reflects perpendicular incident photon ray #1 with its incoming angle (ray #2), such that the connector shadows the solar cell. White colored connectors distribute incoming rays approximately Lambertian. Ray #3 hits the surface glass-air with an angle θ larger than the angle of total internal reflection θ_c and induces current. Such, optical inactive area now provides photons increasing the efficiency. Ray #4 with angle $\theta < \theta_c$ leaves the system. Fluorescent paint on top of white paint shifts photon ray #5 to lower energies which now reach the solar cell with wavelengths where the cell’s quantum efficiency is higher. Ray #6 not absorbed by the fluorescent paint underlies the same conditions as rays #3 and #4.

4.5.1 Experimental set-up

In order to analyze the advantages of colored cell connectors, I use a mono crystalline silicon (c-Si) solar cell with three busbars provided by SOLARWATT. After soldering industrial cell connectors provided by SOLSOL GMBH of width 2 mm onto the busbars, paint is applied according to Fig. 4.34a. Part of each cell connector is painted with white color (Acrylic Spray Paint No. 7100.200 by RICO DESIGN). Half of the white area is then colored with fluorescent paint, active in different wavelength ranges. The UV fluorescent paint (Fig. 4.34b, [20, 21]) absorbs photons for wavelengths $\lambda < 400$ nm where the quantum efficiency QE of the solar cell is lower than in the emission range $400 \text{ nm} < \lambda < 500$ nm. The absorbance A of the red fluorescent paint (Fig. 4.34c, [18]) also lies in a wavelength range with lower

QE -values ($\lambda < 600$ nm), and the emitted photons reach the solar cell within the wavelength range $600 \text{ nm} < \lambda < 700$ nm with high quantum efficiency. The yellow fluorescent dye is a powder [19] mixed into the UV fluorescent paint which leads to a second emission peak additionally to the UV peak (Fig. 4.34d). The absorbance A of this mixed fluorescent paint shows high values throughout the considered wavelength range. The emission shows two peaks, the UV peak of the base material and a peak in the range $500 \text{ nm} < \lambda < 600$ nm. Unfortunately, this paint absorbs photons which reach high QE -values, whereas the emission lies in a range with lower values.

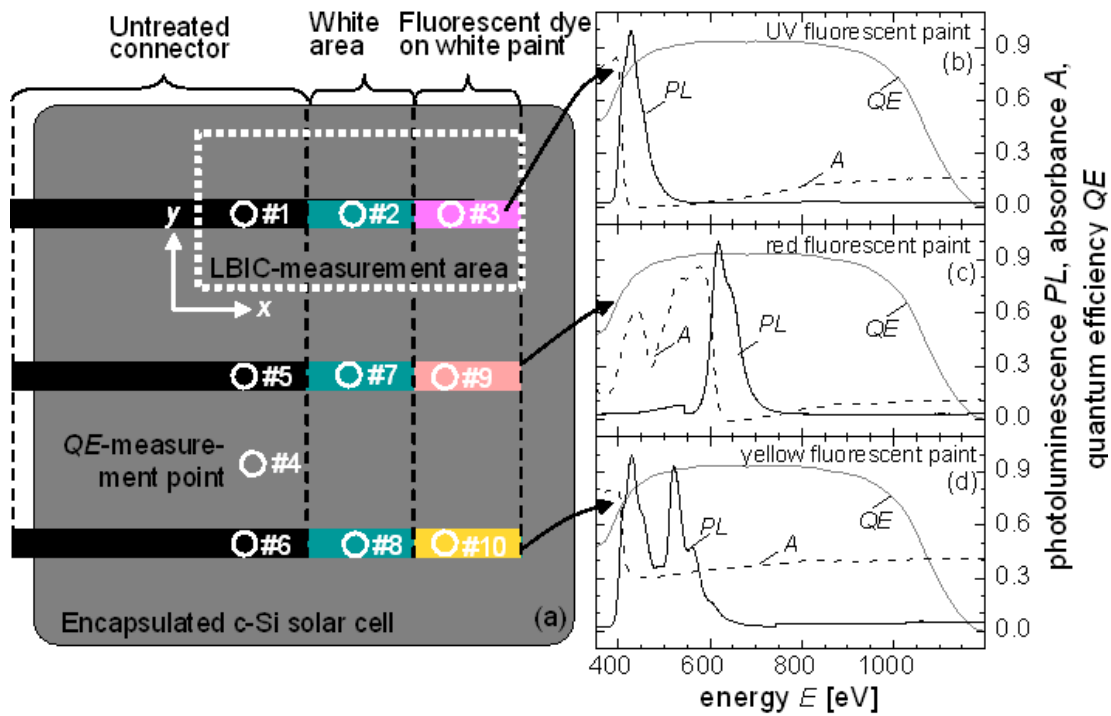


Fig. 4.34: a) A mono crystalline silicon solar cell has three soldered cell connectors partly painted white. Fluorescent paint covers half of the white area. Quantum efficiency QE measurements are performed at the numbered white circles. Light beam induced current (LBIC) measurements at the dashed white rectangle provide an areal QE -image. b) UV fluorescent dye absorbs for $\lambda < 400$ nm where the solar cell has low QE -values and emits at $400 \text{ nm} < \lambda < 500$ nm where the QE -values are higher. b) Red fluorescent dye also emits photons with high QE . c) Yellow dye powder mixed in UV fluorescent dye emits with the UV-peak and an additional peak at $500 \text{ nm} < \lambda < 600$ nm. The absorption in this mixed paint is high for all wavelengths.

The solar cell with the painted cell connectors lies under a glass with Glycerin as the optical coupling. This arrangement is close to the encapsulation of industrialized photovoltaic modules [61] where the refractive index of the optical coupling is always chosen between the refractive index of the module glass and of the photovoltaic active material.

For analyzing the efficiency increase due to coloring the cell connectors, three experiments are performed. i) The solar cell's I/V -curve is measured under the *ipe*-solar simulator which provides an AM1.5G-spectrum on an area $A_{\text{ill}} \approx 256 \text{ cm}^2$ and an optical power $P_{\text{opt}} = 100 \text{ mW/cm}^2$. ii) Quantum efficiency QE measurements at the spots #1-#10 marked with white circles in Fig. 4.34a serve as a base to calculate the short circuit current density J_{SC} provided by each area. iii) A light beam induced current (LBIC) measurement perpendicularly directs a laser beam with wavelength $\lambda = 406 \text{ nm}$ onto the solar cell within an area (dashed white rectangular in Fig. 4.34a) which includes bare, white and UV fluorescent connector area. Analog to Eq. 2.5, the quantum efficiency QE -values are calculated with the ratio of collected electrons $N_{\text{coll}}(\lambda)$ per incident photons $N_{\text{in}}(\lambda)$.

4.5.2 Results for calculated efficiency

Figure 4.35a presents a spectrally resolved external quantum efficiency QE map of an encapsulated mono-crystalline silicon solar cell derived from a LBIC measurement. While the conventional connector shows a low $QE \approx 5\%$, the QE increases on the white colored connector to $QE \approx 26\%$. The connector with white and UV fluorescent paint shows the highest $QE \approx 32\%$. The solar cell area itself provides a quantum efficiency $QE \approx 80\%$. Additionally, this map shows that the paint appears to cover the connector homogeneously. Assuming a homogeneous QE on the cell as well as on the connectors Such, I estimate the efficiency gain as explained in the following.

Figure 4.35b presents the quantum efficiencies measured at the spots #1, #2, #3 and #4 and the calculated short circuit density J_{SC} . The excitation of the white circled points occurs monochromatically within the wavelength range $350 \text{ nm} < \lambda < 1200 \text{ nm}$. Since QE -measurements provide representative values for the surrounding areas, they allow the calculation of the short circuit current density

$$J_{\text{SC}} = q\pi hc \oint \frac{1}{\lambda^2} QE(\lambda) \Phi_{\text{inc}}(\lambda) d\lambda \quad (4.28)$$

with the elementary charge q , the Planck constant h and the velocity of light c .

Equation 4.28 is analog to Eq. 2.4 with the conversion $E = hc/\lambda$. The incident spectrum $\Phi_{\text{inc}}(\lambda)$ is assumed to be an AM1.5G spectrum (see for example [15], p.193). Fig. 4.35b also includes efficiency η values for each measured spot. In the following, I explain the derivation and the meaning of η .

The cell without the connectors has an area $A_{\text{cell}} = 231 \text{ cm}^2$. The connector area for the cell under research is $A_{\text{cc}} = 9.6 \text{ cm}^2$. Thus, the connectors occupy 4% of the overall cell area $A = 240.6 \text{ cm}^2$. I estimate the over-all induced short circuit current density

$$J_{\text{SC}} = (J_{\text{SC}}^{\text{cell}} A_{\text{cell}} + J_{\text{SC}}^{\text{cc}} A_{\text{cc}}) / A \quad (4.29)$$

with the area weighted short circuit current densities $J_{\text{SC}}^{\text{cell}}$ on the cell (spots 4 in Fig. 4.35a) and $J_{\text{SC}}^{\text{cc}}$ at the connectors (spots #1-#3). For example in Fig. 4.35b, the white colored connector provides $J_{\text{SC}}^{\text{cc}} = 13.3 \text{ mA/cm}^2$ on $A_{\text{cc}} = 9.6 \text{ cm}^2$, and therefore a total current of $I_{\text{SC}}^{\text{cc}} = 127.7 \text{ mA}$. In contrast, the untreated connector induces $I_{\text{SC}}^{\text{cc}} = 16.3 \text{ mA}$. The cell area itself gains $J_{\text{SC}}^{\text{cell}} = 35.8 \text{ mA/cm}^2$ on A_{cell} which leads to the short circuit current $I_{\text{SC}}^{\text{cell}} = 8269.8 \text{ mA}$. Thus, a cell with conventional connectors achieves a total short circuit current $I_{\text{SC}} = I_{\text{SC}}^{\text{cell}} + I_{\text{SC}}^{\text{cc}} = 8286.1 \text{ mA}$ and with Eq. 4.29 a short circuit current density $J_{\text{SC}} = 34.4 \text{ mA/cm}^2$ on the entire cell area A . White paint on top of the connector then increases the short circuit current density to $J_{\text{SC}} = 34.9 \text{ mA/cm}^2$.

The fillfactor $FF = 77.1\%$ and dark saturation current density $J_0 = 6.2 \times 10^{-7} \text{ mA/cm}^2$ are determined from the illuminated J/V -curve of the cell and are assumed to be constant. With these parameters and the estimated J_{SC} inserted in Eqs. 2.2 and 2.1, I derive the photovoltaic efficiency η . In Fig. 4.35b, the conventional cell connector gains the efficiency $\eta = 16.0\%$ which white paint on top of the connectors increases to $\eta = 16.2\%$.

In Fig. 4.35b, the conventional connector provides $QE \approx 4\%$. As indicated in Fig. 4.33 for ray #1, the connector has round edges. Photons hitting the connector here have the chance to reach the solar cell via total internal reflection. Thus, a conventional connector does not completely shadow the solar cell [60]. The connector with white paint reaches significantly higher quantum efficiencies than the conventional connector. The black arrow marks $\lambda = 406 \text{ nm}$, the incident wavelength in the LBIC experiments in Fig. 4.35a. Here, the quantum efficiency increases from $QE \approx 4\%$ to $QE \approx 20\%$. The UV fluorescent paint on top of the white paint increases the quantum efficiency even further to $QE \approx 32\%$. In contrast to the white paint, the UV fluorescent paint provides photons with wavelengths below 400 nm

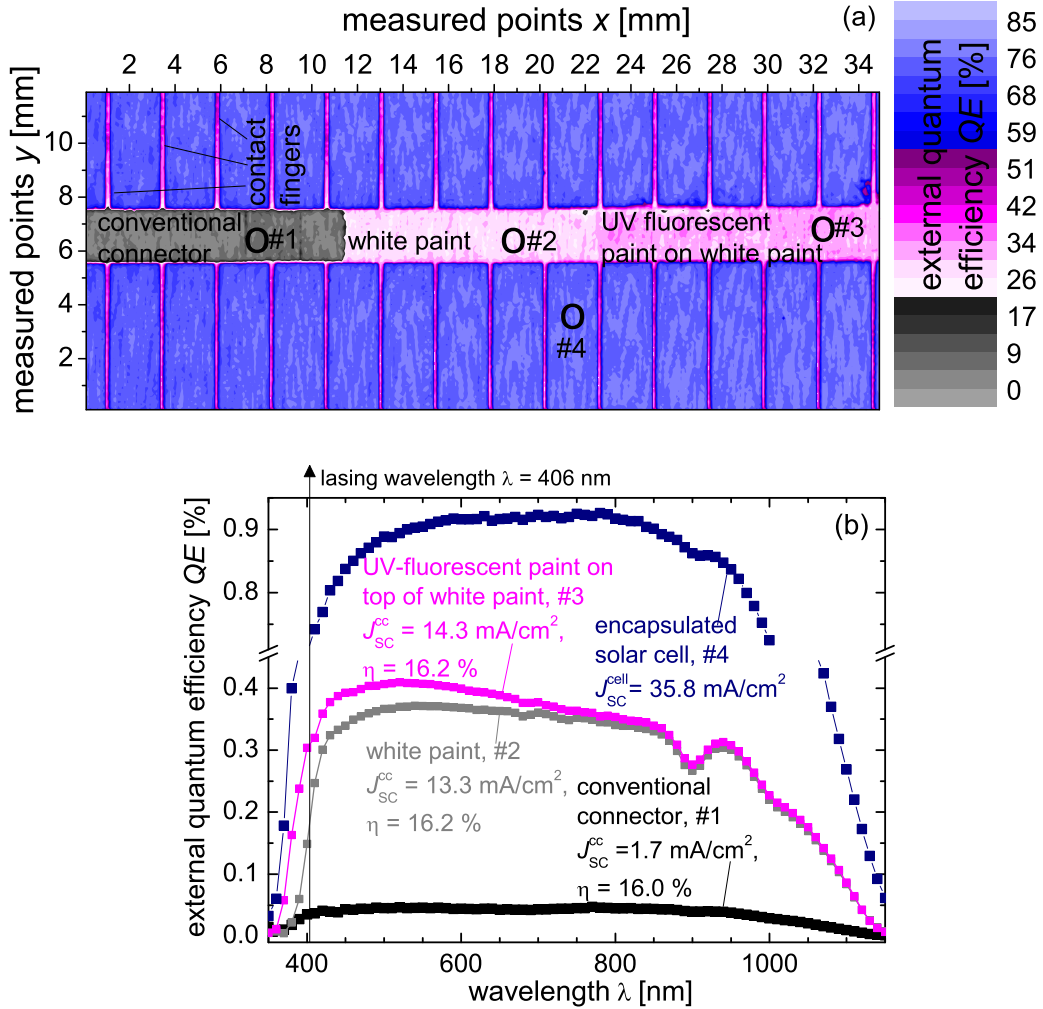


Fig. 4.35: a) External quantum efficiency QE map of an encapsulated single crystalline solar cell derived from Laser beam induced current (LBIC) measurement with lasing wavelength $\lambda = 406$ nm. While the conventional connector shows a low $QE \approx 5\%$, the QE increases on the white colored connector to $QE \approx 26\%$. The connector with white and UV fluorescent paint shows the highest $QE \approx 32\%$. In order to determine the efficiency gain of fully painted connectors, quantum efficiency measurements have been taken on the conventional connector (spot #1), white paint (spot #2), UV fluorescent paint on top of white paint (spot #3) and the solar cell itself (spot #4). b) External quantum efficiency measurement at the white circles marked in Fig. 4.35a. The solar cell itself shows values up to 92% lying in the range of industrial produced solar cells. The conventional connector provides $QE = 4\%$ quantum efficiency. The connector with white paint reaches significantly higher QE . The UV fluorescent paint on top of the white paint increases the quantum efficiency below 700 nm even further. Following Eqs. 2.1, 2.2 and 4.29, the higher quantum efficiency leads to an increased J_{SC} and therefore to a higher efficiency η .

which induce a current. The beneficial behavior results from the Stokes shift that the fluorescent material applies to the incoming photons. Above 700 nm, the fluorescent paint transmits incoming photons which then underlie the reflecting performance of the white paint as sketched in Fig. 4.33 for ray #6. The higher quantum efficiency leads to an increased short circuit current density from $J_{\text{SC}}^{\text{cc}} = 1.7 \text{ mA/cm}^2$ (conventional connector) to $J_{\text{SC}}^{\text{cc}} = 13.3 \text{ mA/cm}^2$ (white paint) and $J_{\text{SC}}^{\text{cc}} = 14.3 \text{ mA/cm}^2$ (UV fluorescent paint). Derived as explained above, conventional connectors therefore gain a solar cell efficiency $\eta = 16.0\%$. Covering the connectors with white paint alone and the additional UV fluorescent paint on top increases the calculated efficiency to $\eta = 16.2\%$. As plotted in Fig. 4.34b, the UV fluorescent dye absorbs photons with wavelength $\lambda < 400 \text{ nm}$. Thus, all other photons are transmitted by the dye and reach the underlying white painted area. The efficiency gain therefore results mainly from the dispersive behavior of the white paint.

Figure 4.36 presents QE -measurements on connectors with UV, red and yellow fluorescent dye on top of white paint. The UV fluorescent dye achieves highest short circuit current densities $J_{\text{SC}}^{\text{cc}} = 14.3 \text{ mA/cm}^2$ because according to Fig. 4.34b, the emission peak lies in a wavelength region where the solar cell shows higher QE than for the absorbed wavelengths. Although the red emission peak lies in a wavelength region with even higher QE values (Fig. 4.34c), its short circuit current density $J_{\text{SC}}^{\text{cc}} = 12.7 \text{ mA/cm}^2$ is lower. I explain this with the fact that the absorbance range already lies in a favorable QE range. Non-radiative losses in the dye then decrease the J_{SC} gain compared to the UV fluorescent dye. The yellow fluorescent paint also suffers from high absorption (Fig. 4.34d) and gains $J_{\text{SC}}^{\text{cc}} = 9.9 \text{ mA/cm}^2$. Either the yellow paint achieves even lower $J_{\text{SC}}^{\text{cc}}$ than the white paint alone or the underlying connector works worse than the other connectors, for example due to poor soldering. In order to correct the results, Fig. 4.37 and Tab. 4.1 compare the results for each area (bare, white and fluorescent) on each connector. The QE measurements which are the calculation basis are taken at the spots #1-#10 indicated with white circles in Fig. 4.34a.

Figure 4.37 also contains the QE -values for the solar cell area. Around 900 nm the QE -measurements show a slight dip which is not detected in a non-encapsulated solar cell. The dip is pronounced for the measurements on the connectors. I explain this effect with absorption in the optical coupling. The intensification in the connector measurements stems from the increased path length, since the photons travel angular through the encapsulation at least twice.

Table 4.1 clarifies that the red and the yellow fluorescent dye decrease J_{SC} com-

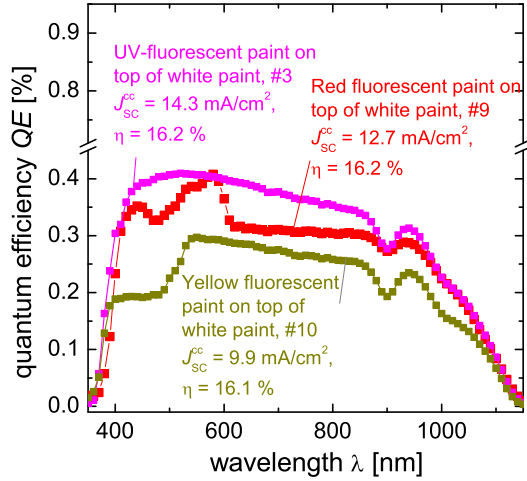


Fig. 4.36: QE -measurement on connectors with UV, red and yellow fluorescent dye on top of white paint.

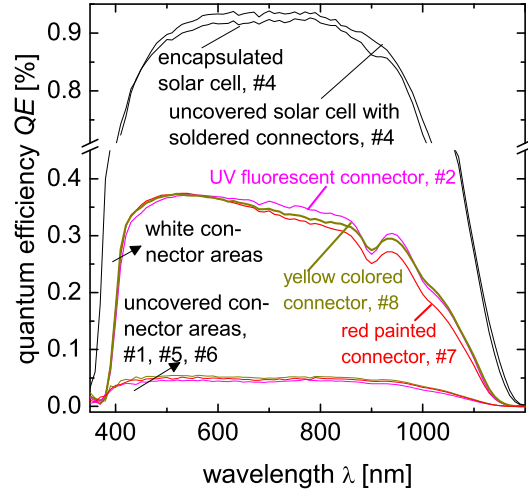


Fig. 4.37: Quantum efficiency QE results taken for different solar cell areas at marked points in Fig. 4.34a.

pared to the white paint alone. Every absorption process causes lost photons due to non-radiative recombination in the dye. The Stokes shift during the emission process in both dyes occurs into a wavelength range, for which the cell holds similar QE values as the absorption range. Therefore, the shift inhibits the compensation of losses due to non-radiative recombination. However, the differences in J_{SC}^{cc} have little influence on the efficiency η because the connector area is small compared to the cell area. Thus, the red fluorescent dye achieves $\eta = 16.2\%$ just like the UV fluorescent dye. White paint alone also gains $\eta = 16.2\%$.

4.5.3 Conclusion and Outlook

The experiments in this section prove that fluorescent material in a photovoltaic module activates photovoltaic inactive area. On single solar cell, the cell connectors shadow 4% of the cell area. By painting the connectors with a white distributive paint, the solar cell efficiency increases from $\eta = 16.0\%$ to $\eta = 16.2\%$. Adding UV fluorescent dye on top of the white paint slightly increases the quantum efficiency induced from photons which impinge on a cell connector. Conclusively, the main

Tab. 4.1: Calculated results for each connector for each area: uncovered, white and fluorescent area (see Fig. 4.34).

connector treatment, <i>QE</i> -spot in Fig. 4.34	J_{SC}^{cc} [mA/cm ²]	J_{SC} [mA/cm ²] (Eq. 4.29)	V_{OC} [mV] (Eq. 2.2)	η [%] (Eq. 2.1)
UV painted connector				
bare, #1	1.7	34.4	602.7	16.0
white paint, #2	13.3	34.9	603.1	16.2
dye on white paint, #3	14.3	34.9	603.1	16.2
red painted connector				
bare, #5	1.9	34.4	602.7	16.0
white paint, #7	12.8	34.8	603.1	16.2
dye on white paint, #9	12.7	34.8	603.1	16.2
yellow painted connector				
bare, #6	2	34.4	602.7	16.1
white paint, #8	13.3	34.9	603.1	16.2
dye on white paint, #10	9.9	34.7	603.0	16.0

benefit of colored cell connectors is their distributive behavior. However, the slightly better quantum efficiency values gained with UV fluorescent dye on top of white paint should lead to a search for suitable fluorescent dyes.

The efficiency increase presented in this section is the result of a careful calculation. Other calculations and experiments [60, 62] point in the same direction. However, experiments with a statistically relevant number of solar cells and outdoor measurements of photovoltaic modules should approve the results from this section.

Aside from the cell connectors, other photovoltaic inactive areas like contact fingers and cell interspaces occur in solar modules. As plotted in Fig. 4.35a, the contact fingers already achieve quantum efficiencies $QE \approx 35\%$. The activation of cell interspaces in a module with mono crystalline solar cells with white reflecting material has been analyzed in outdoor measurements [2]. Additionally activating the contact fingers and the cell interspaces with fluorescent material is promising subject to future research.

Appendix A

Exemplary component matching

With Figs. A.1a-d, I exemplary match the components for a photovoltaic system with the green fluorescent collector (also Fig. 2.2d). Figure A.1a includes an incident AM1.5G-spectrum and a monochromatic excitation at $E = 2.9$ eV. Figure A.1b shows the transmittance T_D spectra of two photonic band stop (PBS) filters: I compare the 11-layer PBS filter (dotted line) from Fig. 2.3 with the Rugate filter (solid line) from Fig. 2.2d. Fig. A.1c presents the photoluminescent emission PL and absorbance A spectra of the green fluorescent collector (solid and dashed line, respectively). The fluorescent collector emits photons into an energy range where the quantum efficiency QE of a crystalline silicon solar cell (Fig. A.1d) is higher than in the absorbance A range. The Rugate filter transmits photons with $E > 2.5$ eV which lie in the FC absorbance range. This filter also transmits photons with $E < 1.6$ eV and reflects all photons with $1.6 \text{ eV} < E < 2.5$ eV. Thus, it reflects most of the photons emitted by the dye. On the contrary, the 11 layer filter reflects photons with $1.8 \text{ eV} < E < 2.4$ eV. From the point of the fluorescent collector, this reflection behavior is disadvantageous, because most of the emitted photons are transmitted by the filter. If the system excitation is monochromatic for example at $E = 2.9$ eV (dashed line), the Rugate filter is of clear advantage since it transmits 70 % of the incoming photons and reflects the larger part of the emitted photons. Then again for an incident AM1.5G-spectrum, the 11-layer filter transmits most of the incoming photons, whereas the Rugate filter has a high reflectance, especially in the range where the QE of the solar cell is high. This example shows that the efficiency of a photovoltaic system with fluorescent collector and photonic structure not only depends on matching these two components to the quantum efficiency of the solar cell but also to the incident spectrum.

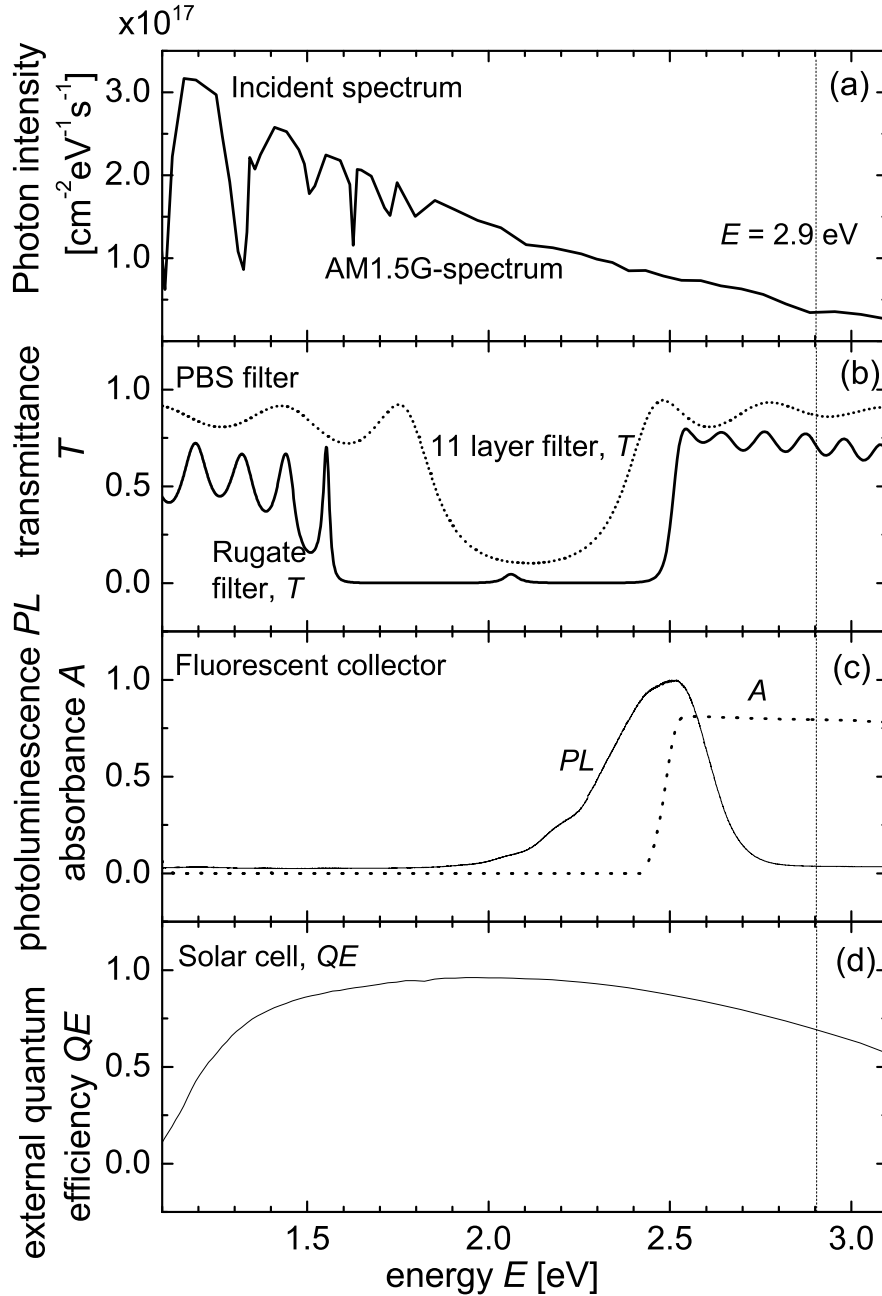


Fig. A.1: a) Incident AM1.5G spectrum or monochromatic photons with $E = 2.9$ eV. b) Transmittance T_D spectra for two photonic band stop (PBS) filters: The 11-layer filter from Fig. 2.3 (dotted line) and the Rugate filter from Fig. 2.2d. c) Absorbance A and photoluminescence PL of the fluorescent collector from Fig. 2.2d. d) Quantum efficiency QE of a crystalline silicon solar cell.

Appendix B

Evenly filled spherical surfaces

In order to describe the photon distribution of a fluorescent dye molecule, the Monte-Carlo simulations in Sect. 3 as well as the analytical description of the reabsorption (Eqs. 4.3 and 4.4) weight the emission intensity with $\sin \theta$. Figure B.1a sketches the emission behavior with evenly distributed spherical coordinates θ, ϕ . In this case, four photons with evenly distributed angle ϕ are sent to the equatorial line ($\theta = 90^\circ$) and towards the pole ($\theta \approx 180^\circ$). Thus, more photons puncture the spherical surface around the poles. As Fig. B.1b indicates, weighting the emission intensity with $\sin \theta$ pronounces the emission towards $\theta = 90^\circ$. With more photons sent to the equatorial direction, the emission sphere of the dye molecules is evenly filled.

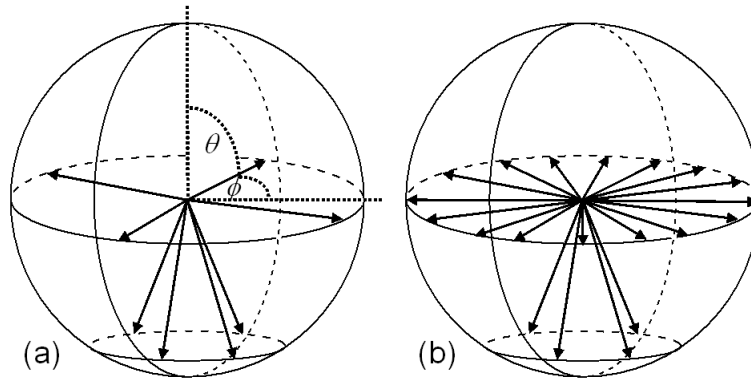


Fig. B.1: a) If the emitted photons occupy evenly distributed spherical angles θ, ϕ , less photons are sent to the equatorial line ($\theta = 90^\circ$) than to the poles ($\theta = 180^\circ$). b) Describing the emission process with $\sin \theta$ pronounces the emission to $\theta = 90^\circ$ and the emission sphere of the dye molecule is evenly filled.

Appendix C

Solar Cell Parameter

In Sect. 4.3, Fig. 4.19 shows the quantum efficiency QE exemplary for the cell in the 2d-trough with fluorescent collector on top. This is a cell cut out from an industrial mono crystalline solar cell manufactured by Q-CELLS.

Figure C.1 presents the QE values for all trough cells. Solar cells in the V- and 2d-trough with clear acrylic glass as well as in the 3d-trough with fluorescent collector on top are also cut out from the Q-CELLS-cell (dashed lines). The V-trough with fluorescent collector on top send photons onto two cells cut out from a screen-printed cell fabricated at the *ipe* (grey lines). The reference cell is also cut out from the *ipe*-cell. For all cells, the fluorescent collector emits the absorbed photons into a more beneficial wavelength range where the photons reach a higher quantum efficiency.

In order to compare the dispersive concentration of fluorescent collectors with the classical geometrical concentration, Monte-Carlo simulations provide the collection probabilities for photons of certain incident angles (ϕ, θ) and energy E . A program developed by Carolin Ulbrich calculates the particular composition of photon angles and energies for each hour of the day and uses the results of the Monte-Carlo simulations as a filter-like transmission on top of the solar cells [57]. Table C.1 presents the properties of the idealized solar cell used in this program. Choosing these parameters leads to an internal quantum efficiency as depicted in Fig. 4.21.

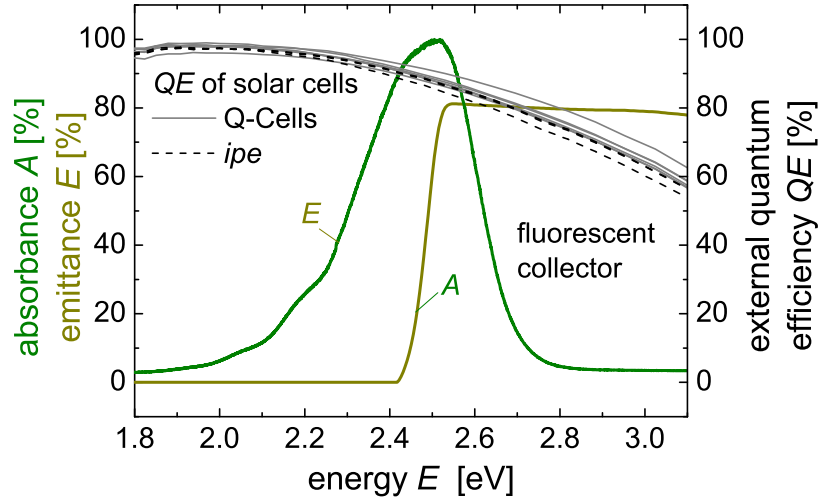


Fig. C.1: External quantum efficiency QE for trough cells cut out from industrially manufactured solar cells at *ipe* (grey lines) and Q-CELLS (dashed lines). For all cells, the collector absorbance A lies in a wavelength range with lower QE -values than the wavelength range of the photoluminescent emittance E .

Tab. C.1: Parameter of silicon solar cell simulated in trough systems which lead to the internal quantum efficiency IQE presented in Fig. 4.21.

Parameter	Value	Unit
thickness	250×10^{-4}	cm
acceptor density	1.5×10^{16}	cm^{-3}
back side recombination velocity	0	cm/s
back side reflectance	1	
diffusion constant	27	cm^2/s
lifetime	300×10^{-6}	s
intrinsic charge carrier density	1×10^{10}	cm^{-3}
refractive index	3.57	

Nomenclature

(θ, ϕ)	Spherical angles	°
(x, y, z)	Cartesian coordinates	m
2d	<u>2</u> dimensional	-
3d	<u>3</u> dimensional	-
α	Absorption coefficient	1/m
α_{reabs}	Reabsorption coefficient	1/m
β	Trough side inclination angle	°
Δ, Π	Cumulative frequency	-
η	Solar cell efficiency	%
γ	Camera opening angle	°
λ	Photon wavelength	nm
Φ_{bb}	Black body spectrum	1/m ² nm
Φ_{em}	Emitted spectrum	1/m ² nm
$\Phi_{\text{em}}^{\text{FC}}$	Emitted spectrum changed by FC	1/m ² nm
Φ_{inc}	Incident spectrum	1/m ² nm
$\Phi_{\text{inc}}^{\text{FC}}$	Incident spectrum changed by FC	1/m ² nm
a-Si	<u>a</u> morphous <u>S</u> ilicon	-
AM1.5G	<u>A</u> ir <u>M</u> ass <u>1.5</u> <u>G</u> lobal	-

c -Si	Mono crystalline Silicon	-
FC	Fluorescent Collector	-
LBIC	Light Beam Induced Current	-
LED	Light Emitting Diode	-
PBS	Photonic Band Stop	-
UV	Ultra Violet	-
V	V-shaped	-
θ_c	Critical angle for total internal reflection	$^\circ$
A	Absorbance	-
A_{cc}	Cell connector area	m^2
A_{cell}	Solar cell area	m^2
A_{coll}	Collector area	m^2
A_{ill}	Illuminated area	m^2
c	Concentration corresponding to I_{norm}	-
c	Speed of light	3×10^8 m/s
c^{sim}	Concentration corresponding to I_{norm}^{sim}	-
c_{FC}	Concentration gain due to enlarged FC	-
D	Discrete data	-
d	Collector thickness	m
d^*	Virtual collector thickness	m
d_c	Black circle diameter	m
d_{LED}	Diameter for LED illumination	m
E	Photon energy	eV

E_1	Absorption energy	eV
E_2	Emission energy	eV
E_{gap}	Band gap energy	eV
F	Camera aperture	-
f	Coverage fraction	-
FF	Fill factor	-
h	Planck constant	4.14×10^{15} eVs
I^{ref}	Reference cell current measured outdoor	A
I^{tcell}	Trough cell current measured outdoor	A
I_0	Incident photon intensity	W/m ²
I_{coll}	Over-all collected current	A
I_{norm}	Normalized current	-
$I_{\text{norm}}^{\text{ref}}$	Normalized reference cell current	-
$I_{\text{norm}}^{\text{sim}}$	Simulated normalized current	-
$I_{\text{norm}}^{\text{tcell}}$	Normalized trough cell current	-
$I_{\text{ref}}^{\text{sim}}$	Simulated normalized reference cell current	-
I_{SC}	Short circuit current	A
$I_{\text{SC}}^{\text{cc}}$	Short circuit current provided by cell connectors	A
$I_{\text{SC}}^{\text{cell}}$	Short circuit current provided by cell	A
$I_{\text{sosim}}^{\text{ref}}$	Reference cell current measured under solar simulator	A
$I_{\text{sosim}}^{\text{tcell}}$	Trough cell current measured under solar simulator	A
$I_{\text{tcell}}^{\text{sim}}$	Simulated normalized trough cell current	-
$I_{\text{with mask}}^{\text{norm}}$	Normalized current for trough under FC with mask	-

$I_{\text{without mask}}^{\text{norm}}$	Normalized current for trough under FC without mask	-
$I_{n,\text{tot}}^{\text{abs}}$	Total intensity of totally internally reflected photons after $n - 1$ absorption events	W/m ²
$I_{n,\text{tot}}^{\text{out}}$	Total intensity of photons leaving the collector after n absorption events	W/m ²
I_n^{abs}	Intensity of totally internally reflected photons after $n - 1$ absorption events	W/m ²
IQE	Internal quantum efficiency	-
J_0	Saturation current density	A/cm ²
J_{SC}	Short circuit current density	A/cm ²
$J_{\text{SC}}^{\text{cc}}$	Short circuit current density provided by cell connector area	A/m ²
$J_{\text{SC}}^{\text{cell}}$	Short circuit current density provided by cell area	A/m ²
k	Boltzmann constant	8.62×10^{-5} eV/K
l	Collector length	m
N_{coll}	Number of collected photons	-
N_{em}	Number of emitted photons	-
N_{in}	Number of incident photons	-
N_{nr}	Number of non-radiative recombined photons	-
N_{rl}	Number of non-reflected photons	-
n_r	Refractive index	-
p_c	Photon collection probability	-
p_c^{em}	Photon emission probability changed by FC	-
p_c^{inc}	Photon collection probability changed by FC	-
P_{el}	Electrical output power	W

$P_{\text{norm}}^{\text{month}}$	Normalized power yield for one month	W
$P_{\text{norm}}^{\text{year}}$	Normalized power yield for one year	W
P_{opt}	Optical power	W/cm ²
$P_{\text{ref}}^{\text{day}}$	Power yield of reference cell for one day	W
$P_{\text{tcell}}^{\text{day}}$	Power yield of trough cell for one day	W
PL	Photoluminescence	-
q	Elementary charge	1.60×10^{-19} C
QE	External quantum efficiency	-
R	Radius	m
R	Reflectance	-
R_{AG}	Reflection of acrylic glass	-
R_{tcells}	Trough cell's resistance	Ω
s	Solar cell side length	m
T	Temperature	K
t	Camera exposure time	-
T_{D}	Transmittance	-
V_{OC}	Open circuit voltage	V
$x_{\text{reabs}}, r_{\text{reabs}}$	Reabsorption radius	m

List of Tables

4.1	Calculated results for colored cell connectors	96
C.1	Parameter of simulated silicon solar cell troughs	101

List of Figures

1.1	Photovoltaic generated electricity in Germany	7
1.2	Sketch of all experiments carried out in this thesis	9
2.1	Principle of photovoltaic system with fluorescent collector, solar cell and photonic structure	11
2.2	Absorbance A and photoluminescence PL of the fluorescent materials analyzed in this thesis	14
2.3	Blue-shift in photonic structures for oblique incident photons	15
3.1	Geometries of simulated fluorescent collectors with solar cells and photonic structure	24
3.2	Properties of simulated fluorescent collectors with solar cells and pho- tonic structure	25
3.3	Simulation results for side-mounted solar cells fully covering collector edges	27
3.4	Simulated results for scaling effect for bottom-mounted solar cells . . .	30
3.5	Simulation results for comparison between bottom-mounted and side- mounted solar cells	32
3.6	Simulation results for non-radiative losses assumed in the fluorescent collector	34
3.7	Simulation results for non-perfect mirror at the collector back side . . .	36
3.8	Simulation results for non-perfect photonic structure	37
4.1	Properties of fluorescent collector in reabsorption experiment	40
4.2	Principle of reabsorption measurement	41
4.3	Grey-scale image derived from reabsorption measurement	42
4.4	Measured and simulated line-scans of reabsorption measurement	43
4.5	Idea behind analytical fit for reabsorption measurement	45

4.6	Principle sketch for the derivation of an intensity I_2^{abs} map after the first absorption	48
4.7	Sketch for the derivation of the analytical fit for reabsorption measurement	49
4.8	Calculated results of the fitting process in the reabsorption measurement	50
4.9	Set-ups for LBIC measurements of amorphous silicon solar cell under fluorescent collector and photonic structure	53
4.10	System component properties for LBIC-measurements	53
4.11	LBIC-measurement results of solar cell	54
4.12	LBIC-measurement results of solar cell under fluorescent collector . .	55
4.13	LBIC-measurement results of solar cell under fluorescent collector and photonic structure	56
4.14	Comparison of simulated and measured LBIC-line-scans	57
4.15	Principle sketch for derivation of LBIC-line-scan	59
4.16	Calculated results for LBIC-line-scan	62
4.17	2d- and V-trough geometry	65
4.18	Fluorescent collector on top of acrylic glass trough	66
4.19	Fluorescent collector and solar cell properties for geometrically concentrating troughs	67
4.20	3d-trough and enlarged collector area	68
4.21	Simulated fluorescent collector on trough	70
4.22	Measurement and simulation results for reference cells	71
4.23	Measurement and simulation results for 2d-trough	72
4.24	Measurement and simulation results for V-troughs	73
4.25	Measurement results for enlarged collector area	74
4.26	Simulated spectrum incident on troughs	76
4.27	Annual power yield of 2d- and V-trough	77
4.28	Set-up for measuring output power of crystalline solar module under fluorescent collector	80
4.29	Fluorescent collector properties lying on top of crystalline solar module	81
4.30	Measurement results for varying distance x between parallel connected crystalline solar cells	83
4.31	Set-up for measuring threshold area a fluorescent collector needs to exceed clear acrylic glass	84
4.32	Measurement results for threshold area	85
4.33	Principle sketch for colored cell connectors	89

4.34	Set-up for measuring efficiency increase due to colored cell connectors	90
4.35	Quantum efficiency results for UV fluorescent dye and white paint on cell connectors	93
4.36	Quantum efficiency results for red and yellow fluorescent dye on cell connectors	95
4.37	All quantum efficiency results for colored cell connectors	95
A.1	Exemplary component matching of fluorescent collector, solar cell, photonic structure and incident spectrum	98
B.1	Spherical angle distribution in simulation of fluorescent collectors . . .	99
C.1	Quantum efficiencies of all trough cells	101

Bibliography

- [1] D. BÖHME, *Zeitreihen zur Entwicklung der erneuerbaren Energien in Deutschland*, Bundesministerium für Umwelt, Naturschutz und Reaktorsicherheit (2010).
- [2] *Albedo SAM 88/5*, <http://www.sunage.ch/it/prodotti/albedo-sam88-5> (2011).
- [3] E. M. SACHS, J. SERDY, F. GABOR, A. M. AMD VAN MIERLO, AND T. BOOZ, in *Proc. 24th European Photovoltaic Solar Energy Conference*, edited by O. H. A. SINKE, W. C. AND P. HELM (WIP, München, 2009), p. 3222.
- [4] L. PRÖNNEKE, M. REUTER, G. C. GLÄSER, AND J. H. WERNER, in *Photovoltaic Specialists Conference (PVSC), 2010 35th IEEE* (2010), p. 002795.
- [5] A. GOETZBERGER AND V. WITTEWER, *Solar Cells* **4**, 3 (1981).
- [6] J. C. GOLDSCHMIDT, M. PETERS, A. BÖSCH, H. HELMERS, F. DIMROTH, S. W. GLUNZ, AND G. WILLEKE, *Solar energy materials and solar cells* **93**, 176 (2009).
- [7] L. H. SLOOFF, E. E. BENDE, A. R. BURGERS, T. BUDEL, M. PRAVETTONI, R. P. KENNY, E. D. DUNLOP, AND A. BÜCHTEMANN, *physica status solidi (RRL)* **2**, 257 (2008).
- [8] D. MESCHEDE, *Gerthsen Physik, 23. Auflage* (Springer-Verlag, Berlin, 2006).
- [9] B. VALEUR, *Molecular fluorescence: principles and applications* (Wiley-Vch, Weinheim, 2001).
- [10] D. C. GIANCOLI, *Physik: Lehr-und Übungsbuch* (Pearson Education, München, 2009).

- [11] *Chemikalien-Lexikon*, <http://www.omikron-online.de/cyberchem/cheminfo/glycerol.html> (2011).
- [12] *Refractive Index Database*, <http://refractiveindex.info> (2011).
- [13] G. C. GLÄSER, *Fluoreszenzkollektoren für die Photovoltaik*, Phdthesis, Universität Stuttgart (2007).
- [14] P. WÜRFEL AND W. RUPPEL, *Journal of Luminescence* **24**, 925 (1981).
- [15] P. WÜRFEL, *Physik der Solarzellen* (Spektrum, Akad. Verl., Heidelberg, Berlin, 1995).
- [16] G. P. SMESTAD, *Optoelectronics of solar cells* (SPIE, Washington, 2002).
- [17] L. PRÖNNEKE, G. C. GLAESER, Y. USLU, AND U. RAU, in *24th European Photovoltaic Solar Energy Conference, 21-25 September 2009, Hamburg, Germany*, edited by D. LINCOT, H. OSSENBRINK, AND P. HELM (WIP, München, 2009), p. 385.
- [18] *Lumogen[®] F Rot 305*, Datenblatt, BASF AG (2004).
- [19] *Lumogen[®] F Gelb 083*, Datenblatt, BASF AG (2004).
- [20] *94700 - 94739 Lumogen[®] Farbstoffe*, Datenblatt, Kremer Pigmente (2011).
- [21] *67400 - 67409 ParaloidTM B-72*, Datenblatt, Kremer Pigmente (2011).
- [22] PERSPEXTM, *Introducing PerspexTM Fluorescent*, <http://www.perspex.co.uk> (2011).
- [23] J. R. LAKOWICZ, *Principles of Fluorescence Spectroscopy* (Springer, Berlin, 1999).
- [24] M. J. CURRIE, J. K. MAPEL, T. D. HEIDEL, S. GOFFRI, AND M. A. BALDO, *Science* **321**, 226 (2008).
- [25] J. C. GOLDSCHMIDT, M. PETERS, L. PRÖNNEKE, L. STEIDL, R. ZENTEL, B. BLÄSI, A. GOMBERT, S. GLUNZ, G. WILLEKE, AND U. RAU, *physica status solidi* **205**, 2811 (2008).
- [26] E. YABLONOVITCH, *Phys. Rev. Lett.* **58**, 2059 (1987).

-
- [27] E. YABLONOVITCH, *J. Opt. Soc. Am. B* **10**, 283 (1993).
- [28] J. REBOLLAR, *Preperation and characterization of photonic layer based on Silicon-Oxynitrides*, Diplomarbeit, Universität Stuttgart (2005).
- [29] A. J. NOLTE, M. F. RUBNER, AND R. E. COHEN, *Langmuir* **20**, 3304 (2004).
- [30] B. G. BOVARD, *Applied optics* **32**, 5427 (1993).
- [31] D. POITRAS, S. LAROUCHE, AND L. MARTINU, *Applied optics* **41**, 5249 (2002).
- [32] Y. USLU, *Physikalische Gasphasenabscheidung von SiO_2 , Si_3N_4 zur Herstellung energie- und winkelselektiver Strukturen*, Diplomarbeit, Universität Stuttgart (2009).
- [33] G. M. GAJIEV, V. G. GOLUBEV, D. A. KURDYUKOV, A. V. MEDVEDEV, A. B. PEVTSOV, A. V. SEL'KIN, AND V. V. TRAVNIKOV, *Physical Review B* **72**, 205115 (2005).
- [34] A. GOETZBERGER AND W. GREUBEL, *Applied Physics A: Materials Science & Processing* **14**, 123 (1977).
- [35] L. PRÖNNEKE AND U. RAU, in *Photonics for Solar Energy Systems II*, SPIE (2008), p. 70020U.
- [36] L. PRÖNNEKE AND U. RAU, in *Light management in photovoltaic devices - theory and practice*, edited by C. BALLIF, R. ELLINGSON, M. TOPIC, AND M. ZEMAN (2008), p. KK08.
- [37] W. HENGARTNER AND R. THEODORESCU, *Einführung in die Monte-Carlo-Methode* (Carl Hanser Verlag, München, 1978).
- [38] D. W. HUBBARD, *How to measure anything: finding the value of "intangibles" in business* (Wiley, Hoboken, 2007).
- [39] J. VAN ROOSMALEN, *Semiconductors* **38**, 970 (2004).
- [40] T. TRUPKE, P. WURFEL, AND M. A. GREEN, in *Photovoltaic Energy Conversion, 2003. Proceedings of 3rd World Conference on*, IEEE (2003), p. 67.

-
- [41] A. J. CHATTEN, K. W. J. BARNHAM, B. F. BUXTON, N. J. EKINS-DAUKES, AND M. A. MALIK, *Solar Energy Materials and Solar Cells* **75**, 363 (2003).
- [42] E. YABLONOVITCH, *J. Opt. Soc. Am.* **70**, 1362 (1980).
- [43] G. SMESTAD, H. RIES, R. WINSTON, AND E. YABLONOVITCH, *Solar Energy Materials* **21**, 99 (1990).
- [44] M. BENDIG, J. HANIKA, H. DAMMERTZ, J. C. GOLDSCHMIDT, M. PETERS, AND M. WEBER, in *Interactive Ray Tracing, 2008. RT 2008. IEEE Symposium on*, IEEE (2008), p. 93.
- [45] U. RAU, F. EINSELE, AND G. C. GLAESER, *Applied Physics Letters* **87**, 171101 (2005).
- [46] G. C. GLAESER AND U. RAU, in *Society of Photo-Optical Instrumentation Engineers (SPIE) Conference Series* (2006), p. 61970L.
- [47] R. REISFELD, *Optical Materials* **32**, 850 (2010).
- [48] R. T. ROSS, *Journal of Chemical Physics* **46**, 4590 (1967).
- [49] T. MARKVART, *Journal of Applied Physics* **99**, 026101 (2006).
- [50] E. YABLONOVITCH, *Journal of the optical society of America B* **10**, 283 (1993).
- [51] M. PETERS, J. C. GOLDSCHMIDT, P. LOPER, B. BLÄSI, AND A. GOMBERT, *Journal of Applied Physics* **105**, 014909 (2009).
- [52] S. KNABE, N. SOLEIMANI, T. MARKVART, AND G. H. BAUER, *physica status solidi (RRL)* **4**, 118 (2010).
- [53] M. SCHÖFTHALER, U. RAU, AND J. H. WERNER, *Journal of Applied Physics* **76**, 4168 (1994).
- [54] D. N. CHIGRIN AND C. M. SOTOMAYOR TORRES, *Optics and Spectroscopy* **91**, 484 (2001).
- [55] H. STÖCKER, *Taschenbuch der Physik* (Verlag Harri Deutsch, Frankfurt am Main, 2000).

-
- [56] I. N. BRONSTEIN, K. A. SEMENDJAJEW, G. MUSIOL, AND H. MÜHLIG, *Taschenbuch der Mathematik* (Verlag Harri Deutsch, Frankfurt am Main, 2008).
- [57] C. ULBRICH, S. FAHR, J. ÜPPING, M. PETERS, T. KIRCHARTZ, C. ROCKSTUHL, R. WEHRSPORN, A. GOMBERT, F. LEDERER, AND U. RAU, *physica status solidi (a)* **205**, 2831 (2008).
- [58] C. VILLRINGER, *Simulation von zwei verschiedenen Solarzellentypen in Trogsystemen*, Bachelorarbeit, Universität Stuttgart (2009).
- [59] C. CARLSSON, M. B. SCHUBERT, AND J. H. WERNER, in *Proc. 20th European Photovoltaic Solar Energy Conference*, edited by W. PALZ, H. OSSENBRINK, AND P. HELM (WIP-Renewable Energies, München, Germany, 2005), p. 2418.
- [60] SCHLENK, *Light Harvesting String*, <http://www.schlenk.de> (2011).
- [61] *Planning and Installing Photovoltaic Systems: A Guide for Installers, Architects, and Engineers* (Deutsche Gesellschaft für Sonnenenergie, Earthscan, 2007).
- [62] G. C. GLÄSER, L. HAMANN, AND L. PRÖNNEKE, in *Proc. 25th European Photovoltaic Solar Energy Conference* (2010).

Danksagung

Ich danke ...

- ... Prof. Dr. Jürgen H. Werner für kritische Fragen einerseits und bedenkenlose Unterstützung andererseits. Die Jahre am *ipe* waren für mich mehr als nur Arbeit. Danke!
- ... Prof. Dr. Uwe Rau für die Wegbegleitung bei der Erkundung mathematischer Gedankenwelten.
- ... Dr. Gerda Gläser für den Pragmatismus, den meine Arbeit gebraucht hat um fertig zu werden.
- ... Dr. Gerhard Bilger für die geduldige Hilfe mit der Sputteranlage.
- ... Dr. Florian Einsele für die Herstellung meiner a-Si-Zelle.
- ... Yusuf Uslu und Claus Villringer für hilfreiche und begeisterte Mitarbeit.
- ... Dr. Thomas Kirchartz für die Einführung in die Materie und einen gelungenen Start in die Doktorarbeit.
- ... Dr. Jan C. Goldschmidt, Lorenz Steidl, Dr. Marius Peters und all den anderen vom Nano-Projekt für fruchtbare Diskussionen und interessante Denkanstöße.
- ... meinen Kollegen Kathrin Ohmer, Jakub Cichoszewski, Dr. Sebastian Eisele, Jens Kistner, Dr. Rainer Merz, Dr. Michael Reuter, Tobias Röder, Liviu Stoicescu, Dr. Marc Sämam, Lars Hamann, Thomas Wurster, Dr. Bastian Zinßer, Christian Ehling, Oliver Fechtig, Dr. Mawuli Ametowobla, Caroline Wagner, Dr. Julian Mattheis, Leo Bauer, Dr. Renate Zapf-Gottwick, Birgitt Winter, Anja Hardekopf und Dr. Barbara Bazer-Bachi für eine entspannt produktive Arbeitsatmosphäre und einige Einblicke in die Stuttgarter Freizeitgestaltung (besonders zur Wasen-Zeit).

- ... Anton Reiß für das Bauen nach untechnischen Zeichnungen.
- ... Irmgard Kerschbaum, Dr. Jürgen Köhler, Dr. Christine v. Rekowski, Heike Mohr und ganz besonders Isabel Kessler für das unkomplizierte und freundliche Verwalten meiner Person.
- ... Werner Wille für die fröhliche Aufnahme am *ipe*.
- ... Dr. Carolin Ulbrich, Gordana Kulushish und Anke Helbig für Freundschaft neben der Arbeit.
- ... Dr. Christina Lumme für Diskussionen rund um LIF und die Zukunft.
- ... meinen Eltern Annegret und Rainer für Ruheplätze und Sorglosigkeit, wann immer ich sie gebraucht habe.
- ... Dir Heiko, dass Du mein Partner bist in jeder Lebenslage.
- ... Ylva und Jele, dass Ihr so wunderbar seid!

Erklärung

Ich versichere hiermit, dass ich die Dissertation "Fluorescent Materials for Silicon Solar Cells" selbständig verfasst und keine anderen als die angegebenen Hilfsmittel verwendet habe.

Stuttgart, den 4. Juli 2011

Liv Prönneke